School of Industrial and Information Engineering

POLITECNICO
MILANO 1863

Catalytic Partial Oxidation of ethanol for small scale applications: effect of flue gas recycling

Supervisors: Prof. Gianpiero Groppi

Prof. Alessandra Beretta

Co-supervisor: Eng.Abdelrahman Mostafa

Master of Science Thesis:

Andrea Ottoboni   matr. 882835

Academic Year 2019/2020

Extended Summary

Introduction

As the demand on the green fuels for transportation sector grows and with the strict limitation on the emissions according to the international agreements and the European standards, ethanol is expected to play a great role in the market as a substitute of the gasoline. Ethanol is one of the fuels that has high energy density. It can be produced directly from biomass by fermentation which makes it a renewable fuel. The suitability of the ethanol for the transportation sector comes from the fact that it can be used with minimal modifications of the internal combustion engines available in the market right now. It can also be blended with the gasoline to add a renewable value to the fuel. The use of ethanol as a fuel is debated to improve the combustion efficiency of the engines due to the extra oxygen atom provided by it (C_2H_5OH).

For many years the on-board production of hydrogen has been studied. Having a source of hydrogen on board the vehicles will have a great added value in terms of emission abatement (by reducing the flue gases), power generation (using a fuel cell), and combustion efficiency improvement. Among the hydrogen production options studied the catalytic partial oxidation of the fuel is a process that shows high promise in terms of suitability to the transportation sector. The suitability of performing the catalytic partial oxidation relies on its autothermal nature: no external heating or special reactants are required, since during this process part of the fuel is oxidized in sub-stoichiometric conditions to provide the required heat for the endothermic reforming processes.

Objective of the study

In this thesis, the catalytic partial oxidation of ethanol is studied on an adiabatic reactor. The objective of this study is the evaluation of the effects of flue gas recycling on the performance of the process to be used for the small-scale on-board production of hydrogen for the transportation sector. The catalysts used are wash-coated on cordierite honeycomb monoliths. This arrangement ensures fast conversion of the feed to syngas with low-pressure drops.

From the definition of the scheme of this process, a sequence of exothermic and endothermic reactions take place. This behavior results in a local hot spot on the catalyst. From previous studies with different fuels it was understood that this local hot spot is one of the main reasons for the deactivation of the catalyst by sintering. Under the influence of the high temperature the active metallic particles tend to cluster leading to reduction of the active surface area thus overall reduction of the catalyst activity. To reduce this phenomenon diluted streams were used in performing all the experiments. Through this thesis the process behavior is studied by evaluating the temperature and the concentration profiles along the axis of the reactor. Both the solid and the gas phases temperatures are measured in situ in order to assess the homogenous and the heterogeneous reactions taking place. From the concentration profiles the reaction steps can be evaluated in order to improve the overall selectivity and conversion of the catalyst. Another deactivation mechanism becomes very significant when dealing with oxygenated fuels is deactivation by coke deposition. The severity of this phenomena is evaluated at the catalyst end of life by performing temperature programmed oxidation (TPO) for samples taken from the monoliths.

Procedure

The experiments performed in this thesis are performed on an adiabatic reactor. The feeding of the fuel is done by using a peristaltic pump. The liquid fuel, herein water-ethanol mixture, is then evaporated and then all the feeding streams are mixed in a static mixer. Later, this stream is fed to the reactor where the catalyst is located. The catalyst Rh/α-Al_2O_3 is wash coated on a cordierite honeycomb monolith. To ensure proper mixing an inert foam monolith is positioned before the catalytic monolith. And to ensure adiabaticity another inert monolith is positioned downstream the catalytic monolith. Besides the inert monolith, part of the catalytic monolith is left uncoated to act as a heat shield. The experiments on this thesis are

performed using both the back heat shield (BHS) and the front heat shield (FHS) arrangements, where the inert part of the catalytic monolith is positioned downstream the catalytic part (BHS) or upstream (FHS) . The temperature profiles of the reactor are collected in situ and without disruption of the process by inserting a quartz capillary tube inside the reactor with a thermocouple mounted inside it. The solid phase temperature of the reactor is measured by using a pyrometer with an optical fiber mounted inside the capillary tube. The collection of the solid and the gas phase temperatures throughout this thesis work is called "temperature test". For the collection of the concentration profiles a capillary tube with an open end is used to collect samples that can be sent to the gas chromatogram to evaluate the concentrations of the different components in the reactor. The capillary is moved along the axis of the reactor by using a linear actuator. This experiment is called "concentration test". The standard methane test, C/O = 0.9, is used to evaluate the catalyst deactivation where the catalyst deactivation has no effect on methane oxidation reaction, given its high rate, while it limits only the CH_4 steam reforming reaction rate, hence the rate of heat removal. In this way, hot spot temperature is a function of catalyst deactivation. A higher hot spot means a higher catalyst deactivation.

The catalyst prepared for this campaign is Rh/Al_2O_3 deposited on cordierite honeycomb monolith. The catalysts are prepared by impregnating the α-Al_2O_3 supports with a solution containing rhodium nitrate. α-Al_2O_3 was obtained starting form commercial product and subsequently by calcination at 1100°C. Wash-coat deposition on the monolith is performed by the dip coating technique and then the excess slurry is removed by blowing with stream of high pressure air.

Experimental results

This study addresses the analysis on the effect of CO_2 addition to water-ethanol mixture CPO. The operating conditions are selected in order to maximize the hydrogen formation and minimizing catalyst deactivation by sintering or carbon deposition according to the results of a thermodynamic analysis. C/O ratio of 0.7, dilution ratio R of 0.25 and water molar concentration in the feed of 5% were chosen for the experimental activity. Temperature and concentration profiles are collected for a CO_2 molar concentration in the feed of 0% and 9%. The results of these experiments show that, by replacing part of the diluting nitrogen with CO_2, the hot spot temperature decreases and the temperature profiles

slightly shift to lower values. Despite a cooling effect kinetics are still very rapid as observed in the large concentration gradient for most of the species occurring at the entrance of the reactor. The concentration profiles show a lower hydrogen to carbon monoxide ratio downstream the reactor. A peak concentration of CH_4 is present at the entrance of the catalyst, which may be explained with the lower temperature limiting the reforming of the produced methane. The addition of CO_2 may favour the reverse water gas shift reaction or the ethanol dry reforming reaction at the entrance of the reactor, leading to the observed consumption of CO_2 and the increased production of CO and H_2O. Further experiments with different CO_2 concentration are required for a better understanding of this behaviour. It is worth mentioning that the measured molar fraction downstream the reactor are slightly different than the values found at the end of the monolith channel, which may be explained by the cup mixing effect as the outer channel of the monolith works at lower temperature due to residual heat losses by the system.

Characterization CH_4-CPO runs after each ethanol test are performed to monitor the extent of the deactivation phenomena. The catalyst tested with water-ethanol CO_2 mix, unlike the catalyst tested in the previous campaign with water-ethanol mix only, shows less stability and this is evident from the large growth of the methane characterization test peak temperatures with respect to the catalyst's time on-stream.

Postmortem analysis is performed on this catalyst to characterize the deactivation mechanism. Temperature programmed oxidation (TPO), performed on the central section of the monolith (within 0-7mm from the entrance) and on a carbon deposit collected downstream the reactor, verified that most of the coke formed onto the surface of the monolith is in the form of either stable C-species or likely stored on the support and thus interacting less with the metal.

In order to test the effect of the FHS configuration of the catalyst on ethanol CPO, where the modelling results with other fuels have shown a better match with the measured profiles for methane and propane CPO, a new batch of catalyst was prepared. Following the standard procedure, CPO of methane was performed through temperature and concentration tests in order to set the benchmark of the monolith. Differently from expectations and the previous results, the adiabatic equilibrium temperature and concentrations were not reached at the end of the catalytic channel. A further investigation was conducted to understand the possible

causes leading to this behaviour: the catalyst was cut along its central axis and it was found that the length of the internal coated area is different from the external one. This was probably related to an uneven distribution of the coating inside the channels: a modified coating technique may be required in order to solve this problem.

Solid oxide auxiliary power unit model results

The performance of a typical solid oxide fuel cell auxiliary power unit is evaluated based on energy efficiencies providing a measure of the process performance. The main components of such units are a fuel reformer, Solid Oxide Fuel Cell (SOFC), heat exchanger, off gas burner, fuel pump, adiabatic mixers, recirculation blower, and air feeding compressor. The analysis focuses on the fuel reformer, evaluating the effect of working conditions (C/O ratio) and recycling of the SOFC exhaust on the process efficiency for ethanol as a fuel. The effects of the fuel utilization of the SOFC and current density of the cell are also investigated. All the required data for the other process components are retrieved from the literature. The results of the model highlighted the benefits of recycling in terms of carbon formation despite the reduced efficiency of the system.

Table of Contents

Abstract

Catalytic partial oxidation (CPO) of ethanol-water-CO2 mixture is studied as a representative of flue gas recycling for a small-scale distributed production of syngas. Experiments are performed on an adiabatic reactor on honeycomb monoliths coated with $Rh/\alpha-Al_2O_3$ catalyst. In order to understand the behavior of the homogenous and the heterogeneous reactions taking place in the CPO, the gas and the solid phases temperatures are measured to evaluate the temperature profiles along the catalytic monolith. Moreover, axial composition profiles are measured by analyzing samples collected in situ using a capillary tube. By comparing the temperature and composition profiles resulting from different feed conditions with the benchmark profiles obtained by using methane as a reference fuel, a solid understanding of the process and the deactivation of the catalyst is possible. Moreover, temperature programmed oxidation (TPO) test is used to identify the degradation mechanisms of the catalysts.

The effect of tail gas recycling is studied also through a computational analysis performed a on solid oxide fuel cell auxiliary power unit (SOFC-APU) modelling the effect of different working conditions.

Sommario

Durante questo lavoro di tesi, l'ossidazione parziale catalitica (CPO) di una miscela di etanolo, acqua e anidride carbonica è studiata per rappresentare l'effetto di ricircolo di gas di scarico sulla produzione distribuita di gas di sintesi su piccola scala. Le prove sperimentali sono condotte in un reattore adiabatico su monoliti a nido d'ape ricoperti da uno strato catalitico di $Rh/\alpha\text{-}Al_2O_3$. Per comprendere il comportamento delle reazioni omogenee ed eterogenee che avvengono durante la CPO, sono effettuate misure di temperatura della fase gassosa e di quella solida, delineando il profilo termico lungo il catalizzatore monolitico. Sono inoltre determinati i profili assiali di composizione delle specie presenti in fase gas, analizzando campioni estratti in situ con l'utilizzo di un capillare.

Tramite il confronto dei profili di temperatura e composizione provenienti da diverse miscele reagenti e differenti catalizzatori con i profili ottenuti utilizzando il metano come combustibile di riferimento, è possibile caratterizzare nel dettaglio il processo di CPO e di disattivazione del catalizzatore. Infine, prove di ossidazione a temperatura programmata (TPO) sono svolte allo scopo di identificare il meccanismo di degradazione dello strato catalitico.

Il ricircolo dei gas di scarico è studiato anche attraverso un'analisi computazione su una unità di potenza ausiliaria combinata ad una cella combustile a ossidi solidi, valutando l'impatto di differenti condizioni di lavoro.

Parole chiave:

Ossidazione parziale catalitica; produzione di idrogeno; etanolo; syngas; rodio; attività catalitica; profili spaziali; ossidazione a temperatura programmata; SOFC-APU

Introduction

As the demand on the green fuels for transportation sector grows and with the strict limitation on the emissions according to the international agreements and the European standards, ethanol is expected to play a great role in the market as a substitute of the gasoline as a fuel for transportation. Ethanol is a liquid fuel with high calorific value. It can be produced directly from biomass by fermentation which makes it a renewable fuel. The suitability of the ethanol for the transportation sector comes from the fact that it can be used with minimal modifications of the internal combustion engines available in the market right now. It can also be blended with the gasoline to add a renewable value to the overall process. The use of ethanol as a fuel is expected to improve the combustion efficiency of the engines due to the extra oxygen atom provided by it (C_2H_5OH).

In this report, the catalytic partial oxidation of ethanol is studied in order to define the behavior of this process and its suitability for the small-scale on-board production of hydrogen for the transportation sector. In analogy with the CO_2 effect studied through the experimental activity, the effect of flue tail gas recycling is investigated on a small SOFC auxiliary power unit. This report is divided into four chapters. The first chapter studies the state-of-the-art technology of the process and reviews the most relevant research papers published and previous experimental activities performed by the laboratory of catalysis and catalytic processes (LCCP). A review of hydrogen production from small on board applications such as the SOFC auxiliary power unit is also included

The second chapter describes the experimental apparatus used in this study. The calibration processes of the different instruments are presented beside the detailed information on the spatially resolved sampling technique and its application for the evaluation of temperature and concentration profiles. Moreover, the preparation and characterization of the catalyst is reported, as well as the main processes leading to the deactivation of the catalyst. Finally, the startup procedure of the catalytic partial oxidation is reported.

In chapter three the experimental results of this study are reported including the thermodynamic calculations for the selected feeding conditions, and the obtained temperature and concentration profiles, focusing on the effect of CO_2 addition in the feed. FHS effect are also evaluated. At the end of this chapter results of the characterization

process of the spent catalysts are discussed. The fourth chapter examines the effect of flue gas recycling in a small SOFC auxiliary power unit. The analysis was performed by changing the working condition of the system. Results and future improvement are discussed at the end of this chapter.

Chapter 1: State of the art

1.1 Importance of the synthesis gas

Synthesis gas or syngas is a mixture of carbon mono-oxide and hydrogen. It has a major role in the production of many chemicals (ammonia, aldehydes, methanol and higher alcohols). It can be used as a source of hydrogen for refinery utilization or as energy carrier. It plays an important role both in terms of industrial and environmental point of view where syngas has gained more interest with the advancement of the Fischer-Tropsch process to produce clean synthetic fuels.

Currently, there is a great interest in the exploitation of gas fields located in remote areas, where the gas transportation is not economic. One of the proposed solutions is the on-site transformation of the natural gas to liquid fuels to reduce the transportation cost. This can be performed by either conversion of the gas to methanol or through the Fischer-Tropsch process.

With the increased environmental awareness, stricter limitations on the emissions is required. This will require higher levels of fuels processing in the refinery which will increase the consumption of hydrogen for the hydro-desulfurization and hydro-treating processes. The biorefinery is another consumer of hydrogen as a great deal of the biomass to fuel conversion processes require hydrogen. With the increased penetration of the biofuels in the market to overcome the elevated carbon emissions from fossil fuels, more hydrogen will be required [1].

In the next years, the role of hydrogen as energy carrier will become very relevant, both for mobile and stationary application. In this respect, on-board hydrogen production has gained attention for conversion of hydrogen into electric energy through fuel cells, regeneration of Lean NO_x Traps during rich cycles, and assisting combustion in internal combustion engines during idle regime. Hydrogen storage and distribution is highly inconvenient compared to those of logistic fuels; furthermore, on-board storage is not competitive because of higher costs and lower energy density of gaseous fuels with respect to liquid ones. In this context, H_2 on-board production from liquid fuels is a viable solution to overcome this problem [2].

1.2 Production of synthesis gas

Hydrogen can be produced from water via electrolysis, a very energy costly process, which is viable only if large amounts of cheap electric energy are available. Photolysis is a fascinating option, but still far from practical development. Accordingly, hydrocarbons are the most viable hydrogen source. The main processes for syngas production are [3]:

- Steam Reforming (SR)

Equation 1.1

Steam reforming (SR)

$$CH_4 + H_2O \leftrightarrow CO + 3H_2 \qquad \qquad \Delta H_r^0 = +206 \; kJ/mol$$

The reforming process produces a gaseous stream composed primarily of hydrogen, CO and CO_2. Steam reforming is an endothermic reaction. The reaction is conducted in a multi-tubular reactor, which enhances heat transfer rate. Generally, nickel catalysts are adopted for large scale reformers due to their low cost and good steam reforming kinetics. However, nickel is not used for small scale reformers because it has high tendency to coke formation and due to the risks related to the nickel pyrophoric behavior [4]. For these applications, rhodium is the best option because of its high specific activity. Including rhodium in the tubular reactor can also provide a gain in terms of coke formation, which could be promoted.

Methane conversion is typically around 90-92%, with syngas composition rich in hydrogen. Main issues related to this kind of process are high costs of materials, high percentage of CO_2 in the products, and the high energy requirement.
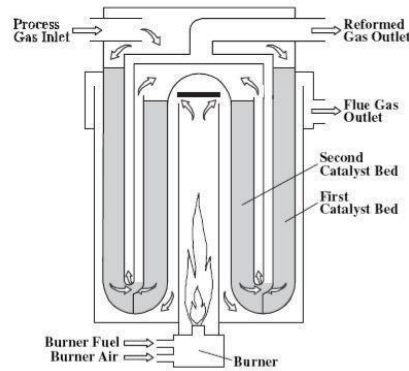
Figure 1.1 Steam reforming reactor

- Non-catalytic partial oxidation (POX)

Equation 1.2

Methane partial oxidation (POX)

$$CH_4 + \frac{1}{2}O_2 \leftrightarrow CO + 2H_2 \qquad\qquad \Delta H_r^0 = -37 \; kJ/mol$$

This reaction is slightly exothermic, so can be conducted in a non-catalytic way inside a reactor where it is necessary to reach flame temperature of 1300-1500°C to ensure complete conversion and to reduce carbon or, in the case, soot formation. This process operates at a pressure comprised between 30 and 100 bar, using pure oxygen as oxidizer, making the overall process costly and inadequate for small application.

- Auto-Thermal Reforming (ATR)

Auto-thermal reforming is a combination of partial oxidation and steam reforming reactions: it consists of a thermal zone where POX is exploited to generate the heat needed to drive the downstream steam reforming reactions. At the exit of ATR syngas is at thermodynamic equilibrium with a range of temperature between 850 and 1100°C. This system can eliminate the problem of energy expenditure of steam reforming, but it keeps the ones related to the deactivation of the catalyst and material resistance at high temperatures.

Equation 1.3

Methane total oxidation

$$CH_4 + 2O_2 \leftrightarrow CO_2 + 2H_2O \qquad\qquad \Delta H_r^0 = -802 \; kJ/mol$$

Equation 1.4

$$CH_4 + \frac{3}{2}O_2 \leftrightarrow CO + 2H_2O \qquad\qquad \Delta H_r^0 = -520 \; kJ/mol$$

Equation 1.5

Methane steam reforming

$$CH_4 + H_2O \leftrightarrow CO + 3H_2 \qquad\qquad \Delta H_r^0 = 206 \; kJ/mol$$

Equation 1.6

Water Gas Shift

$$CO + H_2O \leftrightarrow CO_2 + H_2 \qquad\qquad \Delta H_r^0 = -41 \; kJ/mol$$
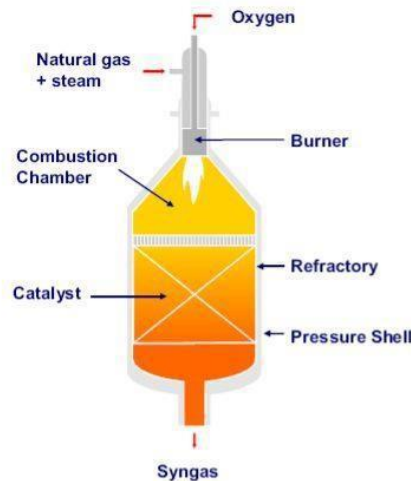
Figure 1.2 ATR reactor

Other methods to produce syngas, less important than previous ones are the following: Plasma Reforming, Aqueous Reforming, Ammonia Reforming [3].

All the previously mentioned processes are clearly inadequate for small scale applications, whose main requirement is the economic feasibility. Catalytic partial oxidation achieves this constraint. In the catalytic partial oxidation process extremely active catalysts, like rhodium, guarantees almost complete conversion of the fuel and very high selectivity to syngas up to 90% with contact time of milliseconds. In this way, it is possible to design more flexible small-scale units, with lower capital and operative costs.

1.3 Catalytic Partial Oxidation

Catalytic partial oxidation (CPO) represents an optimal solution to convert hydrocarbon fuels into synthesis gas and presents the following advantages with respect to the traditional processes [5]:

- CPO is slightly exothermic, while steam reforming is highly endothermic. This implies that the reactor is less expensive and more efficient from an energetic point of view;
- H_2/CO is 2:1. This ratio could bring advantage from operative point of view because it is the ideal ratio for bottom processes, which involve methanol synthesis or production of synthetic fuels via Fischer-Tropsch. In general, at the end of the process a separation unit for hydrogen must be implemented;
- CO_2 presence is very modest (it must be removed);
- Contact times are in the order of milliseconds, so it is possible to reduce the size of the reactor;
- Lower costs related to the use of air instead of oxygen which has the added advantage of limiting the temperature increase because of the nitrogen dilution.

On the other hand, there are some drawbacks to be taken into consideration:

- Formation of local hot spot that can damage the catalyst by means of sintering, leading to the reduction of the catalytic surface, especially for heavy hydrocarbons;
- Nitrogen present in air is hard to be separated;
- Formation of coke and soot precursors, as cracking reactions are promoted by fuel rich conditions.

1.3.1 Catalytic partial oxidation of Methane

Methane CPO has been extensively studied since 1929, when the first results were published by Liander [6]. In 1933 Padovani and Franchetti [7] obtained a methane conversion near unity in an interval of temperature between 850 and 900°C. Subsequent studies held in the late 40s [8] pointed out problems in the formation of soot on Ni catalyst.

CPO research suddenly stopped in 70s, when studies lead by Huszar [9] highlighted the importance of diffusive phenomena in the methane CPO. These studies reported that the kinetics of syngas production was limited by oxygen diffusion from bulk of the gas to catalyst pores. In 90s, Schmidt and others demonstrated that the reaction could be produced without soot formation, replacing nickel with noble metals, obtaining conversion close to thermodynamic equilibrium [10] [11].

They first try to deepen CPO mechanism, studying methane catalytic partial oxidation on noble metals for relative small time of contact (10^{-2} and 10^{-4} s) [12], observing a high selectivity of syngas but a distribution of product far from the thermodynamic equilibrium, calculated from water gas shift (WGS) and steam reforming reaction.

In following work using rhodium catalyst, these researchers reached total conversion of methane and selectivity of syngas higher than 90% [12] . Subsequent studies proposed by Tsipouriari et al. [13] demonstrated a sequence of indirect stages in the formation of syngas, theory supported by Mhadeshwar and Vlachos [14] which suggested how hydrogen could be produced via steam reforming and CO directly from POX of methane. Finally, Bizzi et al [15] proposed an indirect-consecutive mechanism for the formation of syngas.

Methane CPO: reaction mechanism

The reaction mechanism of methane CPO [16] consists of two indirect-consecutive steps:

1. Methane total oxidation with formation of CO_2 and H_2O;
2. Steam reforming of unreacted methane with formation of synthesis gas

Below, it is reported the kinetic scheme on rhodium-based catalysts for catalytic partial oxidation of methane with their relative reaction enthalpies:

Equation 1.7

Methane total oxidation

$$CH_4 + 2O_2 \leftrightarrow CO_2 + 2H_2O \qquad\qquad \Delta H_r^\circ = -802 \; kJ/mol$$

Equation 1.8

Methane steam reforming

$$CH_4 + H_2O \leftrightarrow CO + 3H_2 \qquad\qquad \Delta H_r^\circ = 206 \; kJ/mol$$

Equation 1.9

Reverse Water Gas Shift

$$CO_2 + H_2 \leftrightarrow CO + H_2O \qquad\qquad \Delta H_r^\circ = 41 \; kJ/mol$$

Equation 1.10

Hydrogen oxidation

$$H_2 + \frac{1}{2}O_2 \leftrightarrow H_2O \qquad\qquad \Delta H_r^\circ = -241.6 \; kJ/mol$$
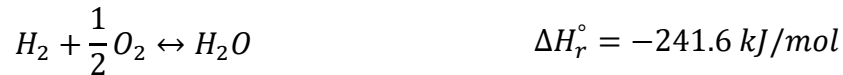
Equation 1.11

CO oxidation

$$CO + \frac{1}{2}O_2 \leftrightarrow +CO_2 \qquad\qquad \Delta H_r^\circ = -283.2 \; kJ/mol$$

Equation 1.12

Water Gas Shift

$$CO + H_2O \leftrightarrow CO_2 + H_2 \qquad\qquad \Delta H_r^\circ = -41 \; kJ/mol$$

According to the reaction scheme, methane initially reacts with oxygen forming CO_2 and H_2O as primary products (Equation 1.7); this reaction is exothermic and releases a large quantity of heat (802 kJ/mol). A fraction of this energy supports the following endothermic reaction of steam reforming (Equation 1.8). Then, once the oxygen available is totally consumed, unreacted methane reacts with H_2O producing H_2 and CO.

Reverse water gas shift (RWGS) (Equation 1.9) consumes part of the H_2 forming CO, lowering in this way the ratio H_2/CO. As the indirect-consecutive mechanism involves

equilibrium reactions, the conversion of the reactants and selectivity towards H_2 and CO are subjected to thermodynamic constraints.

1.3.2 Catalytic Partial Oxidation of iso-octane

As the transportation sector is mainly driven using liquid fuels; significant interest dedicated to the catalytic partial oxidation of these fuels. Experimental work was dedicated to the iso-octane as a representative of gasoline where gasoline has an efficient distribution network, and it is widely used in the transportation sector. The objective of these studies was to determine the suitability of the CPO process in the onboard production of hydrogen.

In his pioneering studies, O'Connor et al. investigated the CPO of many liquid hydrocarbons with different moieties. They demonstrated that the CPO of n-hexane, cyclohexane, iso-octane, iso-octane/toluene mixture, may be successfully performed over rhodium coated foams, with high yields towards synthesis gas (>90% for pure fuels) [17].

The ratio between the total amount of C atoms and the total amount of O atoms in the feed was shown to affect the product distribution, with an optimum for hydrogen production at a unitary C/O ratio. Fuel rich conditions (C/O>1) result in lower reactant conversion, higher olefins selectivity with respect to the optimal C/O = 1 for syngas production. Vice versa, while lowering the C/O ratio, fuel conversion and deep oxidation product selectivity are increased. The authors investigated the CPO of a commercial gasoline, finding catalyst deactivation during the experiment, due to sulfur and metal poisoning.

Panuccio et al. investigated the CPO of octane isomers, as pure fuels and in a 1:1 mixture, over a broad range of C/O ratios (from 0.8 to 2), with focus on the effect pore size of the ceramic foams [18]. Fuel conversion decreased with increasing C/O ratio. Gas phase reactions, responsible for the formation of olefins, were found more important in the catalyst with larger pore sizes.

A first attempt to measure spatially resolved species and temperature profiles for n-octane CPO in a packed bed reactor, has been carried out by Panuccio and Schmidt [19]. They found that Rh catalysts exhibited higher hot spot temperatures and higher oxidation rate than Pt catalysts. The rate of hydrogen formation was also higher on rhodium catalysts than on Pt. Importantly, ethylene, methane, propylene and butylene formation was also detected inside the reactor.
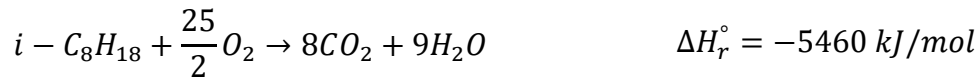
Hartmann et al. studied iso-octane CPO, finding that C/O ratio determines conversion and selectivity [20]. While oxygen was completely converted at all C/O ratios, iso-octane was entirely converted only at fuel lean conditions (C/O ratio lower than 1.1). At C/O 1.1 hydrogen yield was the highest. Methane was found to be the main by-product; minor amounts of iso-butylene, propylene and ethylene were detected. The authors employed a 2D reactor model, accounting for both homogeneous (only in the second part of the monolith) and heterogeneous reaction mechanisms. Model results revealed that catalytic reaction rates are very high at the reactor entrance, and the process is mass transfer controlled.

Iso-octane CPO: reaction mechanism

The reaction mechanism of iso-octane CPO is analogous to the one seen for methane, that is an indirect consecutive mechanism. In addition to all the reactions involved in the methane catalytic partial oxidation process the following reactions take place:

<div align="center">

Equation 1.13

iso-C8H18 total oxidation

</div>

$$i - C_8H_{18} + \frac{25}{2}O_2 \rightarrow 8CO_2 + 9H_2O \qquad \Delta H_r^{\circ} = -5460 \; kJ/mol$$

<div align="center">

Equation 1.14

iso-C8H18 steam reforming

</div>

$$i - C_8H_{18} + 8H_2O \rightarrow 8CO + 17H_2 \qquad \Delta H_r^{\circ} = 1274.9 \; kJ/mol$$
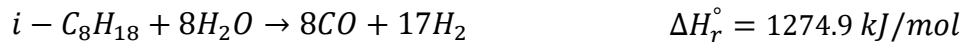
1.3.3 Catalytic Partial Oxidation of Ethanol

Ethanol is one of the fuels that has high energy density. It can be produced directly from biomass by fermentation which make it a renewable fuel. Ethanol is a promising alternative to fossil fuel, when derived from efficient source and processing, it can be considered an "environment friendly" fuel. The economic viability for the use of ethanol for catalytic partial oxidation depends on the development of proper catalysts and on the determination of appropriate reaction conditions. There are essentially two ways to produce H_2 from ethanol: one is steam reforming, the other is the catalytic partial oxidation. Ethanol oxidation presents two major hurdles, mainly related to energetic and flammability issues.

<div align="center">

Equation 1.15

Ethanol partial oxidation

</div>

$$C_2H_5OH + \frac{1}{2}O_2 \rightarrow 2CO + 3H_2 \qquad\qquad \Delta H_r^{298K} = +14 \; kJ/mol$$

As the partial oxidation reaction is slightly endothermic, a heat source is required to sustain the reaction. A viable solution is performing the process in an autothermal way where some total oxidation is needed to generate the heat required to maintain the operation at 700-1200 ^{0}C necessary for fast reaction rate:

<div align="center">

Equation 1.16

Ethanol total oxidation

</div>

$$C_2H_5OH + 3O_2 \rightarrow 2CO_2 + 3H_2O \qquad\qquad \Delta H_r^{298K} = -1277 \; kJ/mol$$

In practice, a small excess of oxygen with respect to the stoichiometry of partial oxidation can guarantee a moderately exothermic process, suitable for adiabatic operation.

From a thermodynamic point of view, the mixing between the fuel and O_2 (or air) represents an important challenge as the accidental occurrence of lean conditions will produce flames. Flammability limits of ethanol have to be considered. Figure 1.3 shows the flammability limits of ethanol-carbon dioxide-air and ethanol-air-nitrogen mixtures at 25°C and atmospheric pressure [21]. Given the ethanol and inert percentage in volume, we will find a point that eventually will fall in the region of flammable mixture.

<div align="center">
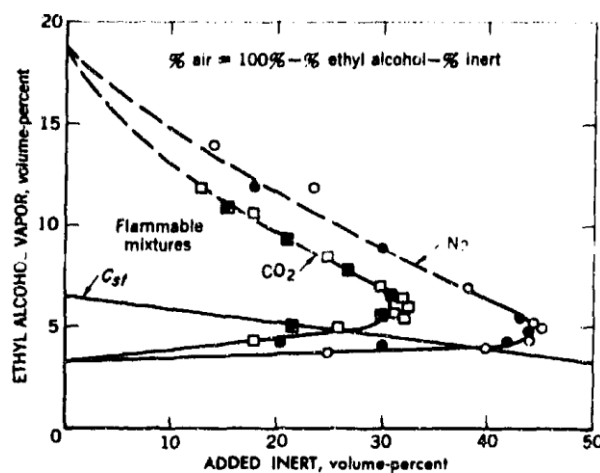
Figure 1.3 Flammability of ethanol-carbon dioxide-air and ethanol-air-nitrogen mixtures

</div>

Starting from the early 2000s, catalytic partial oxidation and autothermal reforming of ethanol have been active area of research. Mattos and Noronha [22] proposed a reaction mechanism to explain the CPO of ethanol on Pt/CeO_2 catalyst. According to this mechanism, adsorption of ethanol on the support gives rise of ethoxy species. In the absence of oxygen in the feed, a fraction of the ethoxy species can be dehydrogenated, which readily reacts with oxygen from the support, producing acetate species and Ce^{3+}. With increased temperature, another fraction of the ethoxy species migrates to the metal particle and is decomposed, forming CH_4, H_2 and CO. Furthermore, the acetate species previously formed can be decomposed to CH_4 and CO and/or oxidized to CO_2 via carbonate species. Under an oxygen rich atmosphere, the intermediate dehydrogenated species formed may desorb to acetaldehyde.

Their results indicated that an increase in the residence time or reaction temperature enhances the ethanol conversion and H_2 yield. Regarding selectivity for hydrocarbons and oxygenated products, the production of methane increased and the selectivity for acetaldehyde decreased, as the residence time or reaction temperature was increased. At low conversions, the ethanol dehydrogenation dominates, forming acetaldehyde, whereas at high conversions the decomposition of ethanol is favored, producing CH_4, H_2, and CO.

In the literature there are also studies that describe the thermodynamics and the evolution of ethanol CPO reaction: Marinov [23] characterized the reactions in homogeneous phase for oxidation at high temperature, while Koehle and Mhadeshwar [24] took into account the non-homogeneous reactions on the surface of the catalyst.

Other studies focused on different suitable catalyst for ethanol partial oxidation: from the point of view of the metal effect, Fatsikostas et al. [25] carried out their reactions by preheating ethanol to ≈500°C over lanthanides, Ru and Ni. They accomplished their tests at residence times ≈10 times longer than needed with millisecond contact time reactor. Less expensive catalyst such as Ni and Co were also studied in the same study for commercial applications.

Regarding the effect of the support, Cavallaro et al. [26] carried out their experiments by preheating ethanol to ≈650 °C over Rh/Al_2O_3 powder. Metal sintering was an issue in these experiments, which were executed in a furnace and focused on diluted ethanol solutions. Moreover, the effects of oxide metal support has been studied by Chen et al. [27] showing

that ZrO_2, CeO_2, Al_2O_3 and La_2O_3 have different effectiveness on product selectivity and ethanol, at constant feed flow rate.

More recently, Toth et al. [28] worked on the effect of the oxide support on the stability of transiently formed intermediates like ethoxide, which can be decomposed to CO_2, CO and CH_4 and dehydrogenated forming acetaldehyde in the CPO of ethanol on Rh catalyst.

By moving to operating conditions closer to those considered in this thesis, Salge et al. [29] demonstrated the feasibility of the partial oxidation of ethanol in adiabatic reactor. Ethanol and ethanol-water mixtures were converted directly into H_2 with higher than 80% selectivity and around 95% conversion of ethanol, with a residence time on rhodium-ceria catalyst of lower than 10 milliseconds. Rapid vaporization and mixing, performed at sufficiently low temperatures and sufficiently short times, allowed to minimize homogeneous reactions producing carbon, acetaldehyde, ethylene and total combustion products.

They also extended their experiments to examine the effects of catalyst and flow rate on the autothermal reforming of ethanol at catalyst contact times less than 10 ms. Noble metals (Rh, Pt and Pd), noble metal alloys (Rh-Ru) and the addition of ceria (Rh-Ce) were inspected. Rh-Ce catalysts gave the highest selectivity to syngas and were the most stable; less H_2 and minor products were produced over Rh, Rh-Ru, Pt and Pd catalysts. Under the conditions used in these experiments, surface reactions dominated: the results were interpreted based on the prevailing mechanism reported in the literature, according to which ethanol activation proceeds via adsorption as an ethoxy species and then decomposed to carbon, oxygen, and hydrogen species. These then reacted rapidly on the surface to form H_2 and CO; no reaction pathways on the surface to form greater than C_1 products were found to exist. The authors proposed that, if homogeneous reactions had dominated, then less syngas and much more CH_4 and C_2H_4 would have been observed.

1.3.4 Studies conducted at Politecnico di Milano

Regarding works conducted at Politecnico di Milano, Carrera et al. [30] studied the kinetics of the CPO of methane, propane, iso-octane and n-octane using an isothermal annular microreactor, at high space velocity and high dilution of the reacting feed. They found that the overall process over Rh/α-Al_2O_3 catalysts can be well explained by an indirect consecutive reaction scheme, consisting of the hydrocarbon deep oxidation to CO_2 and H_2O and the hydrocarbon steam reforming to CO and H_2; H_2 and CO post combustions, Water

Gas Shift (WGS), Reverse Water Gas Shift (RWGS) and CO methanation can then affect the syngas composition. Under operating conditions close to the real application (adiabatic reactor, absence of feed dilution, washcoated structured catalysts, millisecond contact times) the combustion-reforming scheme results in the onset of a hot spot of temperature at the very entrance of the reactor, which can cause an autocatalytic deactivation process. High temperatures can in fact cause catalyst sintering, with loss of activity.

The development of axially resolved sampling techniques has largely contributed to finely characterize the evolution of temperature and composition in short contact time CPO reactors [31]. In our laboratory these techniques have been applied to study the CPO of light hydrocarbons (methane and propane) over Rh and validate a 1D model of the adiabatic reactor implementing the reaction schemes derived from kinetic investigations.

Livio et al. [32] studied the CPO of ethanol over a $Rh/\alpha-Al_2O_3$ coated monoliths, using a spatially resolved sampling technique to collect axial concentration profiles, as well as surface and gas phase temperature profiles. Axial profiles were obtained at different C/O ratios and in different channels across the monolith. This work displayed that the CPO of ethanol is highly sensitive to the composition of the feeding mixture: lean fuel mixture needs to be employed to reach high syngas productivity, comparable to that predicted by thermodynamic equilibrium. The results of the experiments demonstrate that homogeneous decomposition of ethanol occurs under quasi-autothermal condition before the catalyst inlet.

Abdelrahman Mostafa et all [33] studied the catalytic partial oxidation (CPO) of ethanol with H2O co-feed in a laboratory scale adiabatic reactor on $Rh/\alpha-Al2O3$ catalysts deposited on honeycomb monoliths. In order to understand the behavior of the homogeneous and the heterogeneous reactions taking place in the CPO process, axial temperature and concentration profiles were collected using a spatially resolved sampling technique. The effect of steam co-feed was studied at C/O ratio of 0.65, varying the H_2O molar concentration in the feed from 0% to 10 %. H_2O was added to the system by replacing part of the diluting N_2, keeping a constant ethanol concentration. At increasing H_2O feed content, ethanol conversion grew close to 100 %. The water gas shift reaction was promoted, which resulted in increased H_2 yield and H_2/CO ratio. Globally, thermal

effects of the water co-feed were negligible. Moreover, a significant drop of the concentration of cracking products such as CH_4, and C_2H_4 in the initial part of the reactor was observed in the presence of water co-feed. Beneficial effects on the catalyst stability were also observed by performing tests of CH_4-CPO (a reference reacting system that, due to the sensitivity of the temperature profile to the catalyst activity, is used to detect catalyst deactivation processes in between ethanol CPO tests) and by TPO measurements on the used catalysts. Less pronounced drift of the temperature-profile in CH4-CPO and lower carbon deposition were in fact associated with the water co-feed operation of the reactor.

1.3.5 Investigated catalysts for Catalytic Partial Oxidation

Many supports have been tested for the catalytic partial oxidation of hydrocarbons such as foams, extruded monoliths and spheres [34]. Structured catalysts such as honeycomb monoliths or foams guarantees short contact times thus the reduction of the reactive volume, together with low pressure drops, homogeneous distribution of the reactants, and compactness.

Honeycomb monoliths 400/7 CPSI (channels per square inch) made of cordierite, a ceramic material in the form of $2MgO \cdot 2Al2O3 \cdot 5SiO2$, are used in the present thesis, because cordierite does not interact with the wash-coat and manifests a low thermal expansion coefficient, together with high stability at high temperatures (Tmelting=1450°C). As active phase, Rhodium is recognized as the best material from a Hydrogen selectivity point of view. It was proven that rhodium catalysts have high resistance against coke formation and low volatility [10].

The choice of wash-coat material is influenced by the active metal selected, because the interaction with the wash-coat can change the activity of the metal itself. Some wash-coat studied are ZrO2, TiO2, CeO2, Al2O3 and MgAl2O4. The wash-coat must maintain a good dispersion of the active phase and must guarantee thermal stability in extreme conditions.

The catalytic system Rh/α-Al2O3 is optimal for the methane CPO in order to keep high syngas selectivity [35]. Unfortunately, regarding production of hydrogen from heavier hydrocarbons, coke condensation of light hydrocarbons species can deposit onto active sites causing deactivation of the catalyst [36] .

Rh/MgAl2O4, on the contrary, can limit coke formation, together with other combination of desirable properties: higher melting point (2135°C), high resistance against chemical attack, good mechanical strength at both room temperature and elevated temperatures [37].

1.4 Catalyst deactivation mechanisms

1.4.1 Coking (Fouling)

Coking is the chemical deposition of carbonaceous species on the catalyst surface. The phenomenon is common to all process involving hydrocarbons. Coking leads to covering of the active sites and blockage of the catalyst pores. Formation of carbonaceous deposits progresses from the external surface up to the core of the catalytic grain. Coke deposits partially obstruct the pores and slows down the diffusion of the reactants inside the catalyst before blocking the pores [38].
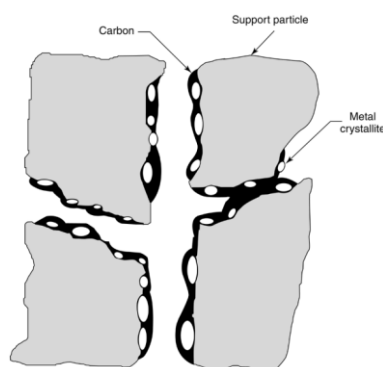
Figure 1.4 Conceptual model of coking

Several types of carbonaceous species exist. The nature of the carbonaceous deposits (coke) depends on the process conditions, the feed composition, the catalyst formulation. Deposits are usually made of high molecular weight polyaromatic structures C/H ratio between 1 and 2. Metal carbides can be also formed, or carbon can be deposited on the active phase. Carbon is formed via disproportionation of CO while coke is formed via dehydrogenation with polymerization, olefin cyclization or cracking of organic molecules [38].

Coking phenomenon can be limited by;

- optimizing the catalyst composition (addition of alkali to poison acid sites of the catalyst and to promote the carbon gasification reactions
- optimizing the pore structure
- using high partial pressure of H_2, O_2 or H_2O to promote gasification reactions
- minimizing the presence of the coke precursors in the feed

1.4.2 Sintering

Sintering is the loss of superficial area caused by the growth of the active phase crystallites. Sintering processes generally occurs at high temperatures and have high activation energy: the process temperature is the most important parameter.

Sintering of supported metals occurs via;

- migration of crystallites on the support, collision and coalescence
- migration of the particle on the surface, coalescence with bigger crystals

Factors affecting the sintering of supported metals: presence of oxidizing or reducing agents, nature of support, metal loading, form and size of the crystallites, presence of impurities [38].
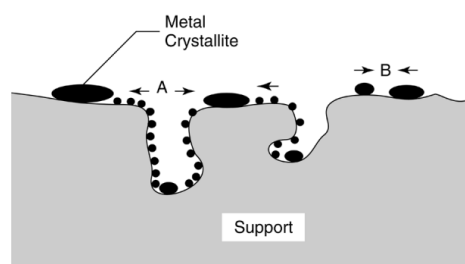
Figure 1.5 Two conceptual model of sintering

Sintering phenomena can be limited by;

- lowering the process temperature
- limiting the catalyst exposure to atmospheres favoring sintering
- adding sintering inhibitors

Moreover, there are other concepts such as poisoning, masking, phase transformation and attrition that result in catalyst deactivation; however, these concepts are not applicable for the catalysts and the working conditions that are used in this study due to the fact that pure ethanol is used as feed, and nonvolatile compounds are not seen in the system.

1.5 SOFC auxiliary power unit (SOFC-APU)

A SOFC APU system (figure 1.6) basically consist of the main components SOFC stack, reformer, heat exchanger, off-gas burner, recirculation blower and air blower. The fuel is injected into hot anode recirculation gas and fed into a catalytic reformer. In this reformer the hydrocarbon fuel is split up into H_2 and CO which is afterwards introduced into the anode part of the SOFC stack. Air is supplied via an air blower and preheated in a cathode heat exchanger, afterwards introduced into the cathode part of the SOFC stack. Within the stack an electrochemical reaction takes place were H_2 and CO with oxygen of the air are transformed into electrical power. The anode off gas still containing residual amounts of fuel is downstream the stack fed into an offgas burner, where all remaining H_2 and CO compounds are oxidized. The thermal energy of this gas stream is used to preheat the cold incoming air.
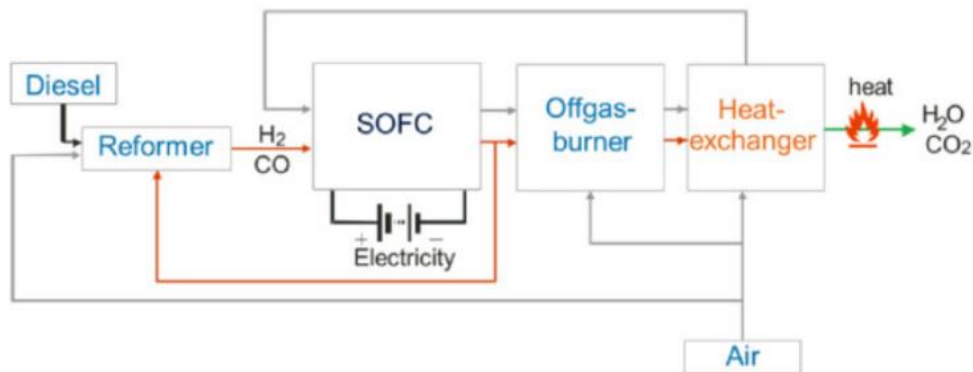
Figure 1.6 Basic SOFC APU system

The use of auxiliary power units (APU) is a promising possibility to reach a efficient way of power generation for mobile applications. The total power demand in passenger cars will triple from approximately 800 We today to an average of 2500 We and to several kWe for peak-power demands in the future [39]. Due to the low energy storage capacity of conventional lead-acid batteries, the use of electrical equipment in modern vehicles (e.g. electrical air conditioning, x-by-wire applications) is limited. The high efficiency coupled with the multiple options for the use of additional comfort functions makes a fuel cell based APU the technology of choice for an engine-independent supply of electrical power in all kind of vehicles. A time near market entry is desired to use synergetic effects in fuel cell improvement and system integration as well, and commercialization of fuel cells is expected to proceed first through SOFC systems for stationary and APU applications initially using conventional fuels [39]. In this direction, the automotive company Daimler has been working on the installation a SOFC APU applications on a heavy duty truck fuelled by diesel [40]. The main advantage of the SOFC stack technology is the use and operation with synthesis gas generated out of conventional fuels. Within the APU system, the Diesel fuel is reformed to a hydrogen and carbon monoxide containing synthesis gas. The SOFC technology allows the conversion of this hydrogen and also carbon monoxide with oxygen of the air directly into electricity. This creates a significant benefit in comparison to other fuel cell technologies like PEM , also allowing significantly high electrical efficiencies. Additionally the fuel cell APU is extremely silent and doesn't emit other harmful emissions like NOx, THC or PM [40].

Chapter 2: Description of the experimental activities

In the following chapter, the experimental techniques employed during this thesis work are described. Firstly, the experimental rig is presented, showing all the instruments mounted, their calibration procedure, and the start-up procedure of the experiments. Then, the catalyst preparation procedure is described.

2.1 CPO Rig

All the experiments are performed in a CPO lab-scale testing rig (Figure 2.1), which for safety reasons is located under fume hood, able to process high flow rate. From the P&ID (Figure 2.2), the rig can be divided into three different sections:

- Feed section;
- Reaction section;
- Analysis section.

The feed section is connected to the reaction one through stainless steel piping, having a nominal diameter of 1/4 inch. To reduce dead volumes, the piping of the analytic section has a nominal diameter of 1/16 inch.

Figure 2.1 CPO lab scale reformer
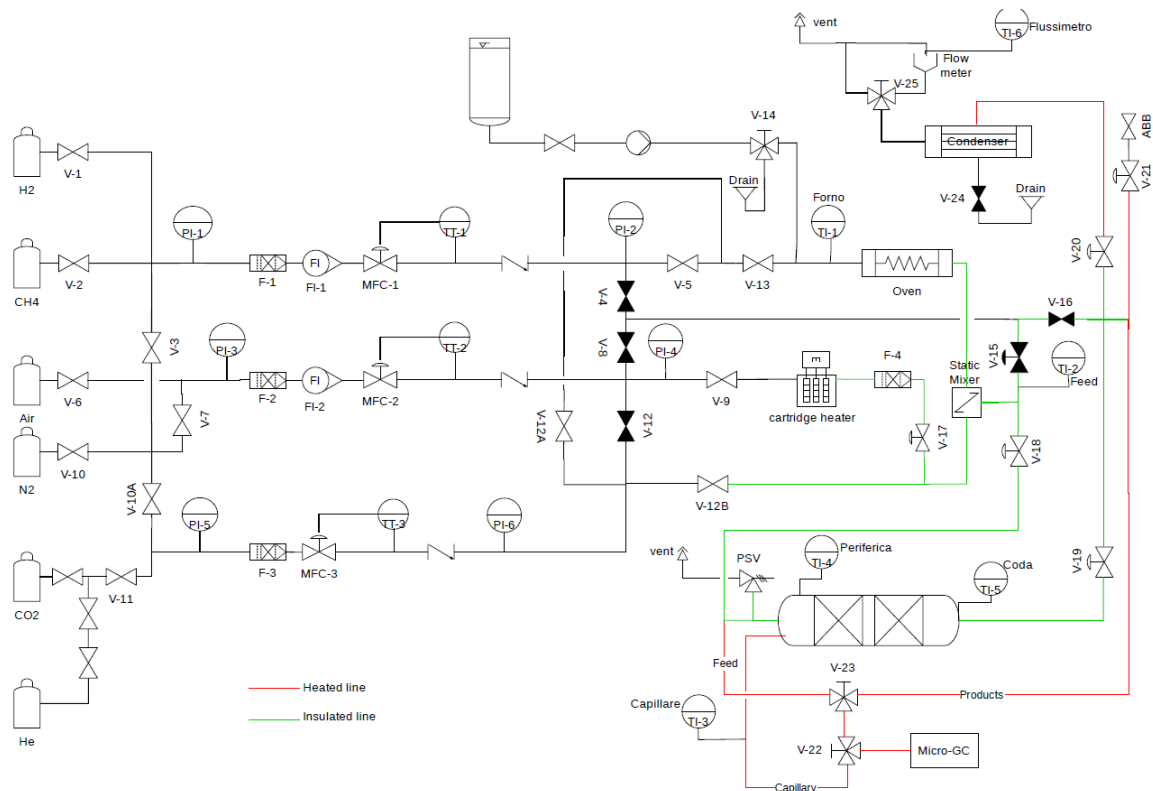
Figure 2.2 P&I diagram of the system; red lines are wrapped with heating tape

2.1.1 Feed section

The section is composed by four feed lines, through which the reactor can be fed by the following reactants:

- The first line carries hydrogen or compressed methane 4.5 (purity 99.995%), stored in cylinders outside the laboratory;
- The second line carries air SP (purity 99.5%), stored in cylinders outside the laboratory;
- The third line carries nitrogen, stored in liquid state, in tanks, outside the building;
- The fourth line carries ethanol (purity 99.5%), stored in liquid state in a burette located under fume hood.

Cylinders are equipped with pressure reducers through which the pressure reduction from the cylinders value (up to 200 bar) to a medium value (5 bar) is realized.

26

On each gas carrying line, the following elements can be found:

- Shut-off valve of the low-pressure line coming from the cylinders (placed at the beginning of the feeding line);
- Bourdon spring pressure gauge (full scale 6 bar);
- Metal mesh filter (2 μm), to protect the equipment from gas flow impurities;
- Rotameter (only for the first and second lines), which allows an instantaneous estimation of the flow rate fed by each line;
- Regulator and flow meter;
- Non-return valve.

Feed streams are regulated by Mass Flow Controller (MFC) type 5850S, which are produced by Brooks®. MFC are characterized by the following full scale:

- 15 Nl/min, for MFC1;
- 30 Nl/min, for MFC2;
- 15 Nl/min, for MFC3.

The first and the second MFC are controlled by PC through the software Brooks Smart Control. The last one is regulated with an analogical knob.

For each MFC a calibration line is required. Using this line, the gas flow rate passing through the MFC can be measured by a bubble flowmeter for different MFC openings. At this point, by performing a linear regression of the data, it is possible to plot the calibration line for each MFC. The openings of the different MFC, that guarantee the desired flow rate and inlet composition are computed starting from the calibration line of each MFC., Figure 2.3 shows the calibration line obtained for the MFC1 when the processed gas is methane.
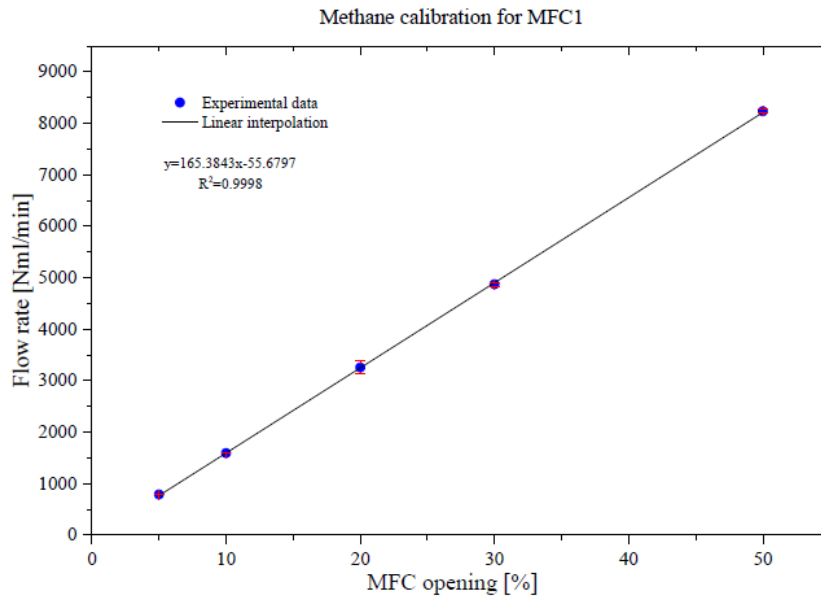
Figure 2.3 Calibration of MFC1 for methane

Liquid fuels are fed from a 250 ml burette, located under hood. The container is connected via Teflon tube (PTFE) to a Gilson® MINIPLUS 3 peristaltic pump that conveys the liquids to the reactor. Similarly to the case of MFC, a calibration line is obtained also for the pump, measuring the liquid flow rate (simply making the ratio between the volume of liquid fuel discharged from the graduated burette in a certain time and the measured time itself) corresponding to different values of the pump rotational speed.

In each experiment the flow rate of the liquids delivered by the pump to the reactor is computed starting from the knowledge of the desired flow rate of fuel in gaseous state, applying the following expression:

Equation 2.1

$$Q_{i,liq} = \frac{Q_{i,gas} \cdot MW_i}{22{,}414 \cdot \rho_i \cdot \mathcal{P}}$$

- $Q_{i,liq}$ = volumetric flow rate of liquid fuel delivered by the pump [mlliq/min];

- $Q_{i,gas}$ = desired volumetric flow rate of gaseous fuel sent to the reactor [Nlgas/min];

- MW_i = hydrocarbon molecular weight [g/mol];

- ρ_i = fuel density [g/ml];

- $\mathcal{P}$ = purity of the reactant [-]

During the previous experimental campaign performed using ethanol, the liquid flow rate required to be delivered by the peristaltic pump was near the maximum volume discharge limitation of the pump (Viton® tubes, 1mm ID, max. flow rate 10 ml/min). In order to work at lower dilution, thus higher ethanol flow rates, larger internal diameter tubes were mounted (Viton® tubes, 3mm ID, max. flow rate 55 ml/min). The increase in the diameter of the tubes ensures the delivery of the required flow rates at reasonable pump rotational speeds ensuring the reliability of the pump.

Once evaluated the required flow rate through (Equation 2.1), the rotational speed of the peristaltic pump is set, starting from the calibration line of the instrument.
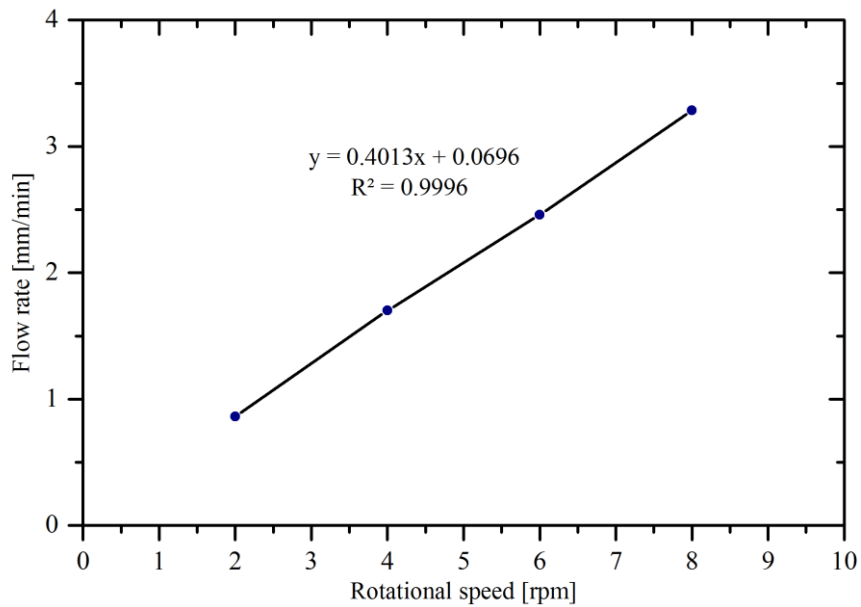
Figure 2.4 Calibration line for the peristaltic pump

Equation 2.2

$$\omega = \frac{V_{i,liq} - q}{m}$$

- ω = rotational speed of the pump [rpm]
- q = intercept of the calibration line [ml_{liq}/min]
- m = angular coefficient of the calibration line [ml_{liq}/rpm]

Upon starting the experiments with the new tube, it was seen that the tube was extending with time leading to a variation in the delivered volumetric flow rate. After several calibration experiments, the length of the tube had stabilized and the presented calibration line was obtained. The same curve was verified using ethanol and water mixture as feed stream.

During the experiments, the liquid current of fuel is flowing from the peristaltic pump towards a three-way valve (named "V-14" in Figure 2.2) through a 1/16-inch steel line. By means of this valve, it is possible to deliver fuel to the reactor, or, in case of necessity, to another steel line that discharges the liquid flow into a beaker, by-passing the reactor.

Downstream, through a three-way union, the fuel is mixed with a flow of about 1.8 Nl/min of nitrogen, coming from the first feeding line. The stream of hydrocarbon present in the biphasic mixture is then vaporized into an electric oven, composed by three independent heating sections. The evaporation process is optimized by the passage inside a 1/2-inch pipe filled by quartz spheres (3 mm diameter) mounted inside the oven. A FeCrAlloy® foam, located at the exit of the furnace, prevents the slip of these filling spheres downstream, ensuring at the same time negligible pressure losses. A K-type thermocouple, inserted into a protective sheath, provides the temperature measurement inside the oven.
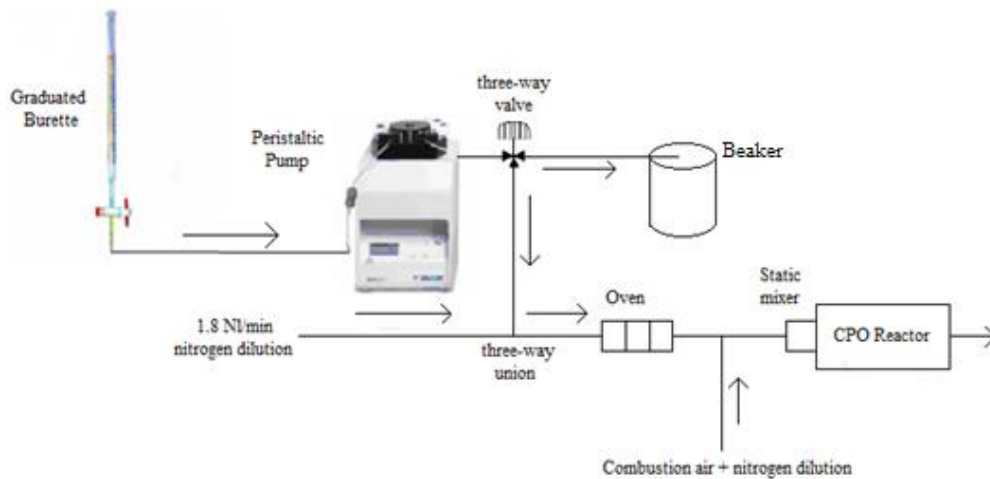
Figure 2.5 Feed section for ethanol CPO experiments

Combustion air and the remaining part of the dilution nitrogen are instead pre-heated by a cartridge (Watlow Starflow®), whose resistance can be set at maximum temperature of 650°C. Figure 2.5 shows that before being admitted to the reactor, air and vaporized fuel are mixed together in a Sulzer® static mixer.

It is fundamental to pre-heat the reactant flows before the CPO reactor, in order to ensure the complete vaporization of the liquid feed and avoid any possible condensation along the system lines ($T_{boiling, EtOH}$ = 78.37 °C). To ensure compliance with these conditions, during a previous thesis work [26], the following set of temperatures was proposed:

- Heating tape: T = 130°C;
- Heating oven: T = 170°C (for all three different sections);
- Heating cartridge: T = 200°C.

For ethanol, a different ignition procedure was developed to prevent the excessive increase of the feed temperature which may result in homogenous reactions before the reactor. Thus, the following temperatures were set:

- Heating tape: T = 160°C;
- Heating oven: T = 375°C (for all three different sections);
- Heating cartridge was shut down for this study

In addition, all the lines downstream the pre-heating system are thermally insulated with a thin ceramic layer of fiberglass and wrapped in a fiberglass tape to minimize heat dispersion.

At these conditions, the temperature of the feed (vaporized iso-octane/ethanol, air and dilution nitrogen), measured by a thermocouple placed between the static mixer and the CPO reactor, is about 100°C. This means that the experiment is conducted in pre-heated conditions (and not autothermic ones), which however can be considered representative of a real application.

It is important to highlight that in case of methane CPO experiments, both the heating oven and the cartridge are turned off, and this guarantees fully autothermic conditions (T_{feed} = 25°C).

2.1.2 Reaction section

The reaction section is made of an adiabatic reactor, able to process high flow rate. Thermal insulation is guaranteed by wrapping the reactor with a very thick layer of fiberglass tape.

To minimize coke formation, the cylindrical reactor is internally lined with quartz tube that has the following dimension:

Table 2.1: Reactor specifications

ID	OD	Length
[mm]	[mm]	[mm]
25	29	117

The quartz tube is inserted coaxially inside a 30 mm ID stainless steel cylinder, which allows the connection to the feeding lines. Two K-type thermocouples are present, in order to monitor the inlet and outlet of the flow:

- A peripheric thermocouple, inserted in a position radial to the metal casing, measures the temperature 7 cm before the reactor inlet;
- A rear thermocouple measures the temperature of the gases downstream the quartz reactor.

The reaction section hosts the catalytic bed, made of a solid support covered by a wash coat, on which the active phase is dispersed. During this thesis work, 400/7 honeycomb monoliths, made of cordierite, have been used as a support. Rhodium was adopted as a noble metal, due to its optimal properties, and was dispersed on Al_2O_4, adopted for its resistance against coke formation.

The reactor configuration was optimized in previous studies [41], and can be seen in the following figure:
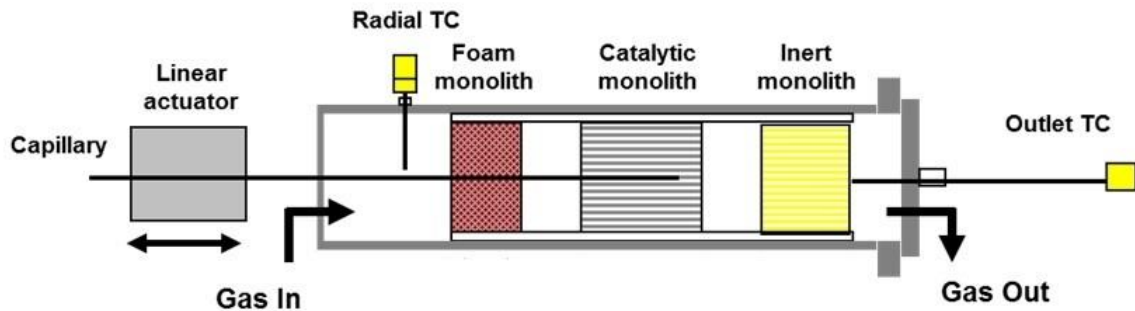
Figure 2.6 Reactor optimal configuration

- Open-cell FeCrAlloy® 15 ppi foam with its random pores shape homogeneously distributes the reactants along the reaction section and reduces axial heat losses at the same time;

- Void interspace promotes mixing of the monolith's channels;

- Active monolith, characterized by the presence of an uncovered (inert) continuous back heat shield (BHS);

- Inert monolith used to avoid axial heat losses.

To prevent any possible by-pass phenomena, the reactor and each monolith are wrapped in a tape (Promat Dalfratex®) made of continuous quartz filaments, a material which combines the flexibility of the fibrous structure and the refractory properties of quartz, guaranteeing the integrity of the material also at high temperature conditions.

To perform temperature and composition measurements along the axial coordinate of the reactor, a quartz capillary (Agilent Technology®) coated with polyimide, to confer elasticity and mechanical resistance, is introduced in one of the central channels of the catalyst. The use of fused silica capillary tubes is related to the low catalytic activity of the material, small superficial area to minimize heat losses, and is essentially transparent to radiation to allow using a pyrometer to measure the solid phase temperature. This ensures that the function of the capillary is just the protection of the instruments (Thermocouples and Optical fibers) with a negligible impact on the process itself.

The temperature capillary (ID 530 μm, OD 670 μm) is sealed at one end through oxyacetylene torch (Kemper® 55H200), to prevent leakages of gas from the reactor.

The final part of the capillary is oxidized with butane gas (RS® 513-657) to obtain the desired optical properties (fundamental for temperature measurements) and avoid any possible further oxidation during the experiments. While the concentration capillary (ID 200 μm, OD 340 μm) is not sealed at the end, allowing the micro-GC to suck a gas sample from a determined axial coordinate.

2.1.3 Ignition procedure

To light off the reactor in the absence of a heating source the procedure adopted during previous activities was followed. It consists of two phases:

- Initially the catalyst is preheated by H_2 combustion, using a H_2-rich stream with 6.5% H_2, 3.1% O_2, 90.3% N_2 in composition and 5 Nl/min as total flow rate.
  The catalytic conversion of H_2 increases the reactor temperature, as monitored with a thermocouple placed downstream the reactor.
- Once the temperature reaches a value of about 200°C, the second phase starts, during which the switching of the H_2/air feed into an EtOH/Air/N_2 feed occurs, with a total flow rate of 10 Nl/min. Exothermic reactions ignite and the reactor heating completes when reaching the steady state.
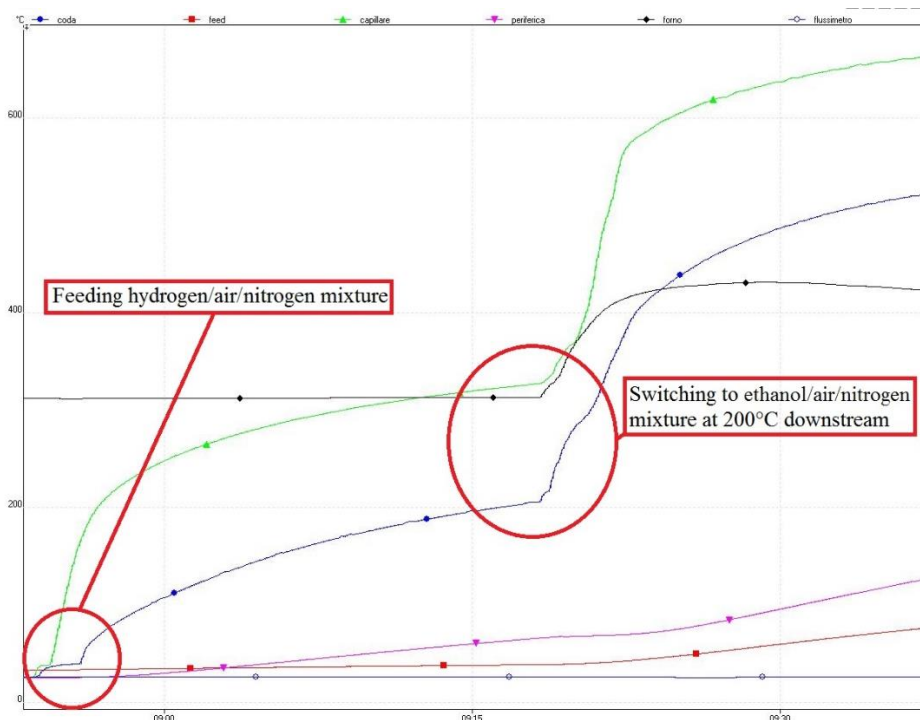
Figure 2.7 Ignition procedure, key points are highlighted in red

Switching to EtOH/Air/N_2 mixture is not performed in a single step in order to have gradual increase in reactor temperature. The decreasing trend of C/O enables a continuous reduction of the diluting nitrogen flow. During these steps, the total volumetric flow was always kept constant and equal to 10 Nl/min. This is because the mass flow controllers and the pump have regulation limits: it is not possible to adopt flow rates below 5 Nl/min, which would impose pump rpm too low, and mass flow controller openings below 1%. In case of CO_2 addition to an EtOH/H_2O mixture, N_2 is partially replaced by CO_2 in order to keep the overall dilution constant.

There is no predefined number of steps in which the ignition must be designed. Therefore, once the volumetric flow rates and temperatures are determined, the last step involves the check of the mass flow controller openings: for each step, a theoretical opening and a theoretical pump rotational speed are calculated using the calibration curves, and then the flow rates are checked using the graduated burette. An example of ignition process of EtOH/Air/N_2 with the inlet flowrate is given in Table 2.2.

Table 2.2 Ignition steps for EtOH/Air/N2 for C/O=0.75, R=0.25, yEtOH=16.1%

Steps	EtOH (Nl/min)	H_2 (Nl/min)	Air (Nl/min)	N_2 (Nl/min)	Total Flow (Nl/min)
1	0	0.35	0.75	3.9	5
Switching to EtOH/Air/N2 mixture when T reaches 200 °C					
Steps	EtOH (Nl/min)	N_2 (Nl/min)	Air (Nl/min)	N_2 (Nl/min)	Total Flow (Nl/min)
2	0.50	1.84	1.19	6.47	10
3	0.60	1.84	1.58	5.98	10
4	0.70	1.84	2.04	5.43	10
5	0.80	1.84	2.58	4.79	10
6	1.00	1.84	3.57	3.59	10
7	1.10	1.84	4.37	2.70	10
8	1.23	1.84	5.44	1.50	10
9	1.48	1.84	6.52	0.16	10

2.1.4 Analysis section

Spatially resolved sampling technique

In this thesis work, the spatial resolved technique, introduced by Horn et al. [42], has been employed, in order to measure temperature and composition along the reactor axial coordinate, maintaining at the same time almost adiabatic conditions.

As shown in Figure 2.8, the quartz capillary, inserted in a channel of the monolith, is fixed on a linear actuator (Zaber® TLA-16) controlled by a computer, with sub-millimetric accuracy. The actuator and the capillary are joined together, so it is possible to collect axial temperature profiles of the gas and solid phase, respectively, by inserting into the temperature capillary a thermocouple or an optical fiber. Alternatively, it is possible to obtain the axial composition profile of the gas flow, connecting the concentration capillary to the micro-GC through 1/16-inch steel line. The importance of this powerful method is emphasized considering that spatial data are much more important than integral steady-state data measured at the outlet, since it is possible to obtain information about the high gradients located few millimeters after the catalyst inlet, where kinetic phenomena are important.
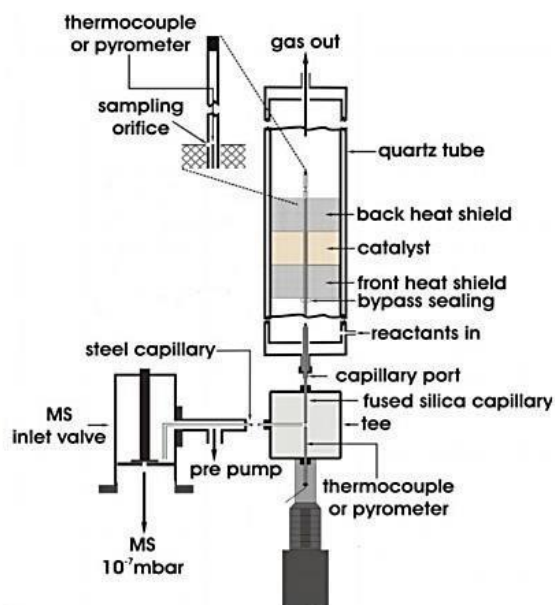
Figure 2.8: Reactor configuration employing spatially solved sampling technique

Measurement of Solid phase temperature

In this thesis work, the acquisition of solid phase temperatures profile has been possible using a pyrometer-optical fiber system. Data collection is performed with InfraWin® acquisition software. Several articles are available in literature that properly explain the functioning of these instruments when applied to honeycomb catalyst [43] . The optical fiber (Polymicro Technologies® FVP3003, OD 370 ±10 μm) is the probe which allows the transmission of the radiation emitted by the catalyst surface to the pyrometer. The cone of light that the fiber collects and transmits strictly depends on the shape of its head (Figure 2.9). As reported by Donazzi et al. [44], fibers whose head is 45° ground are preferred for sampling measures, due to their ability of capturing the radiation coming from a specific point of the surface. On the contrary, the use of fibers, whose head is flat, leads to the underestimation of hot spot temperature, as an average axial measurement is obtained.
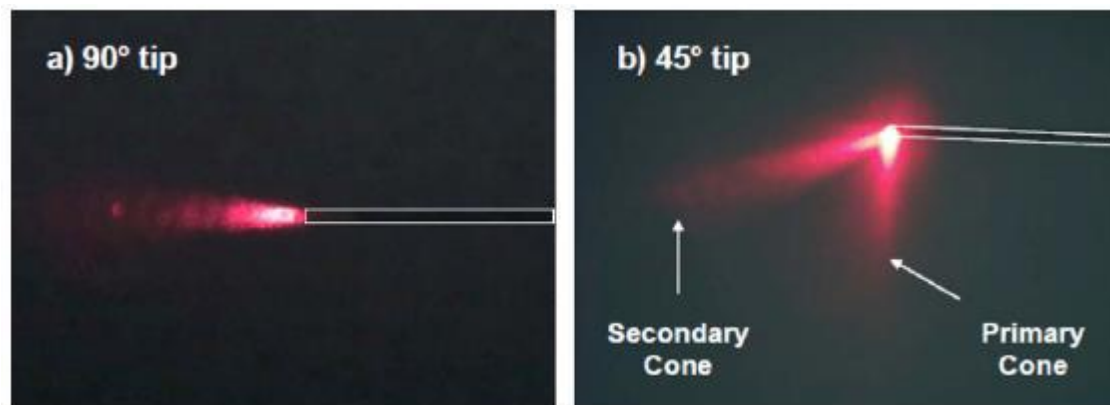
Figure 2.9 Difference between 90° and 45° acceptance cone

The optical fiber is connected to the measuring transducer of the pyrometer (LumaSense Technologies® IMPAC IGA5), composed by the following elements:

- Lens system, that collects the radiation emitted from the surface;
- Filters system, that selects the radiations whose wavelength is comprised between 1450 and 1800 nm;
- IR detector, that transducers the radiation into an electric signal;
- Signal processor.

The photons detector converts IR radiation into voltage difference, through photovoltaic effect, and acts as an electron counter. Photons coming from the optical fiber impact the surface of the detector, causing a voltage difference proportional to the number of photons involved in the process. The fundamental equation that links the voltage difference and the surface temperature is the following one:

Equation 2.3

$$V(T) = \varepsilon \cdot K \cdot T^N$$

- V(T) = voltage difference [V];

- ε = surface emissivity [-];

- K = parameter that depends on the type of pyrometer used [V/K];

- T = temperature [K];

- N = C/λt [-];

- C=1.44*10^4 [μm*K];

- λ = radiation wavelength;

In this thesis work a value for emissivity of 1 has been used

Calibration of the optical fibers

Procedure

Following the same procedure suggested by Donazzi et al. [44], a comparison between a thermocouple and the pyrometer is done over an isothermal oven over a temperature ranging from 400°C to 900°C on stagnant air. The condition of stagnant air ensures that both the gas phase and the solid phase temperatures are equal. The optical fiber used to detect the wall temp. is ground to have a tip angle of 45° as performed by Donazzi et al.

Experiment design

For this calibration a tubular catalyst support with 4 mm of outer diameter, 2 mm of inner diameter and 360 mm of length was placed in the oven wrapped with quartz tape to ensure fixing the tubular support and minimize thermal loses at the end of the oven. As the length of the support is much larger than the diameter it can be assumed as a black body and have an emissivity of 1. As reported by Donazzi et al. [44] painting the internal surface of the

catalyst support with a black paint have no significant effect on the results. Both the thermocouple and the optical fiber are placed inside a a quartz capillary (Agilent Technology®) coated with polyimide (ID 530 μm, OD 670 μm) similar to the temperature capillary, and the oven temperature is varied ranging from 400°C to 900°C.

Obtained results

The reference equation presented by Donazzi et al. [40] is $T_{actual} = 0.936\, T_{measured} + 22.9$. the obtained equation from this experiment is $T_{actual} = 0.929\, T_{measured} + 21.9$ with a difference of 2% at the expected temperature range of the CPO experiments. The deviation of obtained results from the equation given by Donazzi et al. [44] is given in Figure 2.10.
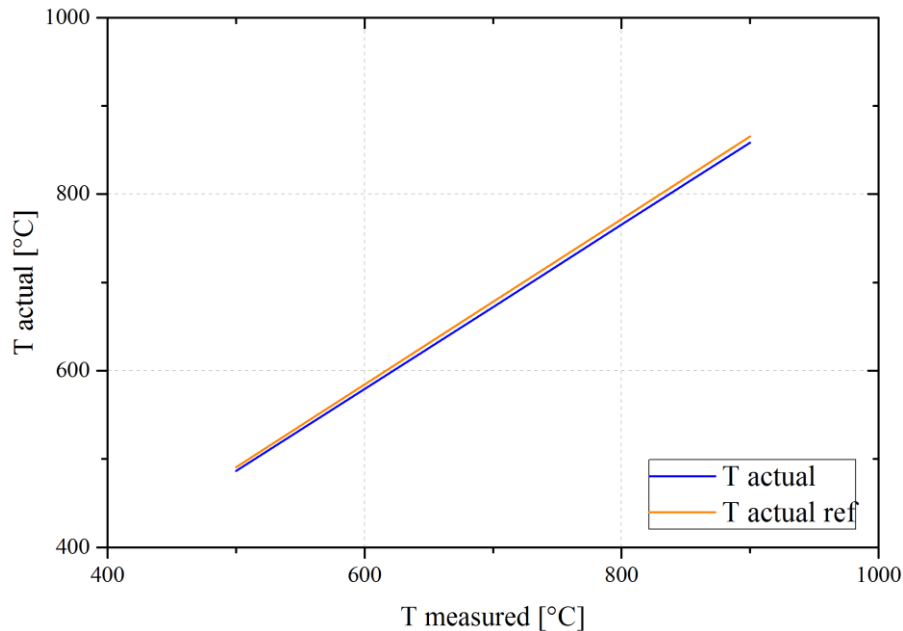
Figure 2.10 The deviation of new obtained results from reference equation

Measurement of Gas phase temperature

Gas phase temperature profiles are determined thanks to the use of a thermocouple; data are acquired by means of a software from Pico Technology®. A thermocouple consists of a pair of electrical wires of different material contained in a protective sheath. The two conductors are joined together at one end, called the hot junction. When the thermocouple is inserted in the temperature capillary, the cold junction, i.e., the other end of the instrument, is connected to a porcelain terminal block, contained inside a protective head on the linear actuator. When there is a temperature difference between junctions, a voltage difference is detected between

the two free ends of the cold junction (Seebeck effect). The equation that links the temperature difference to the potential difference is the following one:

Equation 2.4

$$\Delta T = \sum_{n=0}^{N} a_n V^n$$

- ΔT = temperature difference between the junctions [K];
- V = electric potential [V];
- a_n = parameter depending on the materials used [K/Vn];
- N = parameter depending on the desired accuracy [-]

Table 2.3: Propeties of thermocouples

Typology	Material	T_{min} [°C]	T_{max} [°C]	Sensibility [μV/°C]	OD [μm]
K	Ni-Cr/Ni-Al	-200	1200	41	250

Composition measurements

Micro gas chromatograph

For the analysis of the concentrations, a micro gas chromatograph Micro GC Fusion® (Inficon) is connected via two three-way valves to the feeding line of the reactor, the outlet of the reactor, and to the concentration capillary inserted inside the reactor during concentration tests. This arrangement allows the GC to analyze samples taken upstream, downstream, and localized samples from inside the reactor.

To obtain the localized measurements, the capillary is fixed on a linear actuator (Zaber® TLA-16), by knowing the initial position of the capillary, it is possible to construct the composition profile by taking a sample at different points along the axis of the catalyst.

During this study, Micro GC Fusion® (Inficon) was used to perform all the composition analysis. The instrument is equipped with two fused silica columns: Rt®-Molsieve 5A, which uses argon as carrier gas, and Rt®-Q-Bond which uses helium. The use of two

different columns in the GC is related to the fact that each column has a limitation towards the species that it can separate. The Rt®-Molesieve 5A is capable of separating H_2, O_2, N_2, CH_4, CO and the Rt®-Q-Bond is capable of separating CH_4, CO_2, C_2H_x, C_3H_x, H_2O, C_2H_5OH and one peak composed of air, H_2 and CO.

Table 2.4: Inficon MicroGC Fusion columns

	Rt®-Molsieve 5A	Rt®-Q-Bond
Column type	Capillary (PLOT)	Capillary (PLOT)
Length [m]	10	12
Diameter [mm]	0.25	0.25

Components separation of a sample injected onto a column is achieved through the interaction between the sample and the column coating. The less retentive the column coating is to a specific compound, the faster compound travels through the column. The two columns installed on the GC are Porous layer open tubular (PLOT) where they have small particles coated on the inner surface of the column and separation is based on gas-solid partitioning.

The choice of the type of coating and the length of the columns is particularly important. The coating affects the column's ability to detect certain elements, while the length affects the programming of the temperature ramps. The longer the length of the column, lower is the increase of °C/min.

A thermal conductivity detector (TCD) analyzes the species separated by the micro GC columns. A Wheatstone bridge, Figure 2.10, constitutes this component with two opposite branches lapped by the reference gas and the other two by the stream leaving the columns. When a sample of gas is sent to the TCD, due to the different thermal conductivity of the analyzed species with respect to the reference gas, the temperature of the lapped filaments changes, causing an alteration of the electrical resistance. Equal resistance changes, on two opposite sides, unbalance the bridge, generating an electrical signal that allows the detection of the component leaving the column.
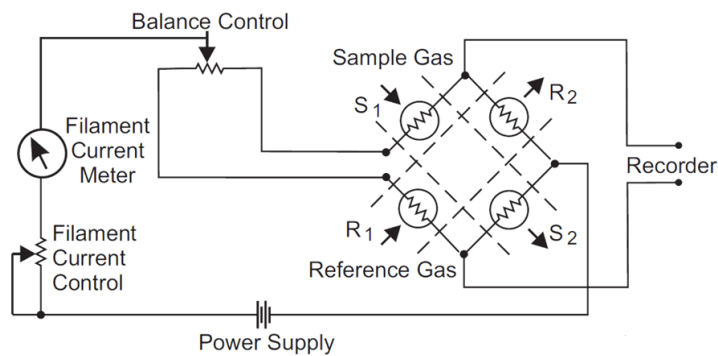
Figure 2.11 TCD scheme

Carrier gas must not contain impurities; otherwise, the analysis would be altered. That is why a filter (2 μm) and an O_2 trap have been installed on Helium and Argon transportation lines. Carrier gases are available at 4 bar, as suggested by the manufacturer, to guarantee the exact functioning of the gas chromatograph.

Gas chromatographic analysis gives as a result a chromatogram, which shows the voltage signal (expressed in μV) provided by the TCD as a function of time. Each voltage peak is caused by the detection of a species, characterized by a certain retention time, dependent just on the physical properties of the considered species.

The separated sample elutes from the GC column and enters the detection subsystem, where an electrical signal is generated based on compound type concentration. A data system controls the GC and processes the detector signal output for the sample being analyzed. As compounds elute from the GC column and are detected, a chromatogram is displayed with the detector response on the y axis and retention time on x axis.
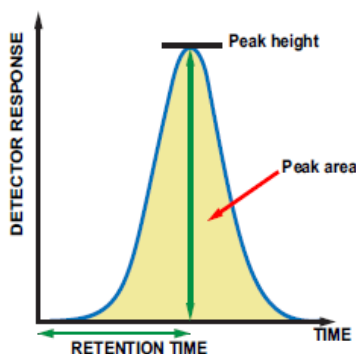
Figure 2.12 Gas chromatography response

The area under each peak is proportional to the amount of species detected. It is possible to convert the areas into species concentrations, introducing the response factors. The response factor relative to a generic i-species is defined as follows:

Equation 2.5

$$\alpha_i = \frac{Q_i}{Q_{N_2}} \Big/ \frac{A_i}{A_{N_2}}$$

- Q_i, Q_{N2} = molar flow of the i-species and nitrogen, respectively [Nl/min];
- A_i, A_{N2} = areas under the peak of the i-species and nitrogen, respectively [μV·s];

For a correct evaluation of α, the following procedure has to be followed: the flow analyzed by the Micro GC is composed by a diluent phase of a reference gas and species whose inlet and outlet molar flows are known (internal standard method). Nitrogen has been chosen to be the reference gas. For each α_i the mixture analyzed has a different concentration of the species of interest to create a calibration curve of the response factor. To create the different concentration the volumetric flow of the reference gas is varied, and the flow rates of the other species are maintained constant. This because the interference of the reference gas on the measurement is lower. The valuation of the flow rate is done with the use of a bubble flowmeter. The response factors used in this study can be found in Table 2.5.

Table 2.5: Response factors calibration results

c	column	Carrier	α_i [-]
H_2		Ar	0.090
O_2		Ar	0.867
N_2	Rt®-Molesieve	Ar	1.000
CH_4	5A	Ar	0.452
CO		Ar	1.075
Air+CO+H_2		He	
CH_4		He	0.915
CO_2		He	0.623
C_2H_4		He	0.623
C_2H_6		He	0.581
H_2O	Rt®-Q-Bond	He	1.420
C_3H_6		He	0.432
C_3H_8		He	0.409
C_2H_5OH		He	0.378

As previously mentioned, Rt®-Q-Bond column does not separate nitrogen. One peak is identified, associated to air, H_2, CH_4 and CO. On the other hand, the Molecular sieve column is able to separate these species, so it is possible to compute the relative ratios between the considered species and identify the fraction of the peak area of the Rt®-Q-Bond column associated to nitrogen (Equation 2.6). The response factors of the species separated by Rt®-Q-Bond column are referred to that fraction of the pseudo-peak associated to nitrogen.

Equation 2.6

$$A_{N_2}^U = \frac{A_{Pseudo}^U}{1 + \frac{A_{CO}^S \cdot \alpha_{CO}^{Ar}}{A_{N_2}^S \cdot \alpha_{CO}^{He}} + \frac{A_{O_2}^S \cdot \alpha_{O_2}^{Ar}}{A_{N_2}^S \cdot \alpha_{O_2}^{He}} + \frac{A_{H_2}^S \cdot \alpha_{H_2}^{Ar}}{A_{N_2}^S \cdot \alpha_{H_2}^{He}}}$$

Each analysis produces two chromatograms, one from each column. Qualitative results are converted in quantitative ones, knowing the response factors of each species, the flow of nitrogen and the value of every area detected:

Equation 2.7

$$Q_i = \frac{\alpha_i \cdot Q_{N_2} \cdot A_i}{A_{N_2}}$$

- Q_i= molar flow rate of the i-species [Nl/min]

The molar flow rate of each species is computed according to Equation 2.8:

Equation 2.8

$$F_i = \frac{Q_i}{\frac{RT}{P}}$$

- F_i= molar flow rate of the i-species [mol/min]
- R= 8,314 m^3Pa/K/mol (universal gas constant)
- T= 273,15 K
- p= 101325 Pa

Consequently, it is possible to evaluate the molar fraction of each species in the mixture at the outlet of the reactor:

Equation 2.9

$$y_i = \frac{F_i}{\sum F_i}$$

Eventually, reactant conversion and selectivity of each species referred to C-molar flow and H-molar flow are calculated:

Equation 2.10

$$\chi_{fuel} = 1 - \frac{F_{fuel,out}}{F_{fuel,in}}$$

Equation 2.11

$$\chi_{O_2} = 1 - \frac{F_{O_2,out}}{F_{O_2,in}}$$

Equation 2.12

$$S_{i,C} = F_{i,out} \cdot \frac{nC_i}{F_{C,converted}}$$

Equation 2.13

$$S_{i,H} = F_{i,out} \cdot \frac{nH_i}{F_{H,converted}}$$

To verify the quality of each analysis, atomic balances, referred to carbon, hydrogen and oxygen are defined:

Equation 2.14

$$B_C = \frac{\sum F_{i,out} nC_i}{F_{C,converted}}$$

Equation 2.15

$$B_H = \frac{\sum F_{i,out} nH_i}{F_{H,converted}}$$

Equation 2.16

$$B_O = \frac{\sum F_{i,out} nO_i}{F_{O,converted}}$$

- nC_i = number of carbon atoms of the i-species
- nH_i = number of hydrogen atmos of the i-species;
- nO_i = number of oxygen atoms of the i-species;
- $F_{C, converted}$ = molar flow of carbon converted;
- $F_{H, converted}$ = molar flow of hydrogen converted;
- $F_{O, converted}$ = molar flow of oxygen converted;

By definition, atomic balances should be as much as possible close to unity.

Analysis methods and the output chromatogram

Figures 2.13 and 2.14 shows the used analysis method parameters for the ethanol tests, where Figure 2.13 presents the parameters set for column A (Rt®-Molesieve 5A) and Figure 2.14 shows the parameters used for column B (Rt®-Q-Bond).
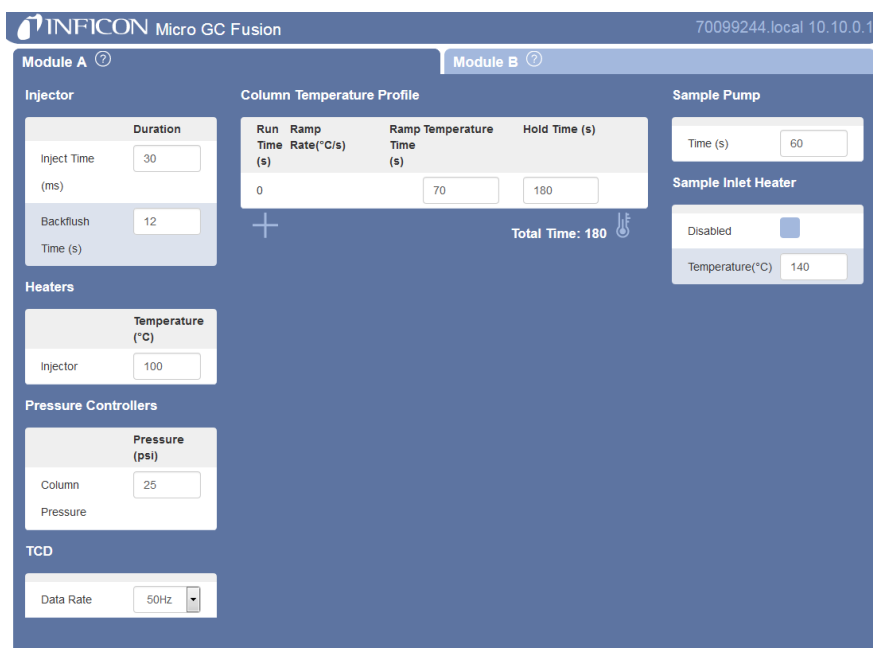
Figure 2.13 The parameters of the method for ethanol analysis for column A
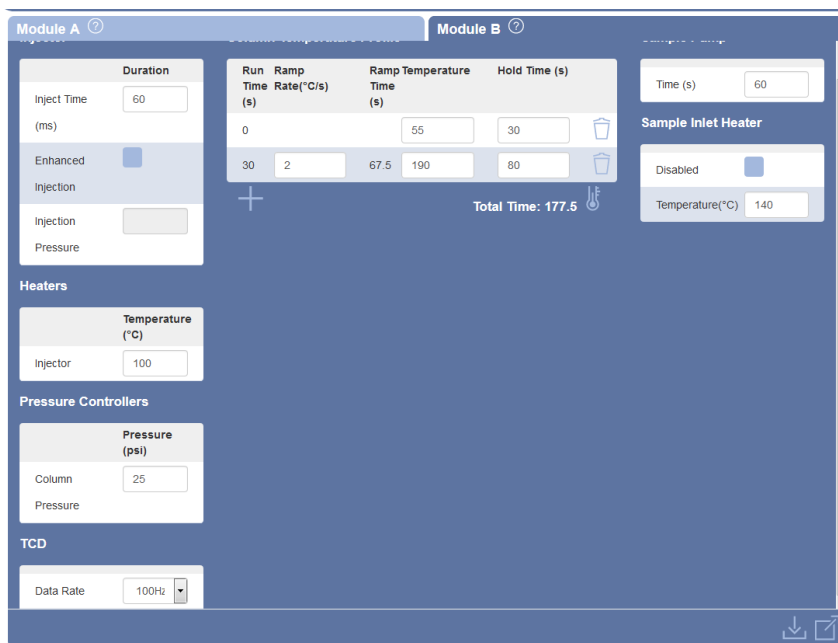
Figure 2.14 The parameters of the method for ethanol analysis for column B

As shown from the parameters, the method includes a temperature ramp which allows better identification of the species. Temperature of each column is given in Figure 2.15.
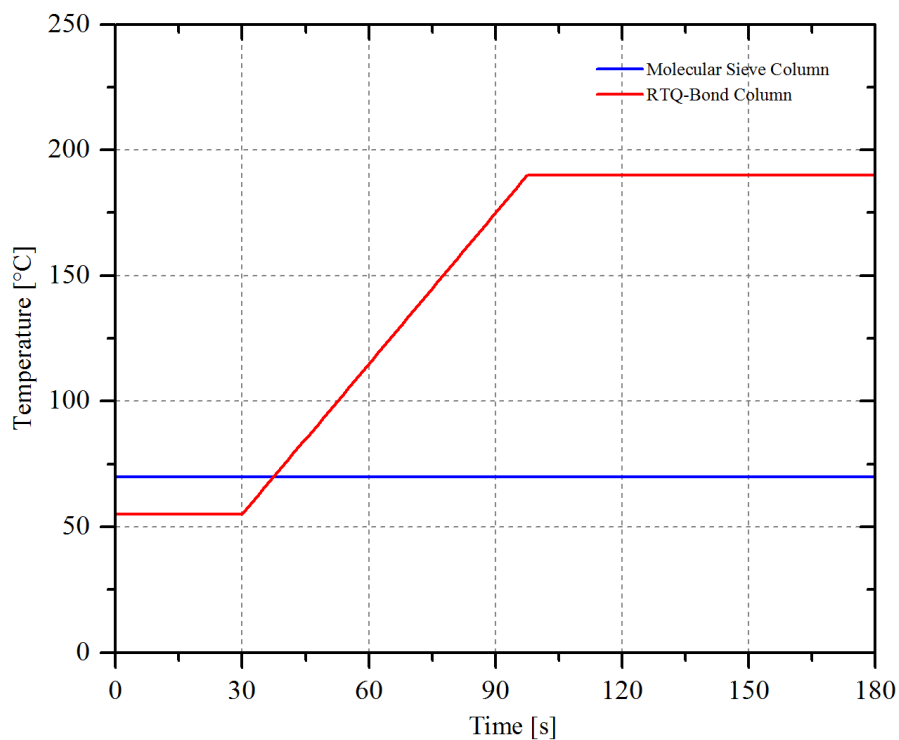
Figure 2.15 GC columns temperatures during analysis

For the methane tests, a shorter analysis time is required so the parameters used for the analysis method are as presented in Figures 2.16 and 2.17.
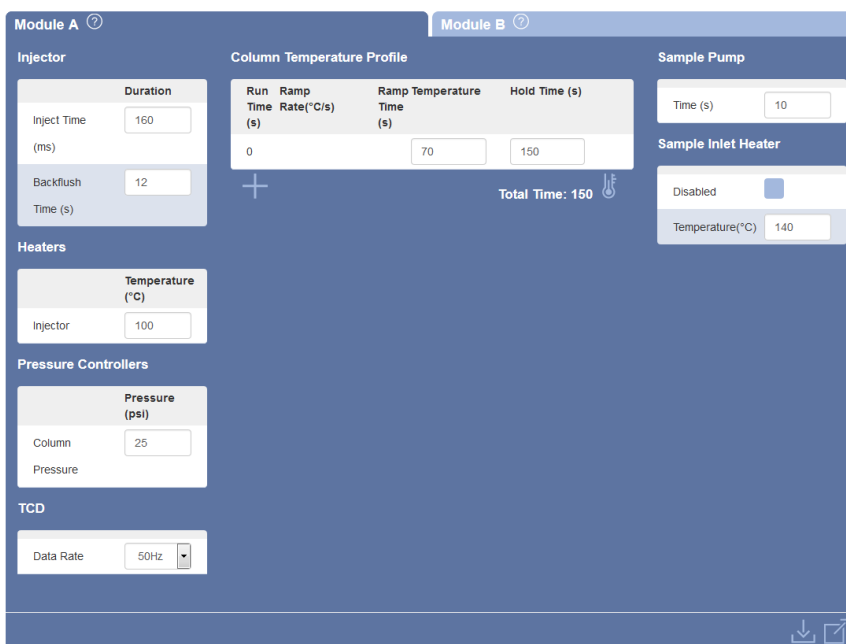
Figure 2.16 The parameters of column A for methane analysis
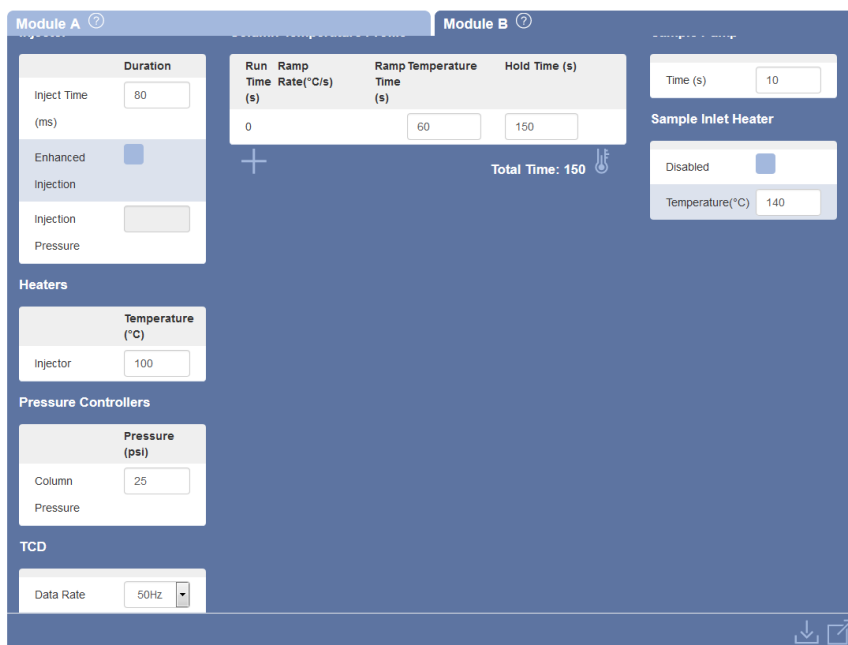
Figure 2.17 The parameters of column B for methane analysis

The output chromatograms of a methane characterization test, as shown in Figure 2.18 and Figure 2.19, identify the different peaks related to the different components.
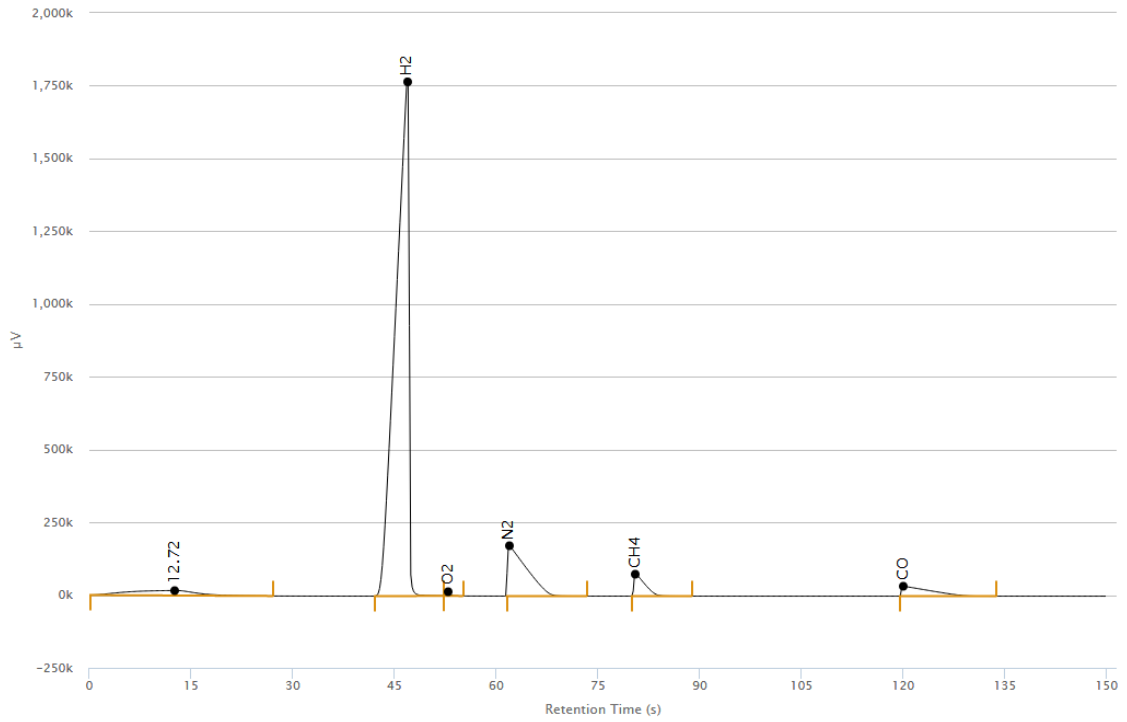
Figure 2.18 The output sample chromatogram for column A
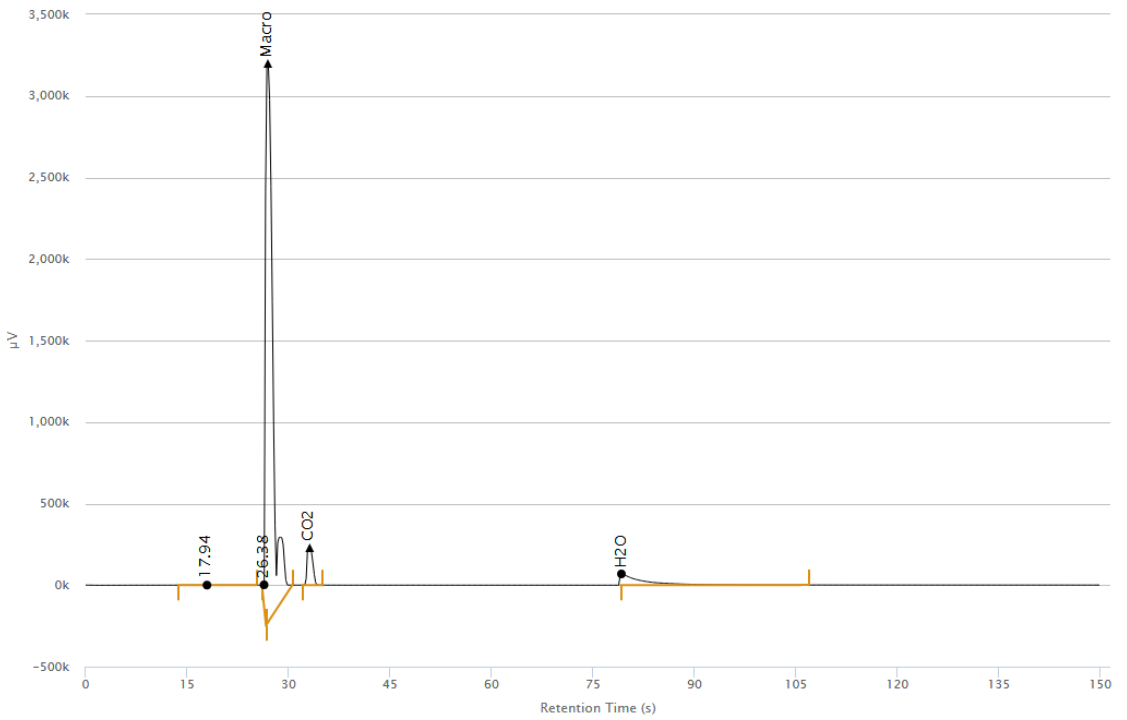
Figure 2.19 The output sample chromatogram for column B

The output chromatograms of an ethanol test, as shown in Figure 2.20 and Figure 2.21, identify the different peaks related to the different components.
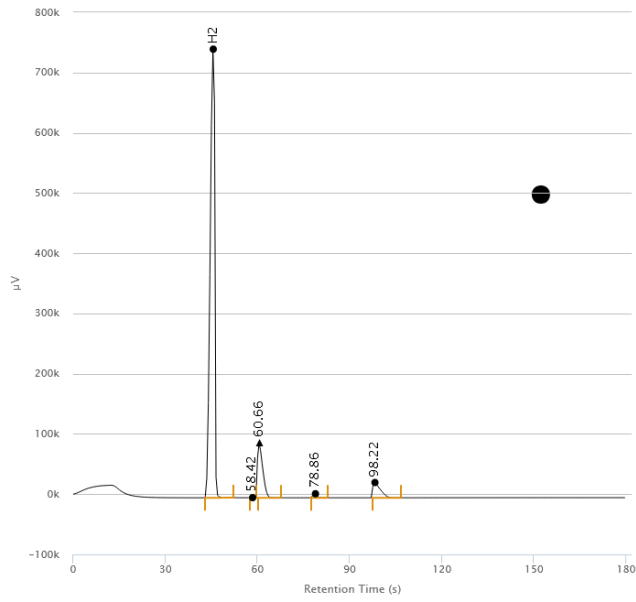
Figure 2.20 The output sample chromatogram for column A for EtOH test
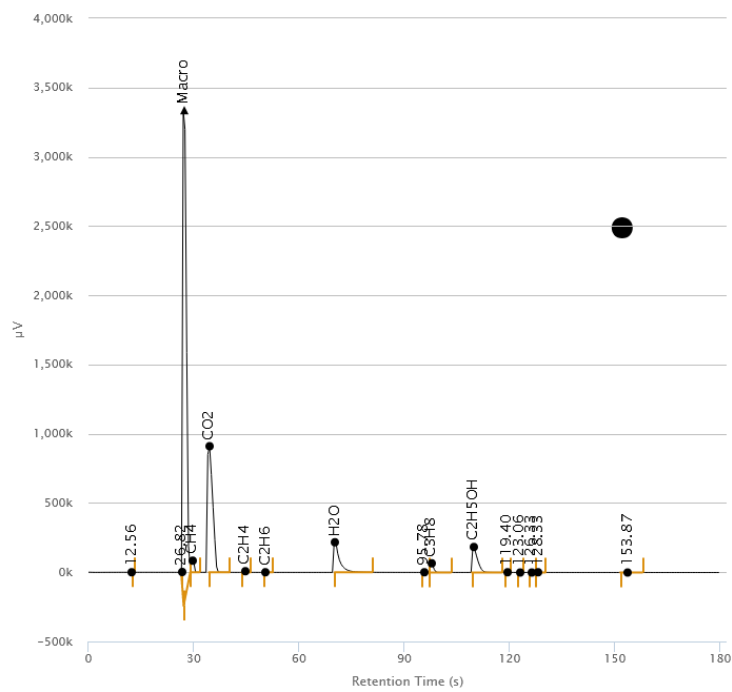
Figure 2.21 The output sample chromatogram for column B for EtOH test

2.2 Catalyst preparation and characterization

In this section the procedures followed for catalyst preparation are described, along with the characterization technique.

2.2.1 Catalyst preparation

The preparation of $Rh/\alpha-Al_2O_3$ catalyst is described in this section. The choice of rhodium as the active phase for the partial oxidation of light hydrocarbons is due to its high activity, stability, and reduced tendency to form carbon deposits. The catalytic powders have been prepared through the dry impregnation (incipient wetness) of the support ($\alpha-Al_2O_3$) with a solution containing rhodium nitrate.

Preparation of the support of $\alpha-Al_2O_3$

The support of $\alpha-Al_2O_3$ was prepared by calcination of the commercial alumina PURALOX Sba-200 (Sasol). The material, as supplied by the manufacturer, consists of 96.9% of $\gamma-Al_2O_3$ with traces of impurity; the surface area is 202 m^2/g. The calcination batch has been prepared at 1100°C.

The $\gamma-Al_2O_3$ was calcined by performing a thermal scale at a speed of 1°C/min and a hold of 10 h when the desired temperature was reached; at the end of hold, the sample was cooled by lowering the temperature to room temperature at a rate of 2°C/min. The choice of calcination temperature is linked to the fact that at 1100 °C the phase transition of γ-to-θ alumina to α is complete.

Slurry preparation

The procedure for the preparation of the catalytic slurry consists in the use of a ball milling to grind and homogenize the catalytic powders. A PTFE container was filled with the powders, nitric acid, deionized water and zirconia spheres. The latter was put in a ceramic jar with a 30° angle between the axis of the two containers. The ceramic jar lies on two rotating cylinders. A rotational speed of 60 rpm was set. After 24 hours, a homogeneous slurry is obtained.

The formula followed for the preparation of the slurry for Rh/ α-Al$_2$O$_3$ powders, proposed by Cristiani et al. [45], has been slightly modified, as the original one has been developed for open-cell foams and not for honeycomb monoliths.
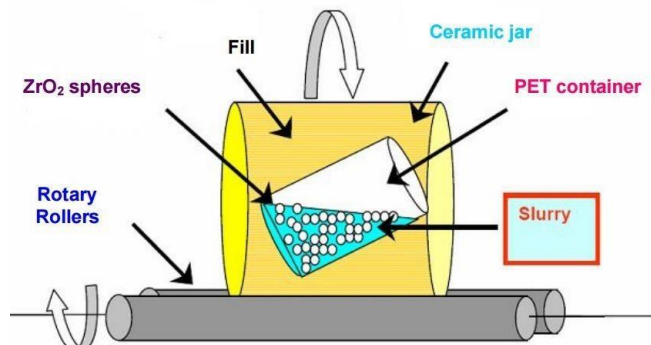
Figure 2.22 The ball milling process

Table 2.6 shows the amount of nitric acid, deionized water and zirconia spheres (specific to the powders mass) used.

Table 2.6: Slurry recipe

Catalytic powders	N_{HNO_3} [mmol/g$_p$]	V_{H_2O} [ml/g$_p$]	m_{ZrO_2} [g/g$_p$]
Rh/αAl2O3	2	1.7	8

Slurry deposition on honeycomb monoliths

Cordierite 400/7 honeycomb monoliths (2.5 cm diameter) have been used as supports for the slurry deposition.

Cordierite physical properties are reported below:

- Density: 2300 kg/m^3;
- Thermal conductivity: 2.5 W/mK;
- Specific heat: 925 J/kgK;

The slurry has been deposited on the monolith by dip-coating technique: after a quick immersion, the slurry level raises inside the channels, because of capillarity. Then the excess slurry is eliminated by a jet of air at a pressure of 7 bar. In this way, a homogenous catalytic layer can be obtained. Later on, the catalysts were placed in an oven at 280°C for 5-10 min (flash drying process) to promote the adhesion between the cordierite substrate and catalytic phase. The catalyst mass has been evaluated by subtracting to the final weight of the monolith the weight of the monolith covered only by the primer.
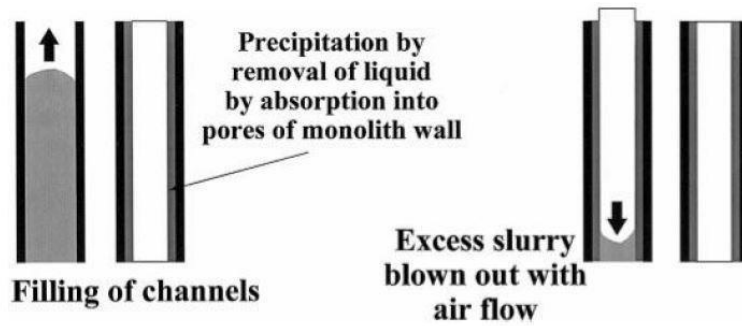
Figure 2.23 Dip-coating process

Table 2.7: Catalysts specifications

Monolith	Catalyst	L_{cat} [cm]	L_{BHS} [cm]	m_{cat} [g]	t_{cat} [µm]
NE3	Rh/α-Al$_2$O$_3$	4.25	1.95	0.60	14
NE5	Rh/α-Al$_2$O$_3$	4.28	2.34	1.07	31
NE6	Rh/α-Al$_2$O$_3$	4.34	2.14	1.29	33

The catalytic thickness and empty grade can be evaluated as follows:

Equation 2.17

$$m_{cat,ch} = \frac{m_{cat}}{n_{channels}} = \frac{m_{cat}}{D_{channel} \cdot \frac{\pi}{4} \cdot D_m^2}$$
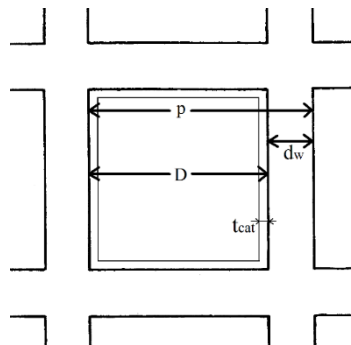
Figure 2.24 Monolith geometrical parameters

Where D_m is in inch. Some proprieties have been defined in order to calculate every geometric characteristic of the cannel:

- Pitch: defined as the sum between the measurement of the channel (D) and the cordierite thickness (d_w); It can be calculated by CD, considering the following equation:

Equation 2.18

$$\text{pitch} = \frac{2.54}{\sqrt{D_{channel}}}$$

- $V_{cat,channel}$: volume of the catalyst inside each channel, considering the catalyst density $\rho_{cat} = 1.38 \text{ g/cm}^3$:

Equation 2.19

$$V_{cat,channel} = \frac{m_{cat}}{\rho_{cat} \cdot n_{channels}}$$

Equation 2.20

$$D = p - d_w = \text{pitch} - d_w = 1.0922 \text{ mm}$$

- t_{cat}: thickness of catalyst on the support:

Equation 2.21

$$t_{cat} = \frac{D - \sqrt{D^2 - \frac{V_{cat,channel}}{L_{cat}}}}{2}$$

- $D_{h,channel}$: width of the channel without t_{cat}, defines the effective flow area:

Equation 2.22

$$D_{h,channel} = D - 2t_{cat}$$

As a final remark, the void fraction (ε) is evaluated as follows:

Equation 2.23

$$\varepsilon = \frac{D_{h,channel}^2}{\text{pitch}^2}$$

2.2.2 Temperature Programmed Oxidation (TPO)

The TPO plant, as shown in Figure 2.25, is under fume hood for safety reasons and presents stainless steel lines, having a nominal diameter of 1/4 inch. The plant is divided into feed, reaction and analysis sections.

Figure 2.25 Photo of the TPO plant

Feed section

The feed section includes five principal lines with shut-off valves, Bourdon spring pressure gauge (upstream and downstream of the mass flow controllers), filters to capture impurities in the gas, mass flow controllers MFCs (Brooks®, 5850S). The latter are controlled by a control unit (Brooks®).

The used feed gases are controlled by the following MFCs:

- Air line is controlled by 100 Nml/min MFC
- Nitrogen line is controlled by 500 Nml/min MFC

Reaction section

The reaction section is composed by an oven and a quartz reactor connected to the stainless-steel lines through proper connections. This part of the plant can be isolated and the flow directed towards a bypass line.

The oven (Carbolite) has a horizontal position, internal diameter equal to 60 mm and length equal to 450 mm. The two lateral electric resistances work together with the central one in order to keep the set temperature uniform over the entire length of the oven; PID regulators that use N-type thermocouples as sensors monitor the temperatures of each zone.

Two K-type thermocouples, 600 mm long and 1 mm in diameter, are made to slide inside the quartz tube and a mullite tube placed next to the reactor: in this way, it is possible to measure the temperature profiles along the axis for the catalytic bed and for the internal oven environment.

The sample is placed inside the quartz reactor as shown in Figure 2.26 with 2 quartz wool beds upstream and downstream the sample to prevent it from moving. The thermocouple is fixed inside the quartz tube at the centre of the sample.
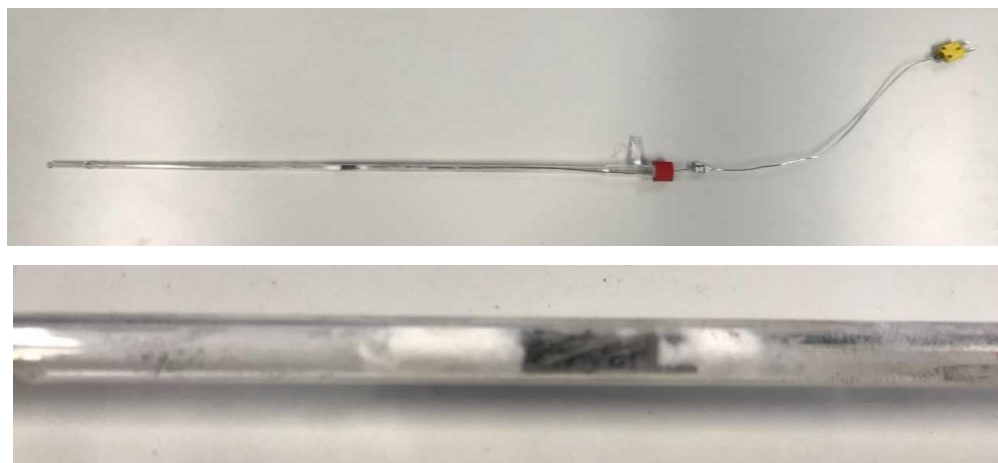
Figure 2.26 TPO quartz reactor

Analysis section

A micro-gas chromatograph (Agilent 3000A) is connected to the plant to analyze the composition of the gas flow rates. The retention times and response factors for the different species are reported in Table 2.8.

Table 2.8: Retention times and response factors of the species analyzed by the GC

Species	Column	Retention time [s]	Response factor [-]
H_2	A	32.73	0.096
O_2	A	38.49	0.866
N_2	A	44.06	1
CH_4	A	57.44	0.463
CO	A	72.03	1.052
Air+CO	B	20.98	-
CH_4	B	22.25	-
CO_2	B	28.95	0.828
H_2O	B	158.56	1.861

Analysis methods and the output chromatogram

In the rig an Agilent 3000A micro-gas chromatograph equipped with two capillary columns is installed: column A (PlotQ) uses helium as carrier, while column B (molecular sieves) uses argon. The method parameters of the columns are shown in Figure 2.27. In order not to alter the analyses, the transport gas must not contain impurities: therefore, water and oxygen traps and dust filters have been installed upstream.
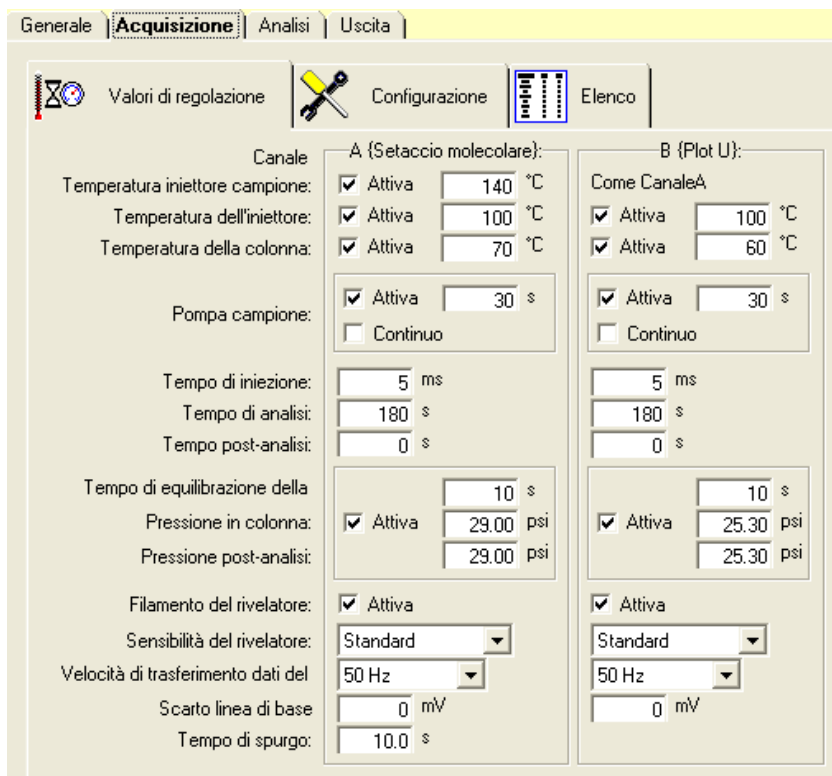
Figure 2.27 The method parameter of columns A and B for gas chromatogram used for TPO analysis

The output chromatogram, as shown in Figure 2.28, identifies the different peaks related to the different components.
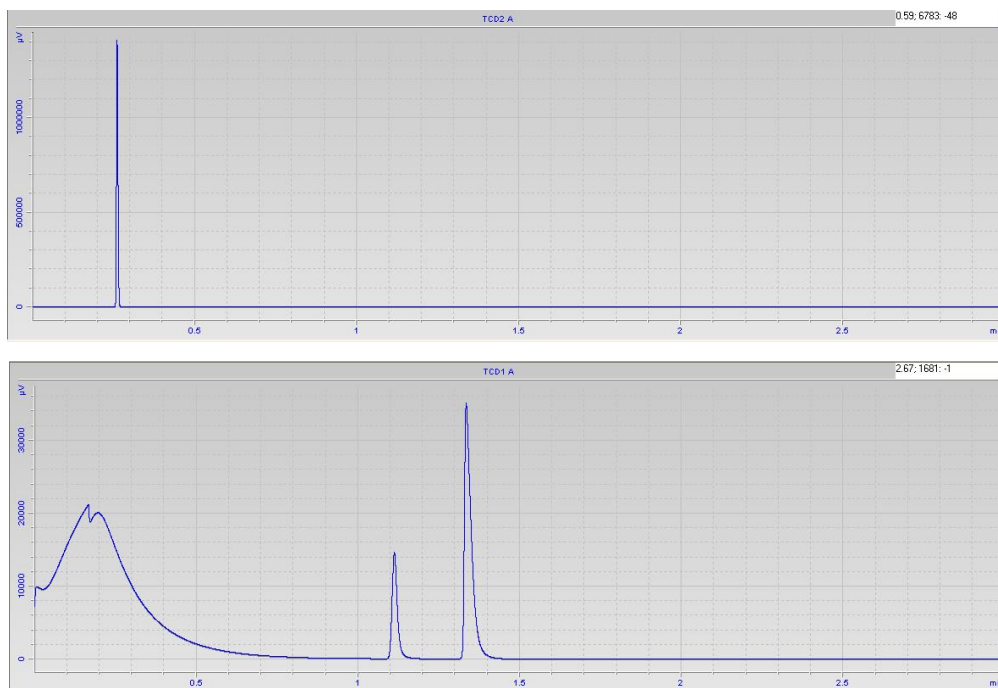
Figure 2.28 Output sample chromatograph for Agilent 3000A micro-gas chromatograph

TPO procedure

TPO is performed by the progressive heating of a sample from each part of the monolith. Starting from the ambient temperature up to 700°C the sample is heated with a rate of 2°C/min while being exposed to a flow rate of air equal to 30 Nml/min. The CO_2 flow rate developed by the combustion of the coke deposited onto the catalyst is measured (μmol/min). It is important to highlight that the moles of CO_2 obtained in the experiment is equivalent to the moles of coke deposited onto the catalyst surface. Through the integration of the CO_2 flow rate, it is possible to have an idea of the total number of μmoles of coke that are present on the sample taken under consideration.

Chapter 3: CPO of Ethanol-water mixture with CO₂ cofeeding

3.1 Thermodynamic analysis

In order to identify the working feed condition to maximize the hydrogen production such that the expected adiabatic temperature does not exceed the threshold of catalyst deactivation by sintering (850-900°C, according to previous experiments [46]) and the formation of solid C is avoided, a thermodynamic analysis is performed.

Equilibrium compositions is calculated by Gibbs free energy minimization using a code written in Matlab R2018b language. The analysis is performed at constant enthalpy and pressure (adiabatic reactor), by assigning an inlet temperature of 100 °C and varying the C/O ratio, the dilution of the feed, and the molar fractions of water carbon dioxide in the feed. The analysis includes the gas phase species $C_2H_5OH, CH_3CHO,\ CH_4,\ C_2H_2,\ C_2H_4, C_2H_6,$ $CO, CO_2, H_2, H_2O, N_2, O_2,$ and the possible formation of solid graphitic carbon.

The assumption of adiabatic conditions involves the simultaneous solution of the enthalpy balance and the determination of the Tout adiabatic:

Equation 3.1

$$H_i(T) = \Delta H°_{F,i}\left(T_{ref}\right) + \int_{T_{ref}}^{T} \tilde{C}_{Pi}.\,dT$$

Equation 3.2

$$\dot{H}(T) = \sum_{i}^{NC} n_i.\,H_i(T)$$

Equation 3.3

$$\dot{H}_{in}\left(T^{in}\right) = \dot{H}_{out}\left(T_{adiabatic}^{out}\right)$$

The parameters used for this study are C/O ratio, Equation 3.4, defined as the molar flow of the carbon of ethanol divided by the molar flow of oxygen in both ethanol and air, R ratio, Equation 3.5, defined such that H_2O and CO_2 are treated as a complementary gases, added to the air/ethanol feed, similarly to the extra N_2 feed, and H_2O/CO_2, Equation 3.7, ratio defined as the molar flow rate of H_2O divided by the molar flow rate of CO_2 in the feed. The Water molar fraction is defined as Equation 3.6.

Equation 3.4

$$\frac{C}{O} = \frac{2n_{C_2H_5OH}}{n_{C_2H_5OH} + 2n_{O_2}}$$

Equation 3.5

$$R = \frac{n_{N2,dil} + n_{H2O} + n_{CO2}}{n_{C2H5OH} + n_{AIR}}$$

Equation 3.6

$$y_{H_2O} = \frac{n_{H_2O}}{n_{C_2H_5OH} + n_{N_2}^{air} + n_{O_2}^{air} + n_{N_2,dil}}$$

Equation 3.7

$$\frac{H_2O}{CO_2} = \frac{n_{H2O}}{n_{CO2}}$$

In previous studies [33], the effect of N2 dilution on the ethanol CPO and the effect of water co-feeding to the process were evaluated and are presented in figure 3.1 and figure 3.2 respectively. These thermodynamic studies are extended to include the effect of CO_2 co-feed into the water-ethanol CPO system and the results are presented in figure 3.3

3.1.1 Effect of N₂ dilution
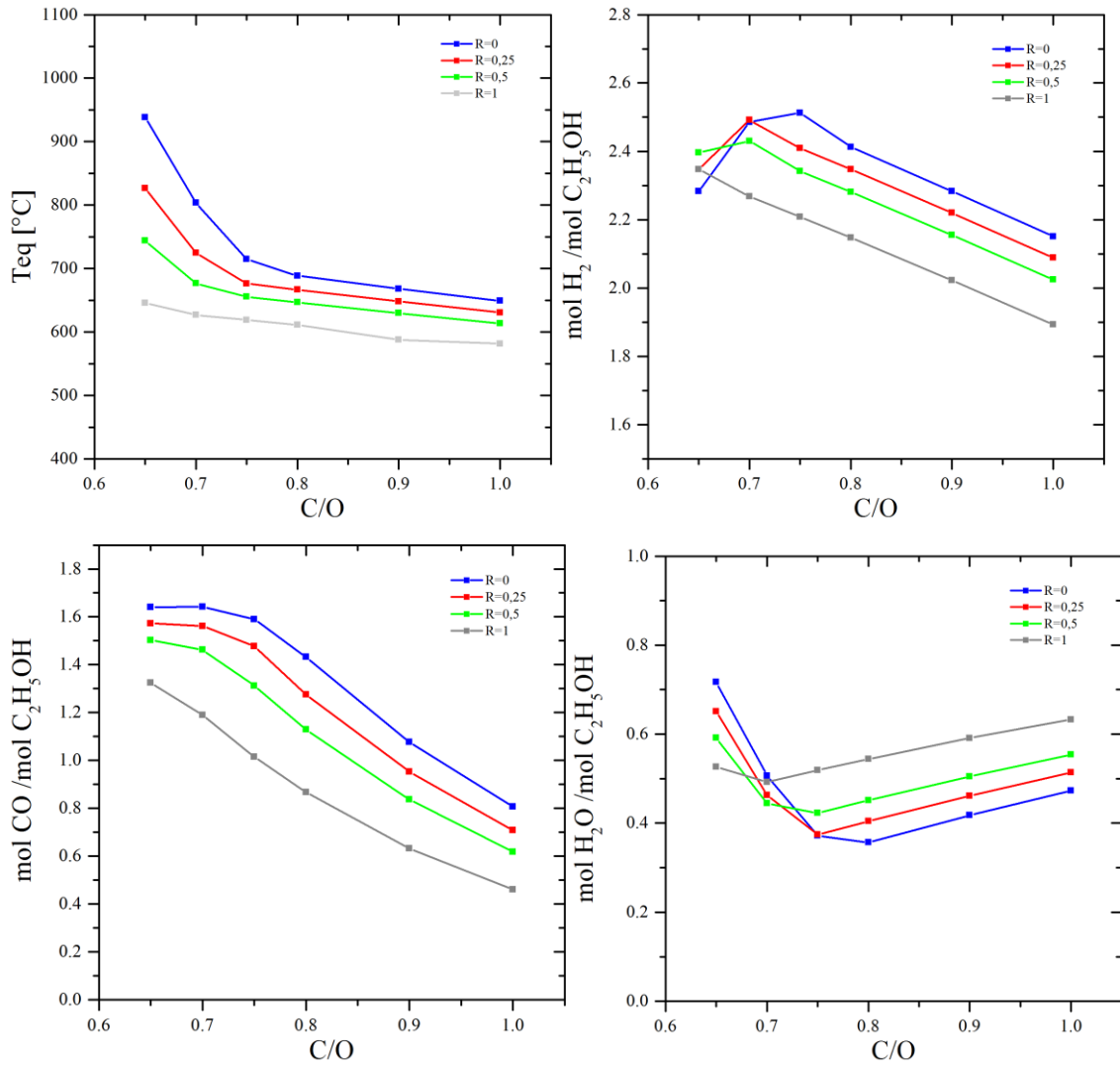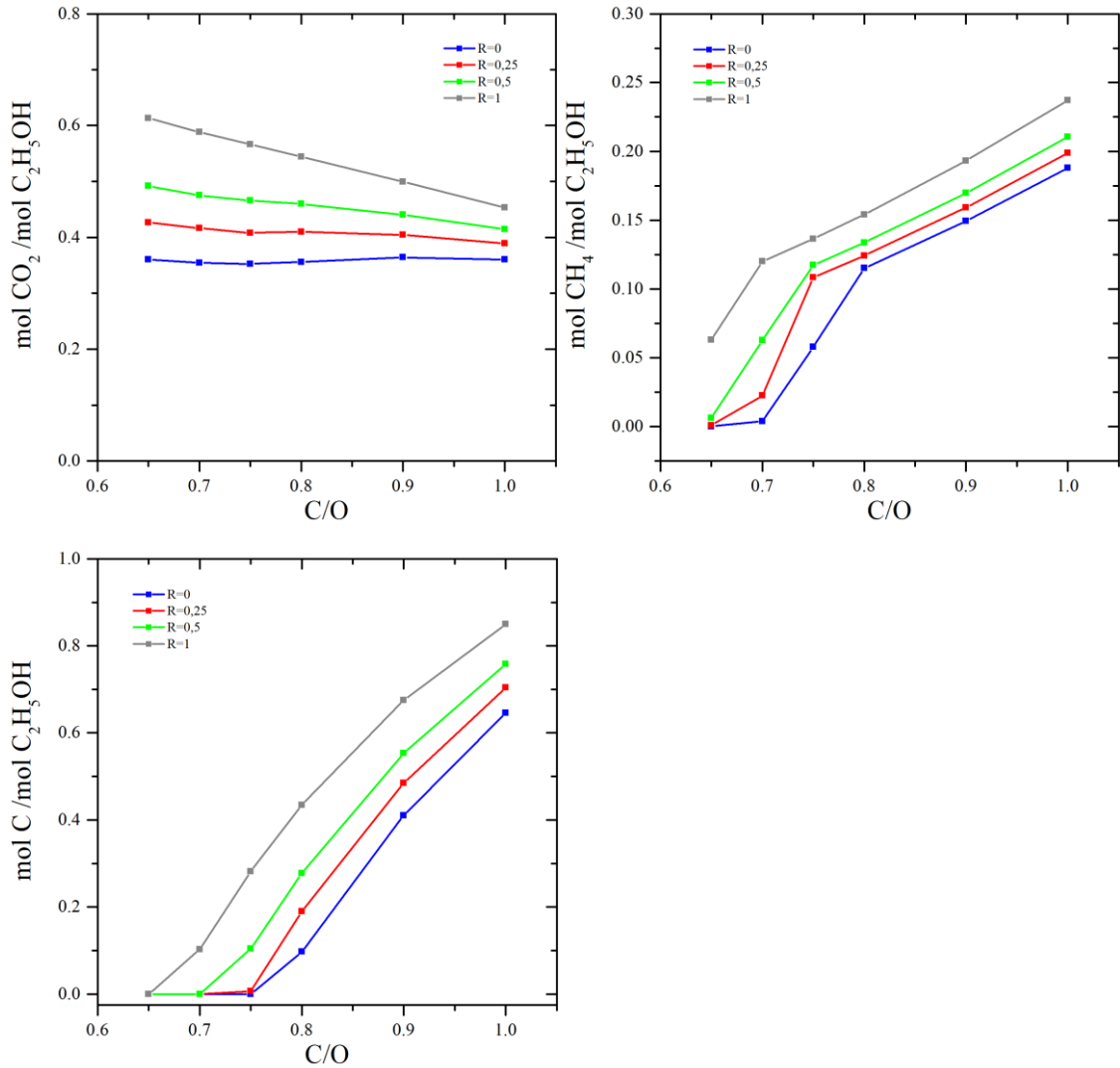
Figure 3.1 Thermodynamic analysis: Effect of Nitrogen dilution on the equilibrium adiabatic temperature and species' molar fraction

Starting with the effect of C/O ratio, a progressive decrease of the adiabatic equilibrium temperature is observed with the increase of C/O. The drop of the equilibrium temperature is accompanied by an increase in CH_4 equilibrium value and solid carbon formation which might be related to a lower extent of the endothermic steam reforming and gasification reactions. H_2 equilibrium value shows a maximum at C/O of 0.75 without any dilution, R=0, and it starts to decrease on increasing the C/O. For the solid carbon formation, the equilibrium value shows remarkable carbon formation with C/O higher than 0.75.

Following the effect of dilution, as the R ratio increases, the equilibrium temperature decreases as well as the max production of H_2. The peak of H_2 production is shifted towards lower C/O ratios on increasing the R ratio showing that it is fully controlled by the equilibrium temperature. The effect of dilution on carbon deposition is intense, limiting the safety working condition to low C/O ratios as R increases.

3.1.2 Effect of H2O co-feeding
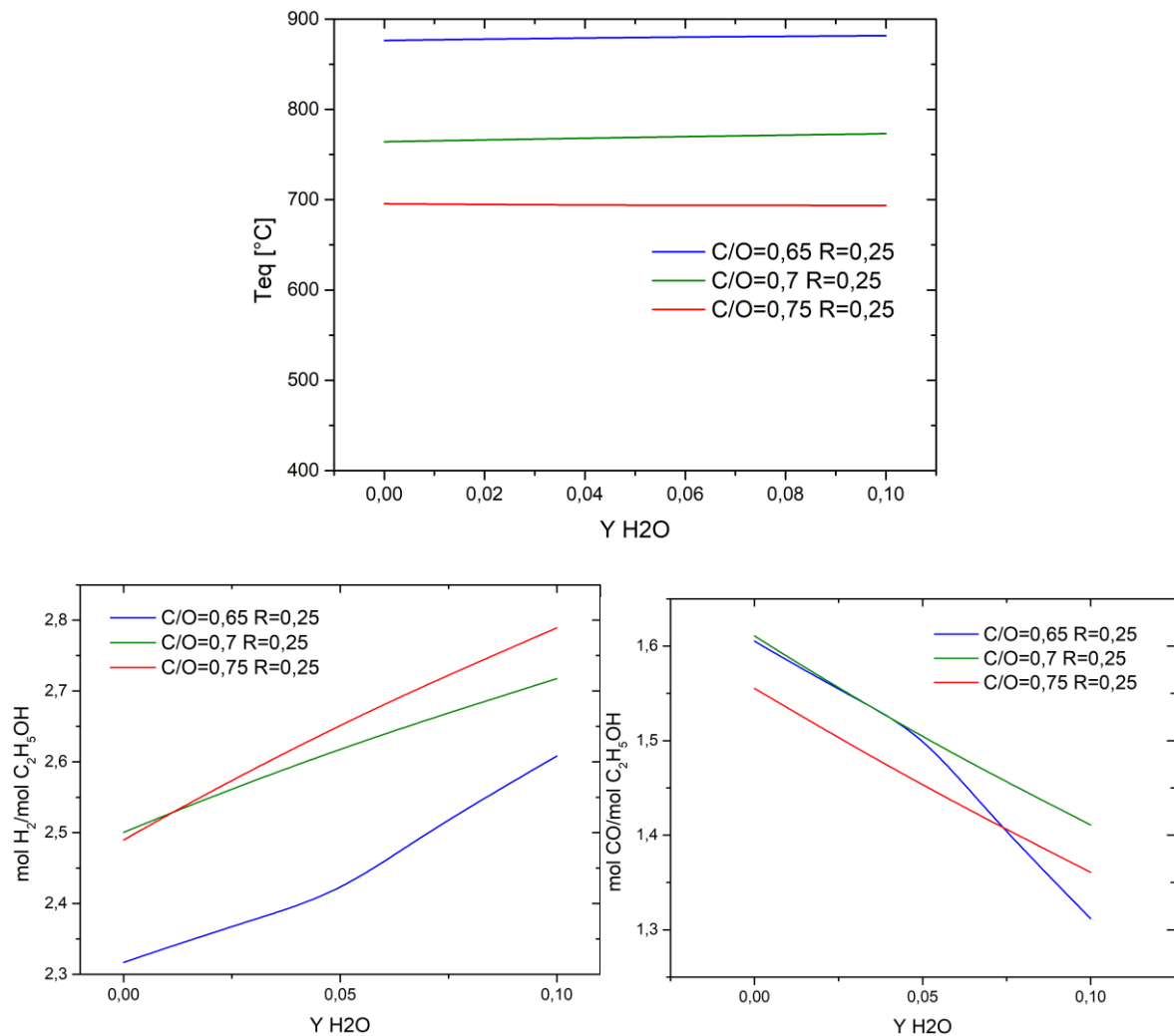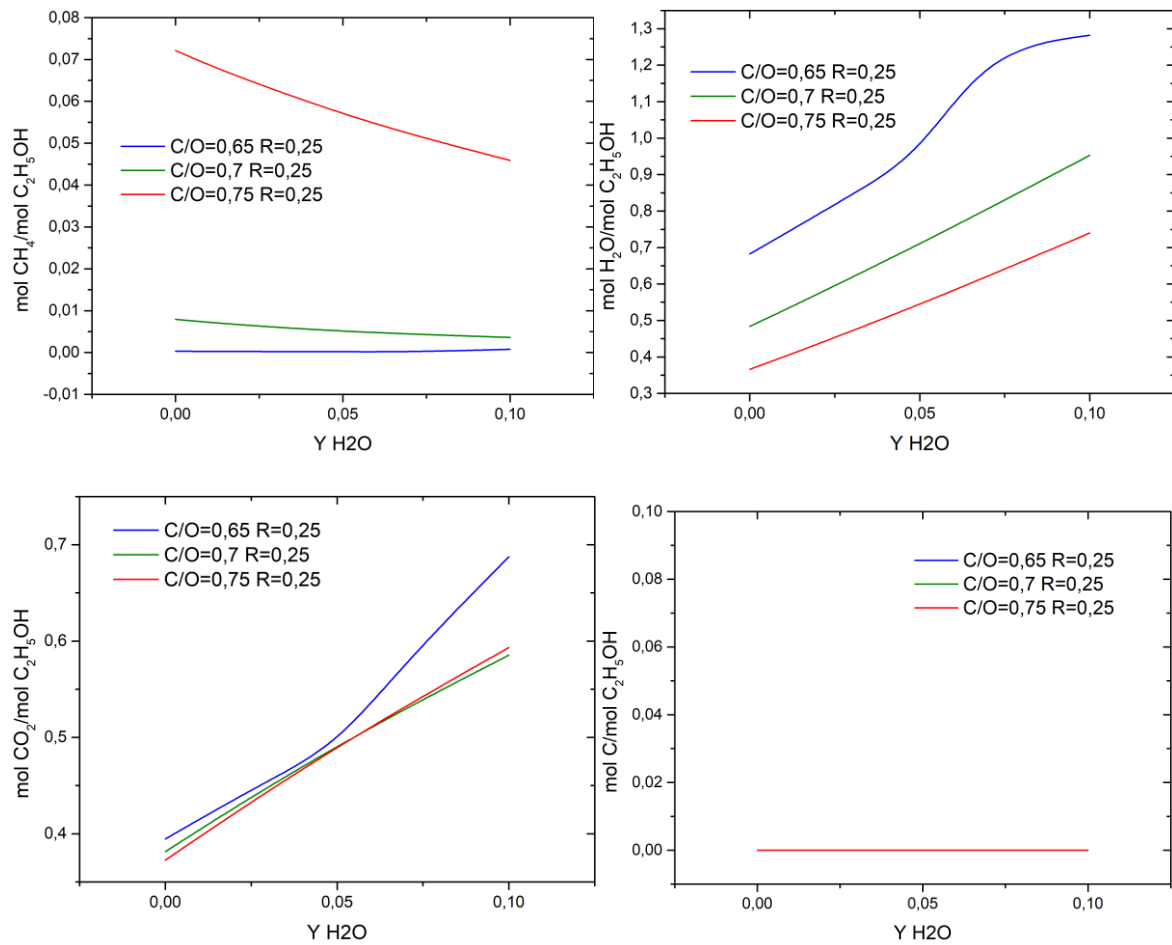
Figure 3.2 Thermodynamic analysis: Effect of H2O co feed on the equilibrium adiabatic temperature and species' molar fraction

Figure 3.2 is showing the effect of water co-feeding, on three C/O ratios (0.65, 0.7, 0.75) at constant R=0.25. No significant effect of water co-feeding is observed on the equilibrium temperatures under the assumption that H_2O is replacing the diluting N_2 as a dilutant. On the other hand, on increasing the y_{H2O} hydrogen and carbon dioxide equilibrium concentrations increase with a decrease in carbon monoxide equilibrium concentration likely related to an increased extent of water gas shift reaction.. The results of the study indicates that carbon formation is negligible for all water feed percentages for all the studied C/O ratios.

3.1.3 Effect of CO_2 co-feeding

Figure 3.3 compares the equilibrium results for 4 different concentration of CO_2 in the feed at constant R and y_{H2O} (respectively 0.25 and 0.05).

As the concentration of CO_2 increases, there is a decrease of T equilibrium and a lower peak of H2. The addition of CO_2 could limit the extent of the water gas shift reaction, leading to higher CO and H_2O equilibrium concentrations at fixed C/O ratio, as shown in the graphs.

Methane concentration is not particularly affected by the variation of CO_2 content although it moderately increases by adding carbon dioxide. The CH_4 concentration curve steeply increases at higher C/O ratio as a result of a lower equilibrium temperature which may promote less consumption of methane due to reforming reaction as previously explained.

Carbon deposition slightly increases with y_{CO2}, as well as with C/O ratio. In order to minimize coke formation, maximize the hydrogen production and prevent excessively high temperatures, C/O=0.7, with R=0.25 are selected for the tests.
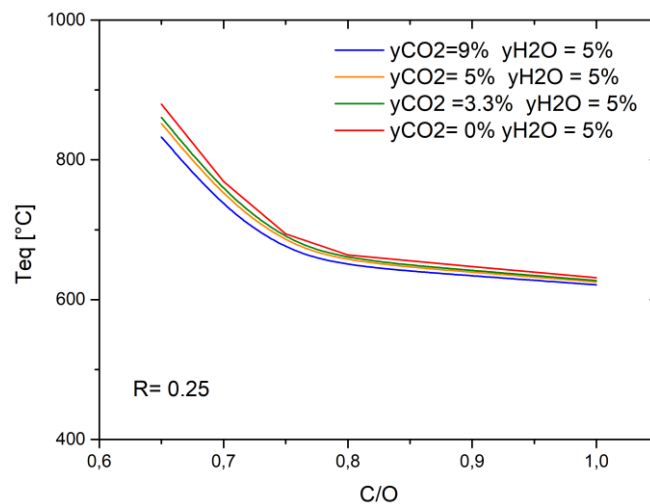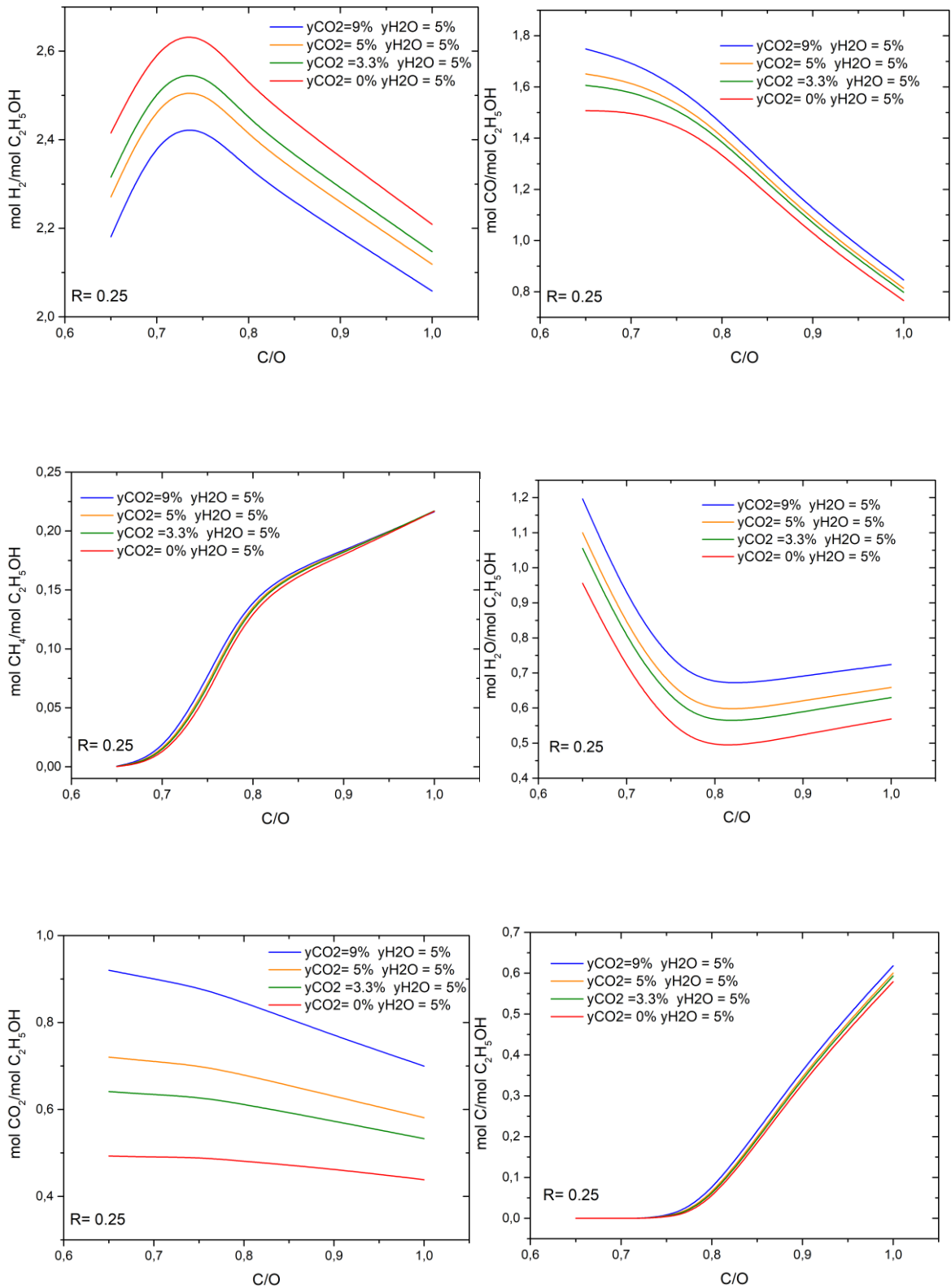
Figure 3.3 Thermodynamic analysis: Effect of CO2 co feed on the equilibrium adiabatic temperature and species' molar fraction

Reactor thermal efficiency

The extent of adiabaticity of the operation of the reactor is evaluated using the thermal efficiency α (equation 3.8)

Equation 3.8

$$\alpha = \frac{T_{exp}^{out} - T_{exp}^{in}}{T_{adiabatic}^{out} - T_{exp}^{in}}$$

In Equation 3.8, T_{exp}^{in} is the temperature measured by a thermocouple located at the inlet of the reactor, T_{exp}^{out} is the temperature measured by a thermocouple at the outlet of the catalytic channel and $T_{adiabatic}^{out}$ is the adiabatic temperature calculated with the inlet composition, inlet temperature, and the outlet composition. Using Equation 3.9, the specific enthalpy for every component is calculated. Then, the total enthalpy is calculated using Equation 3.10 as the sum of the product between the specific enthalpy and the molar flow rate of each specie in the mixture. The used coefficients of the heat capacity and enthalpy of formulation for each specie were presented by Bride [47].

Equation 3.9

$$H_i(T) = \Delta H°_{F,i}(T_{ref}) + \int_{T_{ref}}^{T} \tilde{C}_{Pi}.dT$$

Equation 3.10

$$\dot{H}(T) = \sum_{i}^{NC} n_i.H_i(T)$$

Assuming the adiabatic condition, enthalpy balance is performed and the $T_{adiabatic}^{out}$ is calculated to satisfy the Equation 3.11.

Equation 3.11

$$\dot{H}_{in}(T_{exp}^{in}) = \dot{H}_{out}(T_{adiabatic}^{out})$$

3.1.4 Previous results

During the previous experimental campaigns [33], C/O=0.75 with varying R ratio (1,0.5, and 0.25) were selected for a study to evaluate the effect of dilution on the process, as reported in figure 3.4 Another study regarding the water co-feed effect [33] was performed on NE5 catalyst with C/O=0.65 and R=0.5 at different water concentrations, as presented in figure 3.5.

In figure 3.4 the solid phase temperature measured by the pyrometer as explained previously in chapter 2 is indicated by the dotted lines, while the gas phase temperature, measured with the thermocouple are represented by in solid line. The vertical lines indicates the beginning of the monoliths, the end of the coated part and the end of the monoliths. Comparing the effect of the R ratio there is an increase of the profile temperatures as R decreases, perfectly in line with the thermodynamic analysis. The concentration profile for NE3 catalyst were not collected because it deactivated due to coke formation.

NE2 - y C_2H_5OH = 10% , C/O=0.75, R=1,   F=10Nl/min, T_{in}=85°C
NE2 - y C_2H_5OH = 13.4%, C/O=0.75, R=0.5, F=10Nl/min, T_{in}=85°C
NE3 - y C_2H_5OH = 16.2%, C/O=0.75, R=0.25, F=10Nl/min, T_{in}=100°C
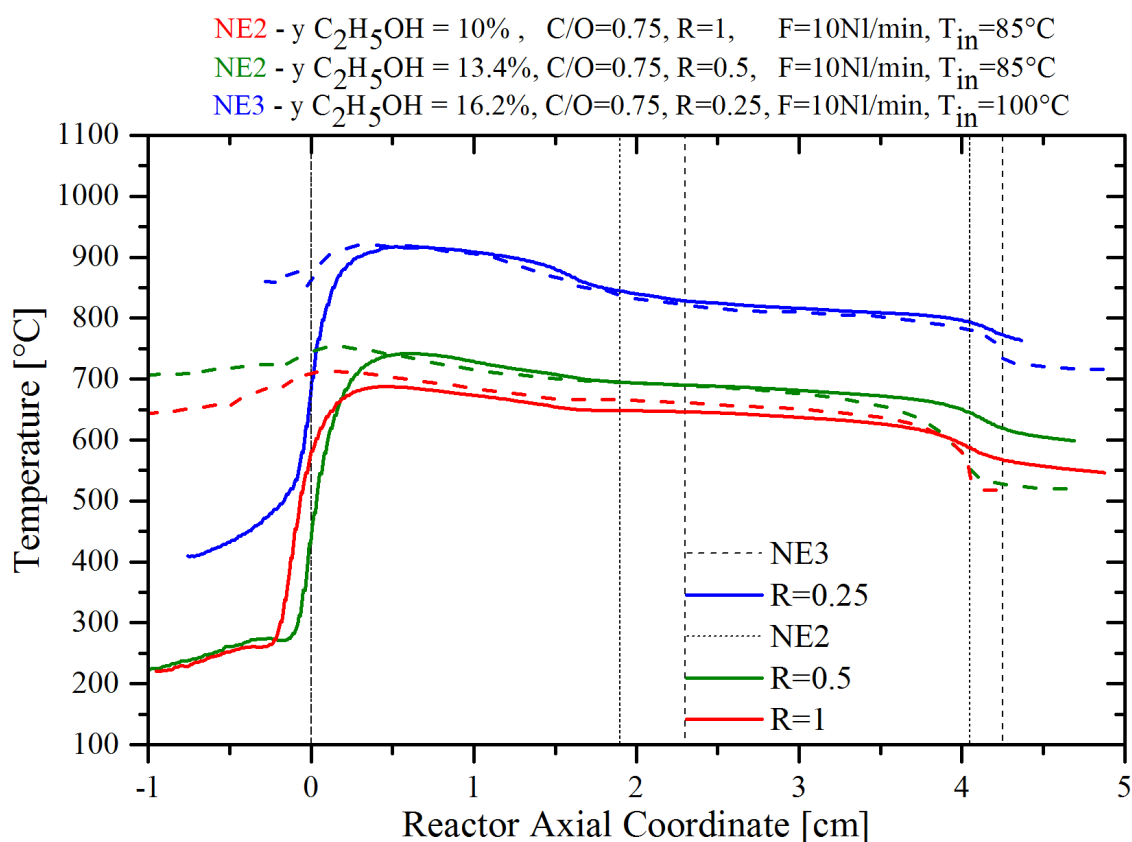
Figure 3.4 effect of R on gas and solid phase temperature profiles

In figure 3.5 the effect of H_2O concentration was evaluated

NE6 and NE5 - y C_2H_5OH = 11.2%, C/O=0.65, R=0.5, F=10Nl/min, T_{in}=100°C
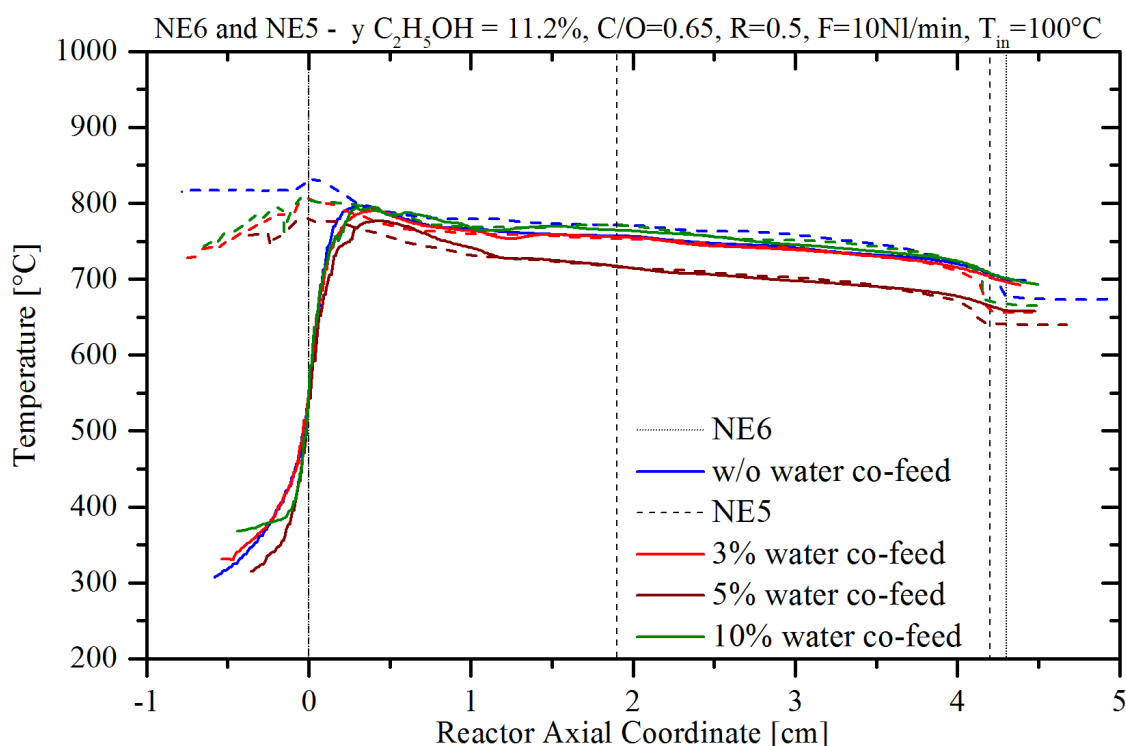
Figure 3.5 effect of water co-feed on gas and solid phase temperature profiles

The temperature profiles obtained for dry ethanol CPO was in line with previous findings in the literature [48] . Here, the co-feed of H2O did not seem to affect significantly the thermal behavior. The intensity and the position of the hotspot was similar as in the H2O-free system.

The axial concentration profiles of the reactants and the main products that were measured in the dedicated experiments are plotted in Fig. 3.6 in terms of molar fraction of all the detected gas-phase species. In ethanol CPO oxygen was consumed within the same characteristic length of about 5 mm from the entrance, as seen in previous studies [32] [33] with different fuels which confirms that oxidation reactions proceed under full mass transfer control and are thus insensitive to the nature of the fuel and verifies that the measurement technique has minor impact on the results.

On the other hand, a significant drop of the concentration of the cracking species (CH_4, CH_3CHO, C_2H_4) was observed in the initial part of the reactor on increasing the amount of

feed water. A significantly lower CO concentration was observed for 10% of water concentration in the feed experiment, which is associated an increased extent of the water gas shift reaction, resulting also in higher concentration of CO_2. Noteworthy an almost complete ethanol conversion was recorded for all the three experiments.
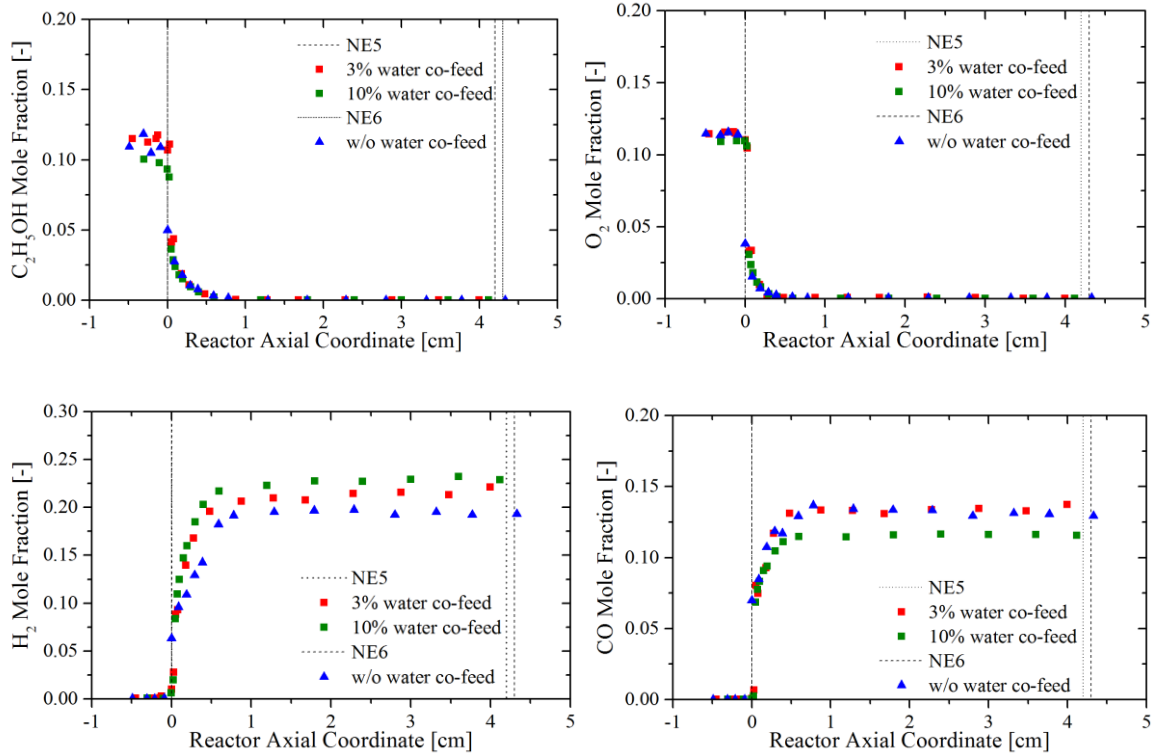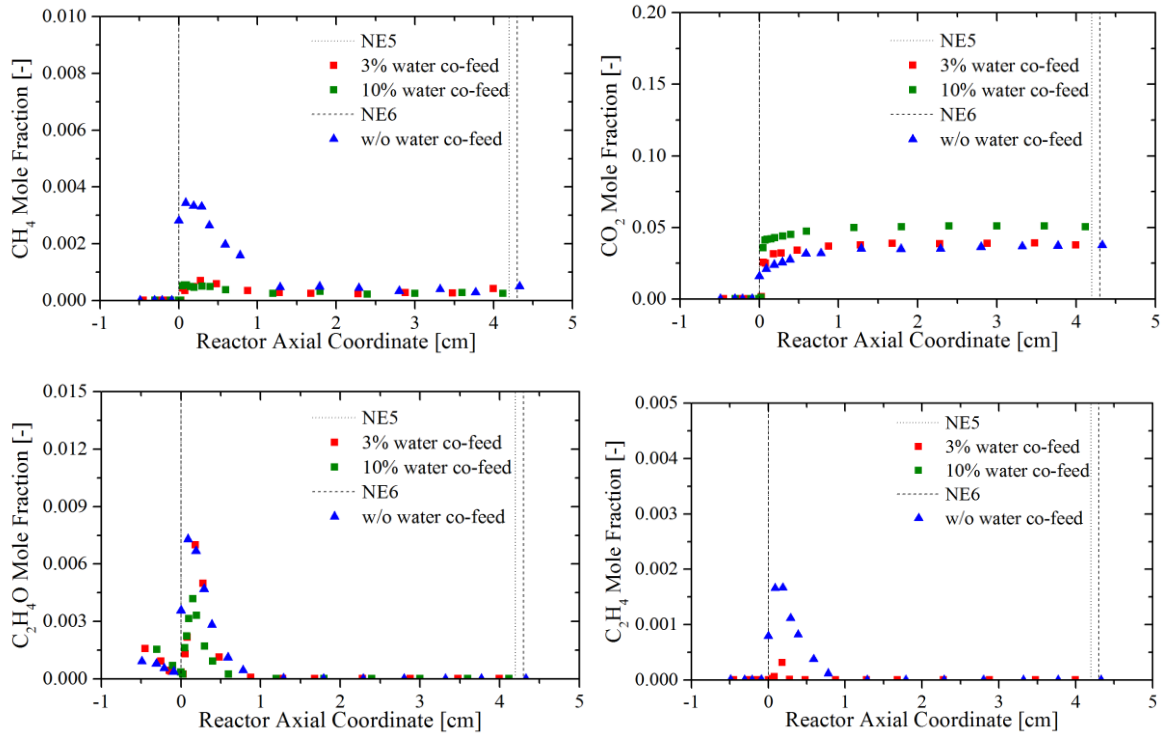
Figure 3.6 effect of water co-feed on gas and solid phase temperature profiles

3.2 Effect of CO₂ cofeed

3.2.1 Operating conditions

The catalyst (NE4) is used to perform some test to evaluate the effect of CO_2 ratio at fixed C/O and R ratios. According to the thermodynamic analysis, C/O=0.7 guarantees a lower risk of carbon formation which rapidly increases approaching higher C/O ratios. R=0.25 is chosen since this dilution condition is related to a high H_2 production at a moderate equilibrium temperature which prevents thermal deactivation of the catalyst by sintering. Concerning the amount of co-feed water, y_{H2O}=5% is selected and will be fixed during all experiments performed in this study.

Initially H_2O/CO_2=1.5 (y_{CO2}=3.3%) was taken into account, since it represents the ratio for recycling of the flue gases produced from the total oxidation of ethanol. However, due to experimental limitation this ratio was not achieved and the experimental study is performed at a higher CO_2 concentration with H_2O/CO_2 equals 0.56 (y_{CO2}=9%).

The selected working conditions for the experimental campaign performed on NE4 catalyst to evaluate the effect of CO_2 co-feeding, are the following:

1)C/O=0.7 R=0.25 y_{H2O}=5% y_{CO2}=0%

2)C/O=0.7 R=0.25 y_{H2O}=5% y_{CO2}=9%

Catalysts used in this study

In this experimental campaign, Rh-coated honeycomb catalyst is adopted (NE4). Cordierite honeycomb monolith with 400 cpsi cell density is used where α-Al_2O_3 washcoat is added to support the active phase as explained in Chapter 2.2 of this thesis. The catalytic monolith has the following properties in Table 3.1. The reactor is arranged in a same way described in Chapter 2.1.2.

Table 3.1 NE4 catalyst properties

Monolith	Catalyst	L_{cat} [cm]	L_{BHS} [cm]	m_{cat} [g]	m_{cat}/L_{cat} [g/cm]
NE4	Rh/α-Al_2O_3	4.2	2.46	1.74	0.616

3.3 Results and discussions

Following the same spatial sampling technique already employed throughout the previous experimental activities [33] both the concentration and the temperature profiles are collected. For this experimental test, first a water-ethanol temperature and concentration tests are performed with C/O = 0.7, R = 0.25 y_{EtOH} = 14.75%, y_{H2O} =5%, y_{CO2} =0%. R ratio are adjusted by adding extra nitrogen flow as a dilutant of the process. The results of this test are compared with CO2 co-feeding temperature and concentration tests profiles performed with C/O = 0.7, R = 0.25 y_{EtOH} = 14.75%, y_{H2O} =5%, y_{CO2} =9% (H_2O/CO_2=0.56). The R ratio is kept constant by replacing the diluting nitrogen with CO_2.

It is worth mentioning that a series of characterization methane temperature tests are performed after each CPO ethanol test, either temperature or concentration to track the state of the catalyst deactivation. As the catalyst testing is completed temperature programmed oxidation, TPO, is performed on the spent monolith to characterize its deactivation mechanism.

Temperature and concentration profiles
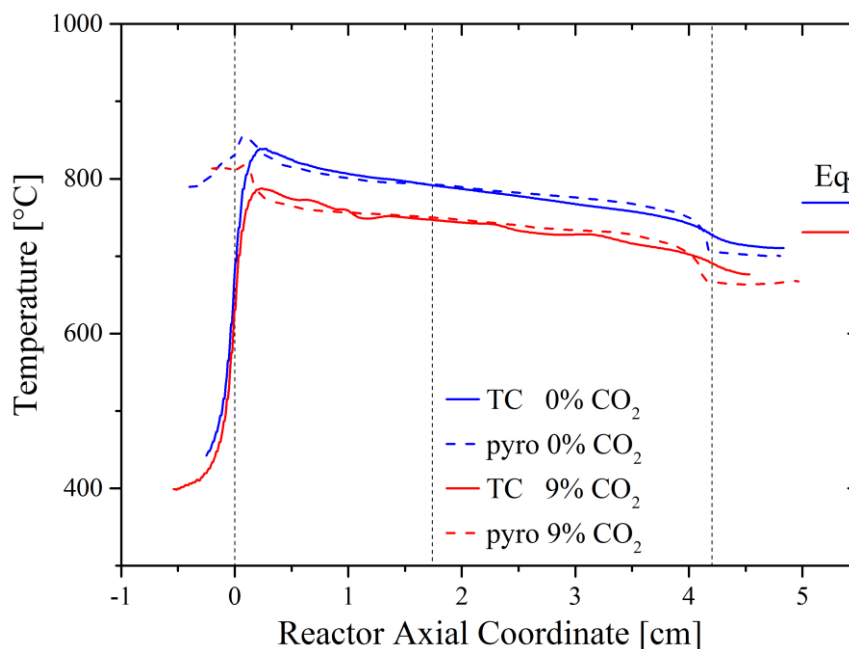
Figure 3.7 Temperature profiles comparison between water-ethanol and water-ethanol+ CO2 mixture

In figure 3.7, the solid phase temperature measured by the pyrometer as explained previously is indicated by the dotted lines, while the gas phase temperature, measured with the thermocouple are represented by in solid line. The vertical lines indicates the beginning of the monolith (x=0), the end of the coated part (x=1.7cm) and the end of the monolith (x=4.2cm). The horizontal lines at the right side of the panel represent the adiabatic equilibrium temperature, calculated as previously explained.

As presented in Figure 3.7, the obtained temperature profiles are in line with the previously performed studies for ethanol CPO. The catalyst exhibits a rapid increase of the gas phase and the solid phase temperatures at the inlet of the monolith associated with the rapid exothermic oxidation reactions taking place in the region where oxygen is still present. As soon as the oxygen is completely depleted a drop of the temperature is observed associated with the reforming reactions. The super imposition of the exothermic and the endothermic reactions leads to the formation of a hot spot at the entrance of the monolith. By looking at the impact of the CO_2 addition, a limited effect on the qualitative thermal behaviour of the

reactor is observed. Replacing part of the diluting nitrogen with CO_2 shifted the adiabatic equilibrium temperature to a lower value moving the whole profile to lower temperatures. It is worth mentioning that the calculated thermal efficiency α for water-ethanol mixture CPO and water-ethanol mixture CPO with CO_2 cofeed are 1.09 and 1.05 respectively.

By looking at the concentrations profiles presented in Figure 3.8, although there is a cooling effect, kinetics are still very rapid as inferred from the large concentration gradients for most of the species occurring at the entrance of the reactor (x=0). The concentration profiles show a lower selectivity towards hydrogen production downstream the reactor. The concentration profile of ethylene and acetaldehyde are not significantly affected with CO_2 addition. On the other hand, higher concentration of CH_4 in the oxy-reforming zone are observed, which may be related to the different temperature in this area. Reverse water gas shift or ethanol dry reforming at the entrance of the reactor might be favoured, leading to the observed consumption of CO_2 and the increased production of CO and H_2O. Other experimental activities at different CO_2 concentration are needed to provide a better understanding of this behaviour.

As previously observed in previous studies [33] the measured molar fractions downstream the reactor is slightly different than the values measured at the end of the monolith channel which can be explained by the cup mixing effect where the outer most channels are colder due to some residual heat losses by the system leading to lower conversions.
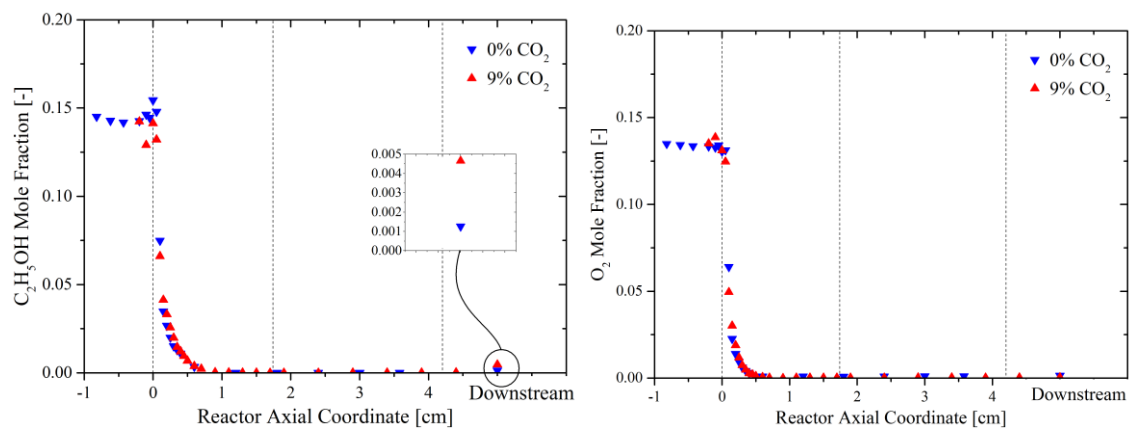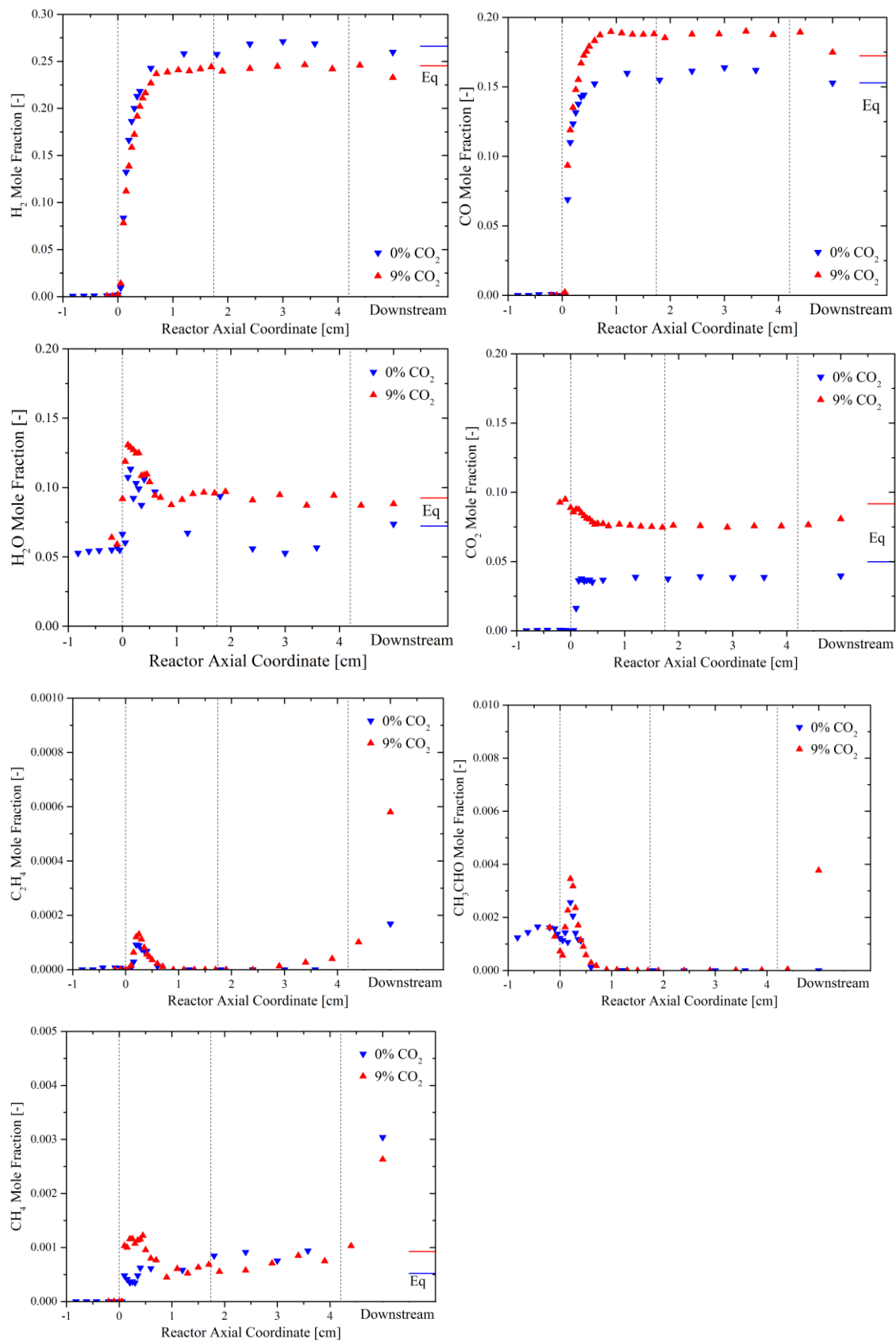
Figure 3.8 Concentration profiles comparison between water-ethanol and water-ethanol+ CO2 mixture

The deactivation state of NE4 catalyst is monitored by performing a methane characterisation test after every ethanol test and evaluating the hot spot temperature. Figures 3.9 and 3.10 show the evolution of the solid and the gas phases temperature profiles by deactivation.
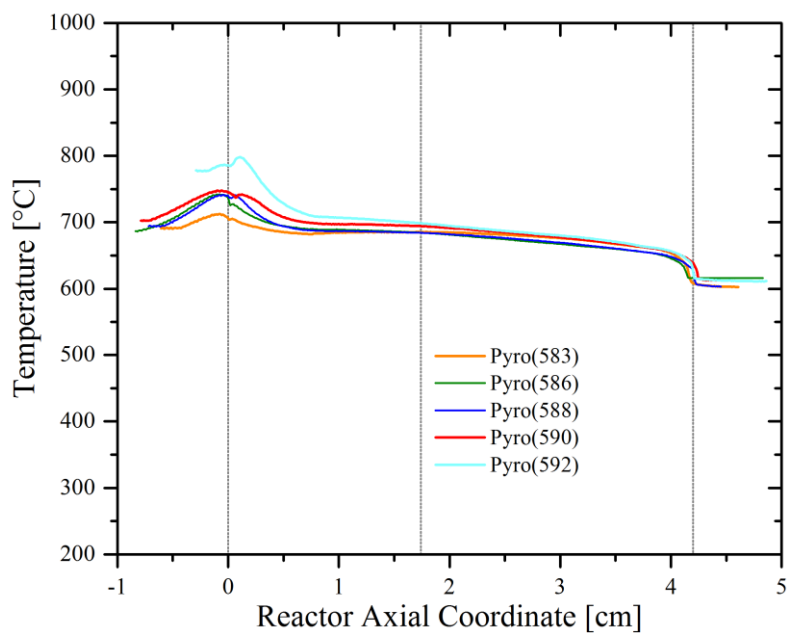
Figure 3.9 Evolution of the solid phase temperature after each ethanol test
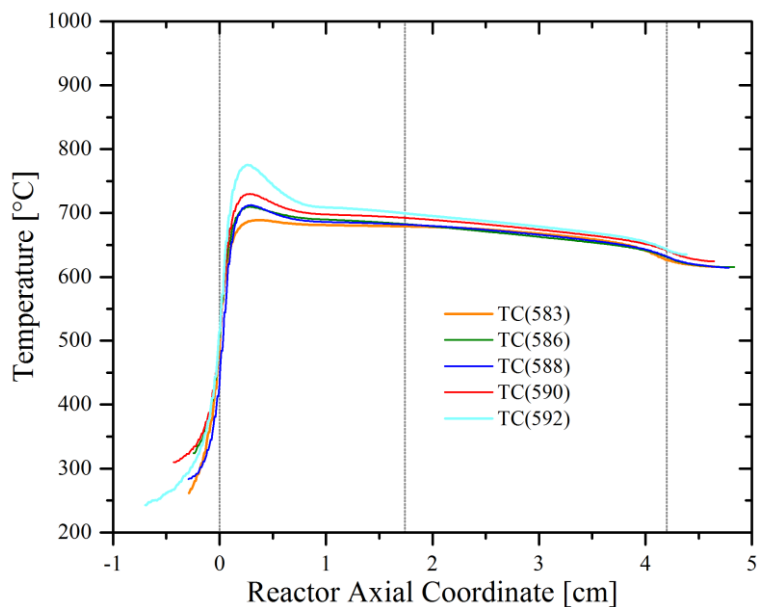
Figure 3.10 Evolution of the gas phase temperature after each ethanol test

As recalled above, the hot spot is formed as a result of the superposition of the exothermic oxidation and endothermic steam reforming process. The catalyst deactivation has no effect on the released heat flux, since the rate of O_2 consumption reactions is extremely high and entirely governed by mass transfer; instead, catalyst deactivation limits the reaction rate of CH_4 steam reforming, thus the heat consumption term, being it under partial chemical kinetic control. As seen in these figures the peak temperature is increasing. However, the axial position of the peak temperature and the shape of the peak are not changing indicated some loss of activity of the catalyst after being onstream in the ethanol CPO. The experiment guide for standard methane tests are given in Table 4.3 to explain and clarify the experimental path followed for NE4 catalyst.

Table 3.2 Experimental guide of methane standard tests performed on NE4 catalyst

Methane Standard Tests Performed on NE4 catalyst	
Run #	**Experiment Guide**
583	First methane benchmark test
586	Performed after the first ethanol temperature profile (C/O=0.7, R=0.25, yH2O=5%)
588	Performed after the first ethanol concentration profile (C/O=0.7, R=0.25, yH2O=5%)
590	Performed after the second ethanol temperature profile (C/O=0.7, R=0.25, yH2O=5%, yCO2=9%)
592	Performed after the second ethanol concentration profile (C/O=0.7, R=0.25, yH2O=5%, yCO2=9%)

3.4 Post-mortem analysis

After completing the required experiments NE4 catalyst was unloaded from reactor in order to perform post-mortem analysis. In Figure 3.11, small amount of coke deposit is found downstream the reactor.

Figure 3.11 Reactor display after deactivation of NE4 catalysts

3.4.1 Temperature programmed oxidation (TPO)

The catalytic monolith (NE4) is unloaded from the reactor and is cut axially into two halves. Then a sample from the central part of one-half of the monolith is cut, crushed, and loaded in the quartz reactor to perform TPO. The sample, as shown in figure 3.12, is located in the middle of the coated area with a specific length of 0.78cm and a mass of 123.2 mg. Another sample is taken from the deposit that was found downstream the reactor with a mass of 21.4 mg. The results of the TPO of the central sample shown in figure 3.12 are compared with the results obtained from previous experimental work concerning NE5 monolith which was tested previously with water co-feeding at C/O=0.65 R=0.5 and y_{H2O}=5%. On the other hand, the sample of carbon deposit is compared with the results obtained from a similar sample taken from the deposit found downstream NE3 monolith tested with ethanol only at higher C/O =0.75 and R=0.25, Figure 3.12. The masses of the tested samples are reported in Table 3.3.
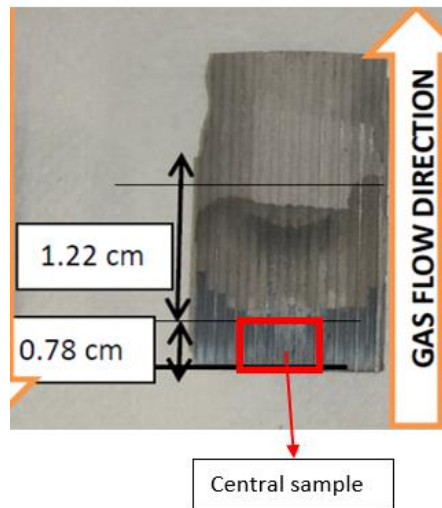
Figure 3.12 NE4 cross section with highlighted sample for TPO

Table 3.3 Mass of the samples for TPO

Monolith [mg]	Mass of the sample	
	0-7mm	C-deposit
NE3	-	22.8 mg
NE4	123.2mg	21.4 mg
NE5	108.2mg	-

Figure 3.13 presents the comparison of the results obtained from the TPO of the central sample (0-7mm) of monoliths NE4, tested in this experimental campaign with water-ethanol mixture and CO_2 cofeed, and NE5 which was tested in the previous experiments with ethanol and different water molar concentrations in the feed.

On a qualitative basis, it is interesting to note the two different peaks appearing at 300°C and 500°C for NE4 catalyst tested with water-ethanol mixture and CO_2 cofeed. The 300°C peak is associated to relatively uniform C-species located near the Rh particles. However, the 500°C peak is representative of either a more stable C-species or likely stored on the support and thus interacting less with the metal. The amount of the carbon deposit on catalyst NE4 may be justified by an increased extent of the boudouard reaction due to the high molar

fraction of CO. On the other hand the first section of NE5 catalyst shows only one significant peak at temperature around 500°C. This indicates the absence of the less stable carbon species, which may be related to the water co-feeding for all the testes performed on this catalyst. Steam co-feeding helped gasifying the carbon formed on the catalyst surface. It is worth mentioning that the results from TPO are not representative from a quantitative point of view since the two monoliths were tested with different working conditions (R and C/O).
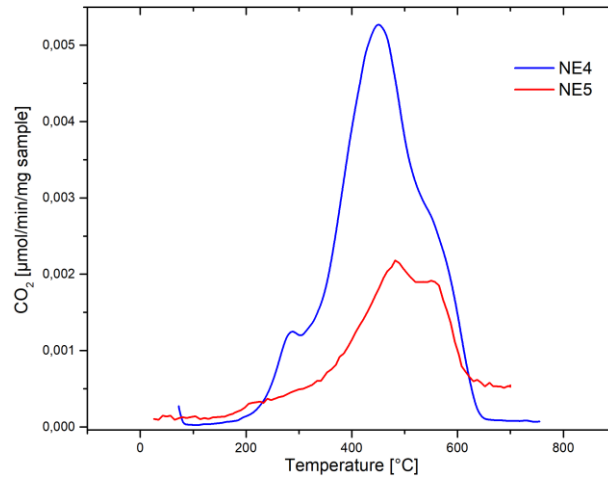
Figure 3.13 TPO analysis for central sample (0-7mm) of catalyst NE4 and NE5

Moreover, figure 3.14 shows the results of the TPO performed on deposits collected downstream of the NE3 and NE4 catalyst respectively. NE3 was tested in the previous experimental campaigns without water co-feed at C/O=0.75 R=0.25, thus in a more severe carbon condition than NE4. The results shows that both samples are of similar complexity, however the sample collected downstream NE3 has a higher peak.
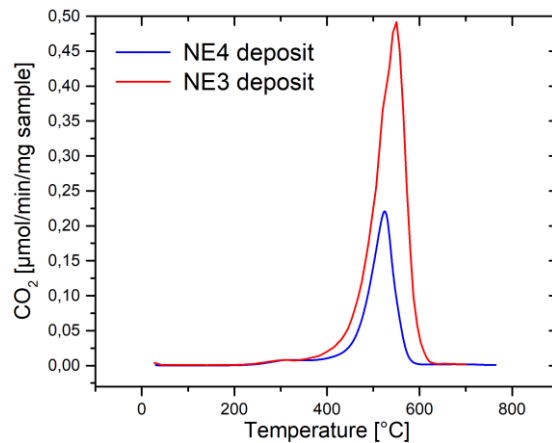
Figure 3.14 TPO analysis for the carbon deposit found at the downstream of the reactor

3.5 Methane CPO: front heat shield configuration effect

In order to test the effect of a FHS configuration of the catalyst on ethanol CPO, where the modelling results have shown a better match with the measured profiles for methane and propane CPO [41] a new batch of catalyst was prepared. Following the standard procedure, CPO of methane is performed on a catalyst (OTT2) through temperature and concentration tests in order to set the benchmark of the monolith. The experimental campaign is conducted by placing the catalyst in a continuous FHS configuration, such that a perfect continuum between the catalyst and the heat front shield is realized. The design of the reactor is reported in figure 3.15
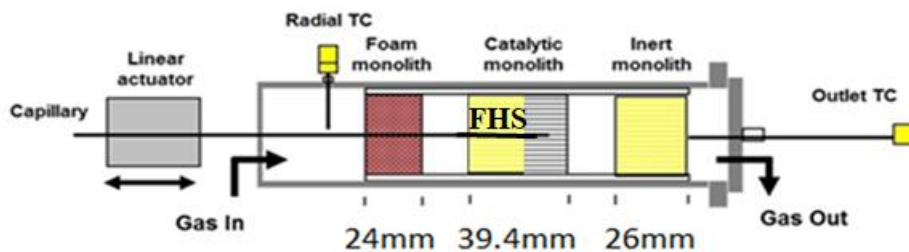
Figure 3.15 Reactor design with catalyst OTT2 arranged in continuous FHS configuration

Monolith data

The selected catalyst OTT2 was prepared according to the procedure described in chapter 2 and its properties are reported in Table 3.4

Table 3.4 OTT2 monolith properties

Name	Support	CPSI	Ltot [cm]	L_FHS [cm]	L cat. [cm]	D [cm]	m_{cat} [gm]	mcat/Lcat [gm/cm]	Type
OTT2	Cordierite	400	3.94	2.04	1.9	2.5	1.13	0.595	Rh/α-Al2O3

Working condition

The operating working conditions tested is $y_{CH4} = 27.4\%$ and O2/C = 0.56.

Experimental activity

Methane temperature and concentration tests are performed through the spatially resolved sampling technique, as explained previously.

As observed from the obtained temperature profiles, Figure 3.16, the presence of the continuous FHS better insulated the inner reactor portion and favours an increase of the local surface and gas-phase temperature in line with the previously obtained results [41]. The monolith with continuous FHS exhibits a much sharper hotspot than the one reached with a BHS arrangement, with a maximum temperature of 980 °C measured by the thermocouple and 960 °C measured by the pyrometer. Thermal equilibrium is not reached in this test, which may indicate that the length of the coated part is shorter than the required one.
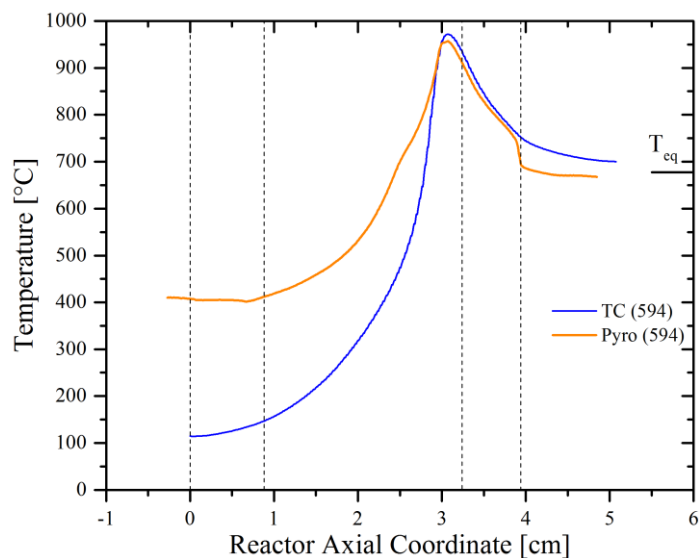
Figure 3.16 Solid and gas phase temperature profiles for OTT2 catalyst

Concerning the measured concentration profiles of reactants, reported in figure 3.17, it is found that O_2 conversion- which is regulated, as previously explain, by the mass transfer- is complete within 5 mm from the catalyst entrance. On the other hand, methane is consumed at a slower rate, where methane is under partial chemical kinetic control as previously explained [34]. The measured molar fraction of methane at the end of the monolith channel is lower than calculated the adiabatic equilibrium value (represented by a red line at the end of the reactor axial coordinate axis), which can be explained by the higher temperature measured at this section of the monolith.

The measurement of the product composition shows that there is a reduced selectivity towards hydrogen and CO. Water and CO_2 increases as the oxidation zone is approached, with a rapid drop for the CO_2 occurring at the beginning of the reforming zone which can be explained by the water gas shift. Downstream the monolith cup mixing effect explains the change of the compositions as observed for previous experiments.
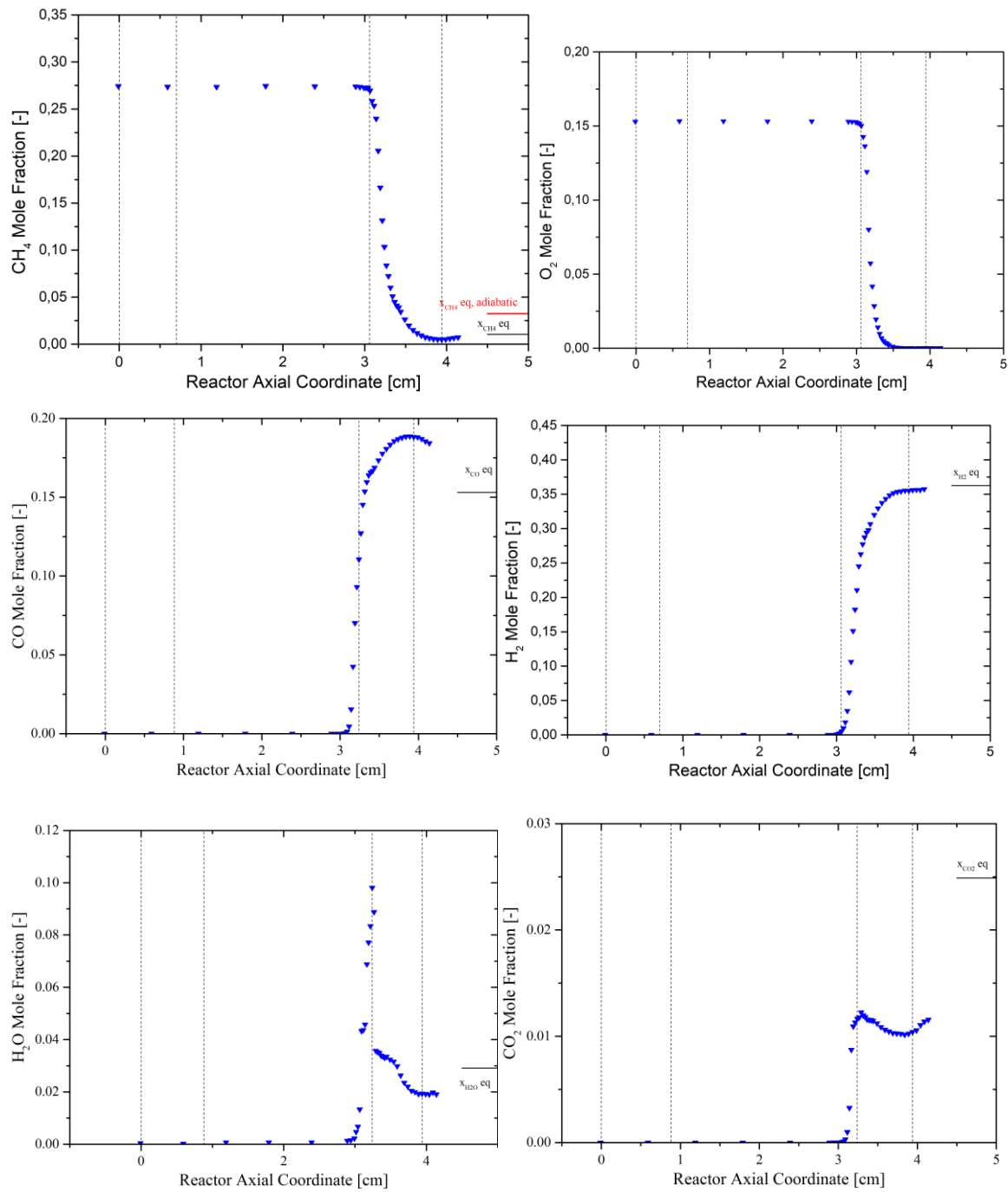
Figure 3.17 Concentration profiles CPO of methane with catalyst OTT2 tested in FHS configuration

The concentration test shows that the process did not reach equilibrium: in order to better understand the probable cause of this trend, the catalyst was cut along its central axis. Particular evidence to a shorter coated length than the one visible from outside the monolith is observed. The coated part, a wetted part as well as the direction of the gas flow are reported in figure 3.18 and 3.19. The catalysts used in a previous experimental campaign and belonging to the same batch (NE4, NE5, NE6) are also compared. Figures 3.18 and 3.19 show that the length of the coated part inside is different from the external one: this suggests the presence of a problem in the coating process where the high viscosity of the slurry leads to poor distribution of the coating inside the channels.
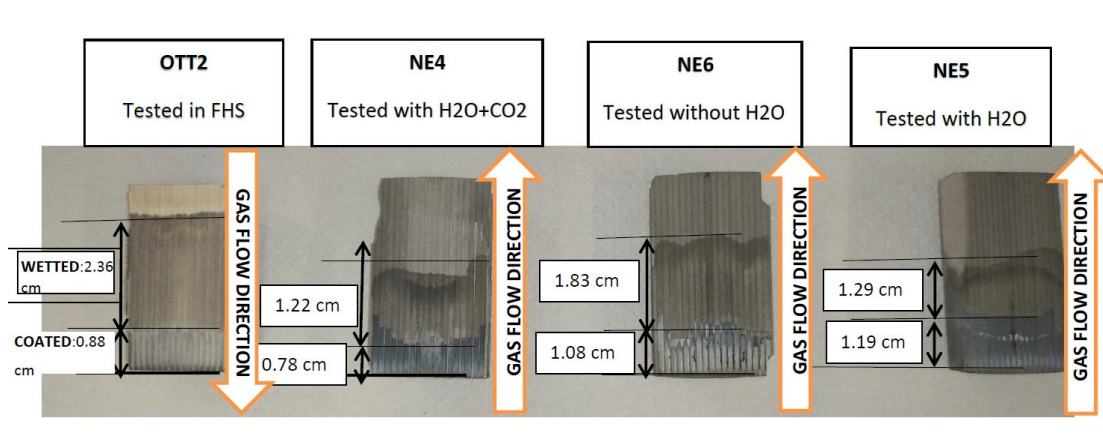
Figure 3.18 inside view of the cross-section of catalysts NE4, NE5, NE6, OTT2
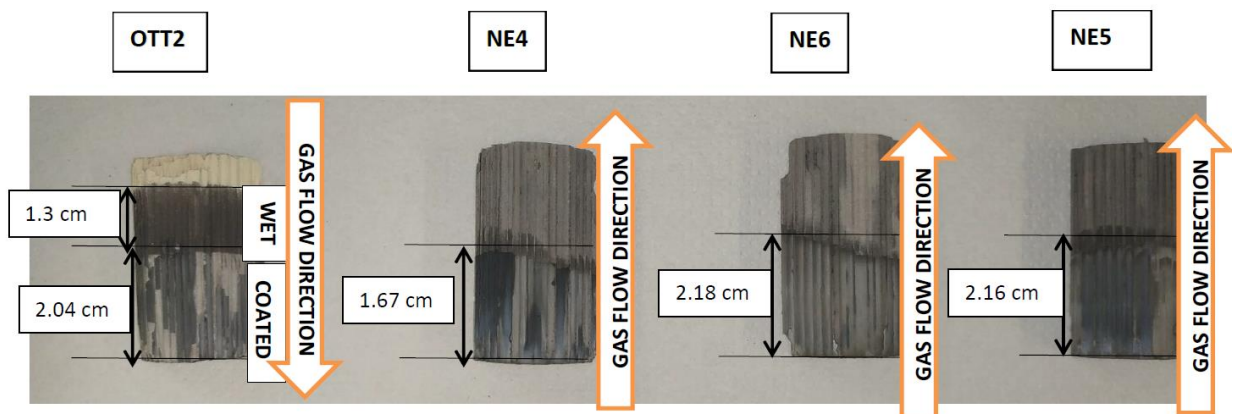
Figure 3.19 outside view of the cross-section of catalysts NE4, NE5, NE6, OTT2

Chapter 4: Tail gas recycling in a SOFC auxiliary power unit

4.1 Introduction

Recently, fuel cells became more interesting for small-scale and onboard applications as they provide improved performances from energetic and environmental point of view. For example, more efficient energy use can be achieved by installing a Combined Heat and Power (CHP) system in residential areas, where the heat produced by power generation is used to cover the hot water demand. Regarding onboard applications, a good example is the fuel cell based Auxiliary Power Unit (APU) for heavy-duty trucks, which is expected to bring significant advantages by reducing engines idling costs, the emissions of trucks, and the noise of idling engines. [40]

As a commercial application of the CPO of liquid fuels the performance of a typical SOFC APU was evaluated based on energy efficiency providing a true measure of the process performance. The analysis focuses on the fuel reformer, evaluating the effect of working conditions (C/O ratio and recycling of the SOFC exhaust) on the process efficiency for ethanol as a fuel. The effect of the current density and fuel utilization of the SOFC were also evaluated. The model was implemented on Matlab® 2019 software and 1KWe net was selected as basis of the study.

4.2 Working system

Figure 4.1 represents the flow diagram of the analysed working system. The main components are : air and flue gas recycling compressors, a pump, an evaporator, two adiabatic mixers, an adiabatic reformer, a solid-oxide fuel cell stack, an off-gas burner and three heat exchangers that are used in order to supply heat or cool down the inlet and outlet streams of the SOFC air channel and the inlet of the fuel channel of the cell.
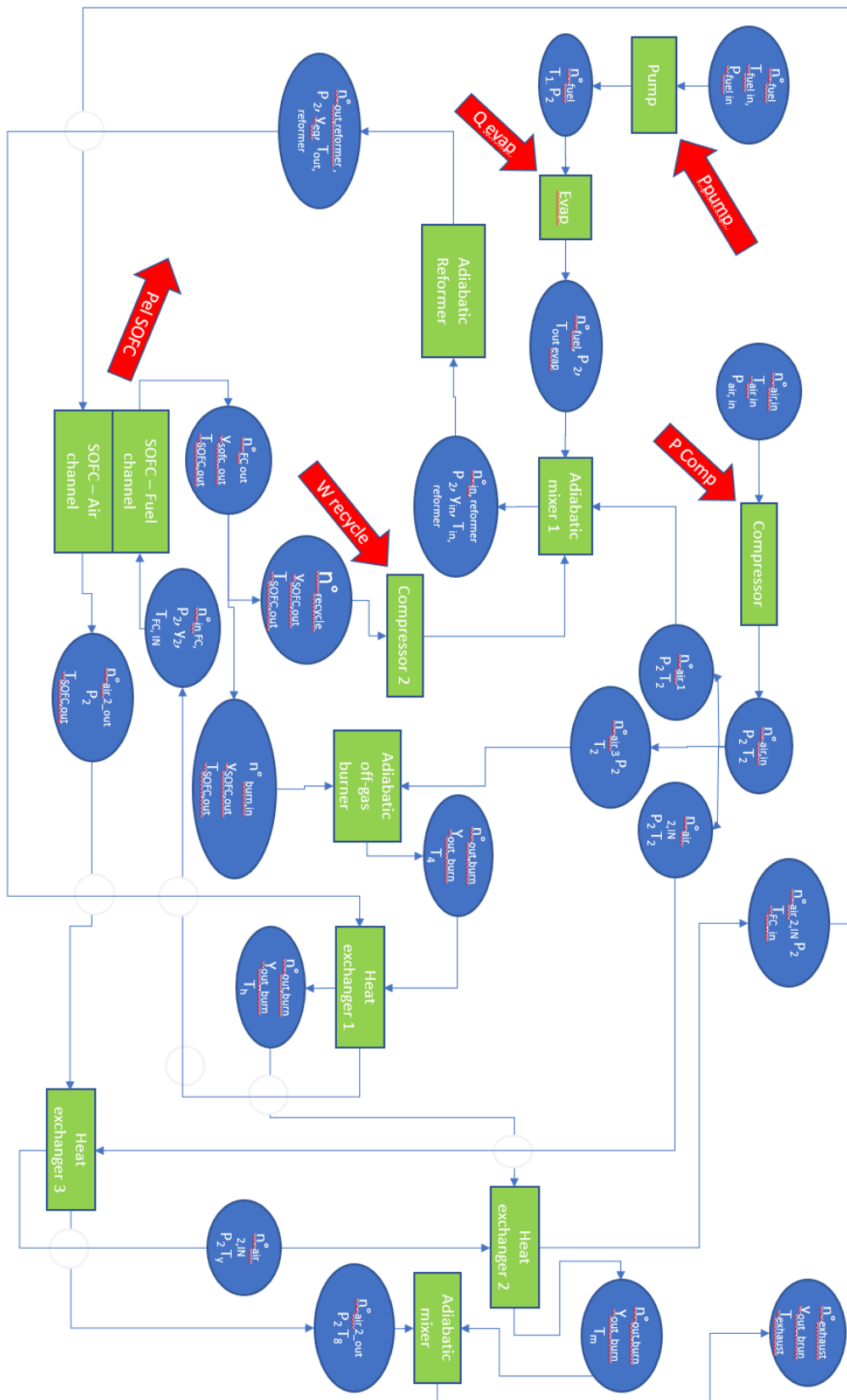
Figure 4.1 Flow diagram of the analysed SOFC-APU

4.2.1 Assumptions of the model

The working fluids were assumed ideal gas, considering the effect of temperature for the calculation of the specific heat (c_p) and selecting, where it was required, the average c_p between the inlet and outlet of each component. Pressure losses were not included, on the other hand the efficiency of the compressors and the pump were taken into account [49]. The heat exchangers were considered ideal with a unitary efficiency and a pinch point temperature of 50°C [49]

Fluid properties and the equations calculating the power output of the main components were retrieved from both a chemical and a thermodynamic engineering handbook, respectively [50] and [51]

The assumptions used for modelling solid-oxide fuel cell part were retrieved from a paper modelling the internal reforming of the cell [52] and are the followings:

- Feed consists of the following gas species, i = [C_2H_4O C_2H_4 C_2H_6 H_2O H_2 CO_2 CO C_2H_5OH CH_4 O_2 N_2 C]
- Air consists of 79% N_2 and 21% O_2
- Gas mixture at the fuel channel exit is at chemical equilibrium
- Fuel cell operates at steady state
- The temperature at the outlet of the fuel channel is $T_{FC,out}$= 850°C
- Temperature at the channel inlets is same for both air and the syngas entering the fuel channel
- $T_{FC,in}$ =$T_{FC,out}$-100°C
- Pressure drops along the fuel cell are neglected. Also, temperature at the channel exits is same
- Temperature of the solid structure is midway between the inlet and exit temperatures
- Fuel cell is insulated which means that there is no heat interaction with environment.
- Only hydrogen is electrochemically reacted. CO is converted to CO_2 and H_2 by water–gas shift reaction.
- Radiation transfer between solid structure and gas channels is ignored
- Contact resistances are ignored

Input	Value
TSOFC_out	850°C
Temperature difference between exit and inlet	100°C
Pressure of the cell (Pcell)	1 bar
Active surface area (A)	100 cm2
Exchange current density of anode (i0a)	0.65 A/cm2
Exchange current density of cathode (i0c)	0.25 A/cm2
Effective gaseous diffusivity through the anode (Daeff)	0.2 cm2/s
Effective gaseous diffusivity through the cathode (Dceff)	0.05 cm2/s
Thickness of the anode (La)	500 μm
Thickness of the electrolyte (Lc)	10 μm
Thickness of the anode (La)	50 μm

Table 4.1 Input data of the SOFC

4.2.2 Equations

1) The efficiency of the APU system is calculated as follows

$$\eta_{sys} = \frac{W_{el,net}}{N_{fuel,in} * LHV_{fuel,in}}$$

$$W_{consumed} = W_{pump} + W_{compressor,air} - Q_{evap} - W_{recycle} \ [W]$$

$$W_{el,net} = W_{el,SOFC,stack} - W_{consumed} \ \ [W]$$

Where Pel,net is our target equals to 1kWe; Nfuel,in is the inlet molar flow rate of ethanol, reported in mmol/s

2) The C/O ratio is calculated with this equation:

$$\frac{C}{O} = \frac{n_{C,fuel}}{2 * n_{O2} + n_{O,fuel}}$$

3) The inlet air molar flow rate $\dot{N}_{air\,in}$ which is the total air provided by the air compressor is divided into 3 different streams: $\dot{N}_{air,1}$, representing the air flow mixing with the recycled flue gas and the evaporated fuel and then sent to the adiabatic reformer; $\dot{N}_{air\,2,in}$ and $\dot{N}_{air\,2,out}$ respectively the inlet and outlet air flowing in the air channel of the fuel cell; $\dot{N}_{air,3}$ which is supplied in moderate excess (5%) to the off-gas burner for the combustion of the SOFC tail gas which is not recycled. The equations used for the calculations of these streams are the following:

$$\dot{N}_{air,1} = \frac{1}{2} * \dot{N}_{fuel} * \frac{\frac{n_{C,fuel}}{C} - n_{O,fuel}}{0.21} \quad \text{[mmol/s]}$$

$$\dot{N}_{air\,2,in} = \frac{\dot{Q}_{SOFC}}{cp_{air2} * (TFCout - TFCin)} \quad \text{[mmol/s]}$$

$$\dot{N}_{air\,2,out} = 0.21 * (1 - Uox) * Nair2, in \quad \text{[mmol/s]}$$

$$\dot{N}_{air\,in} = Nair1 + Nair2, in + Nair\,3 \quad \text{[mmol/s]}$$

$$U_{ox} = \frac{1}{2*0,21} * \frac{(\sum_{i=1}^{Nr\,species} N_{FC\,out,i} * n_{O,i} - \sum_{i=1}^{Nr\,species} N_{FC\,in\,,i} * n_{O,i})}{\dot{N}_{air\,2,in}}$$

where Uox is the air utilisation factor, nO,i is the number of oxygen contained in each species, nC and nO are the numbers of carbon and oxygen atoms of the inlet fuel (in this model, ethanol was selected as a fuel, thus nC=2 and nO=1).

4) The following equations were used to calculate the specific heat of each species and the total one. The a_i coefficients were taken from the Nasa memorandum document [47], R is the gas constant= 8.314 kJ/kmolK, y_i is the molar fraction.

$$cp_i(T) = R * (a_{1,i} + a_{2,i} * T + a_{3,i} * T^2 + a_{4,i} * T^3 + a_{5,i} * T^4) \quad \text{[kJ/kmolK]}$$

$$cp\,(T) = \sum_{i=1}^{Nspecies} y_i * cp_i(T) \quad \text{[kJ/kmolK]}$$

The enthalpies of each species and the total one were calculated with the following equations, where $T_0 = 298.15K$ is the reference temperature.

$$h_i(T_0) = R * \left(a_{1,i} * T_0 + \frac{a_{2,i}}{2} * T_0{}^2 + \frac{a_{3,i}}{3} * T_0{}^3 + \frac{a_{4,i}}{4} * T_0{}^4 + \frac{a_{5,i}}{5} * T_0{}^5 + a_{6,i}\right) \text{ [kJ/kmol]}$$

$$h(T) = \sum_{i=1}^{Nspecies}\left(h_i(T_0) + \int_{T0}^{T} cp_i(T)\ dT \right) \text{[kJ/kmol]}$$

Pump:

Assumptions: ideal fuel, $\eta_{poly,p}$=0.8; $\eta_{mecc,p}$=0.95; Pfuel,in=1 atm; P2=1.1*Pfuel,in ; T1= Tfuel,in= 298.15K; v*ΔP<< Nair,in*cpair*ΔTcompressor

$$\dot{W_{pump}} = \frac{1}{\eta_{poly,p} * \eta_{mecc,p} * density_{fuel,in'}} * \dot{N}_{fuel,in} * MW_{fuel,in} * (P_2 - P_{fuel,in}) \quad \text{[W]}$$

Compressors (Air and flue gas)

Air:

Assumptions: ideal gas, $\eta_{poly,c}$=0.85; $\eta_{mecc,c}$=0.95 ; Tair,in= 298.15K; β=(P2/Pair,in)=1.1; γ air,in=1.4

$$\theta_{air,in} = \frac{\gamma_{air,in} - 1}{\gamma_{air,in}}$$

$$T_2 = T_{air,in} * \beta^{\frac{\theta_{air,in}}{\eta \, poly,c}}$$

$$\dot{W}_{comp,air} = \frac{1}{\eta_{poly,c} * \eta_{mecc,c}} * \dot{N}_{air,in} * cp_{air,in} * (T_2 - T_{air,in}) \quad \text{[W]}$$

Flue gas recycling compressor

Assumptions: $\eta_{poly,c}$=0.85; $\eta_{mecc,c}$=0.95 ; β=1.1; ideal gas

$$\gamma_{flue\,gas} = \frac{c_{p,flue\,gas}}{c_{p,flue\,gas} - R}$$

$$\theta_{flue,gas} = \frac{\gamma_{flue\,gas} - 1}{\gamma_{flue\,gas}}$$

$$T_{recycle} = T_{SOFC,out} * \beta^{\frac{\theta_{flue\,gas}}{\eta_{poly,c}}}$$

$$\dot{W}_{recycle} = \frac{1}{\eta_{poly,c} * \eta_{mecc,c}} * \dot{N}_{air,in} * cp_{recycle} * (T_{recycle} - T_{SOFC,out}) \quad [W]$$

Evaporator

Assumptions: Tevap_out= Tevap+ 150K; 100% gas out of the evaporator =0.8; η_{evap} =0.8; no pressure drops

Q_evap=(1/ η_{evap})* n°fuel*(cp_fuel_L*(Tevap-T1)+DeltaHevap+ cp_fuel_V *(Tevap_out-Tevap)) [W]

Adiabatic reformer

The assumption of adiabatic conditions involved the simultaneous solution of the enthalpy balance and the determination of the Tout, reformer.

$$H_i(T) = \Delta H°_{F,i}(T_{ref}) + \int_{T_{ref}}^{T} \tilde{C}_{Pi}. dT$$

$$\dot{H}_{in}(T_{in,reformer}) = \dot{H}_{out}(T_{out,reformer})$$

This condition is combined with the minimization of the Gibbs Free Energy

$$dG = 0$$

Adiabatic mixers:

$$\sum_{i=1}^{Nflows,in} Nin, i * hin, i \ = \ \sum_{i=1}^{Nflows,out} Nout, i * hout, i$$

From this balances Tin reformer and Texhaust gas are calculated.

Off-gas burner

$$\sum_{i=1}^{Nflows,in} Nin, i * hin, i \ - \ \sum_{i=1}^{Nflows,out} Nout, i * hout, i + \text{Nburn*LHVburn=0}$$

From this equation the outlet temperature of the burner is calculated.

Heat exchangers

General equation for the calculation of the power exchanged by each heat exchanger:

$$Q_{HX,i} = N * cp * \Delta T \quad [W]$$

SOFC

All the parameters used in this sections are collected and explained above in table 4.1 and are retrieved, along with the equations of the SOFC part from Ibrahim's et al. paper [52].

1) Nernst Voltage is calculated as follows:

$$Vn = V_0 - \frac{R*T_{SOFC,out}}{2*F} * ln \left(\frac{y_{H2O,FC,out}}{y_{H2,FC,out}*\sqrt{y_{O2,air2out}*\left(\frac{P}{P°}\right)}} \right) \ [V]$$

$$V_0 = 1.253 - 2.4516 * 10^{-4} * T_{SOFC} \ [V] \ [53]$$

2) Ohmic losses

$$Vohm = \left(\sum_{k} \rho_k * L_k \right) * i$$

Where ρ_k represents the resistivity of the anode, cathode and of the electrolyte and are retrieved from literature [54]. Lk is the thickness of the anode, cathode and electrolyte.

3) Activation losses

$$Vact = Vact, a + Vact, c = \frac{R * T_S}{F} * sinh^{-1}\left(\frac{i}{2 * io, a}\right) + \frac{R * T_S}{F} * sinh^{-1}\left(\frac{i}{2 * io, c}\right)$$

F is the Faraday's constant=96845 C/mol, Ts is the temperature of the solid structure, which is defined as Ts=$\left(\frac{TFC,in+TFC,out}{2}\right)$

4) Concentration losses

$$Vconc = Vconc, a + Vconc, c$$

$$= \left[-\frac{R * T_{SOFC,out}}{2F} * ln\left(1 - \frac{i}{i, as}\right) + \frac{R * T_{SOFC,out}}{2F}\right.$$

$$\left. * ln\left(1 + \frac{y_{H2,FC,out} * i}{y_{H2O,FC,out} * i, as}\right)\right] - \frac{R * T_{SOFC,out}}{4F} * ln\left(1 - \frac{i}{i, cs}\right)$$

i,as and i,cs are the limiting current density of the anode and cathode respectively, which are calculated as follows:

$$i, as = \frac{2F * P_{SOFC} * y_{H2,FC,out} * D_{aeff}}{R * T_{SOFC,out} * La}$$

$$i, cs = \frac{4F * P_{SOFC} * y_{O2,air2,out} * D_{ceff}}{(1 - y_{O2,air2,out}) * (R * T_{SOFC,out} * Lc)}$$

5) Potential of the cell

$$V_{cell} = V_n - V_{ohm} - V_{act} - V\_conc \qquad [V]$$

6) Power of the SOFC

$$W_{el,cell} = V_{cell} * i_{cell} * A_{cell} \qquad [W]$$

7) Power of SOFC stack

$$W_{el,SOFC,stack} = W_{el,net} + W_{consumed} \qquad [W]$$

8) Number of cells:

$$Nr_{cells} = \frac{W_{el,SOFC,stack}}{W_{el,cell}}$$

9) Efficiency of the fuel cell

$$\eta_{SOFC} = \frac{W_{el,SOFC}}{\frac{N_{ref,out}}{Nr_{cells}} * LHV}$$

10) Fuel utilization factor

The fuel utilization factor is defined as the ratio between the hydrogen consumed by the cell and the inlet hydrogen.

$$U_F = \frac{n_{H2,FC\ out} - n_{H2,FC\ in}}{n_{H2,FC\ in}}$$

11) Recycling ratio

$$r = \frac{N_{flue\ gas}}{N_{FC,out}}$$

4.3 Results and discussion

The selected fuel for this analysis was ethanol. The effect of recycling was tested for r=0% to 50% and C/O=0.6 to 1 fixing the SOFC current density at 0.4 A/cm^2. Then the effect of the current density and the fuel utilization of the SOFC is evaluated at a fixed C/O ratio.

4.3.1 Recycling and C/O ratio effect

Efficiency of the system

Figure 4.2 shows the effect of the recycling and C/O on the overall efficiency of the system. The dotted line represents the limit of the carbon formation zone inside the reformer: moving to the right side of it, coke deposition starts occurring inside the reformer, as previously explained in the thermodynamic analysis of the experimental activity.

The overall efficiency of the system presented in figure 4.2 is decreasing with recycling, indeed more power is consumed since both the recycled tail gas and the inlet fuel increase. The C/O ratio does not affect significantly the efficiency of the system, excepts for high recycling ratios (40% and 50%) , due to a higher increase in the molar flow rate of ethanol.
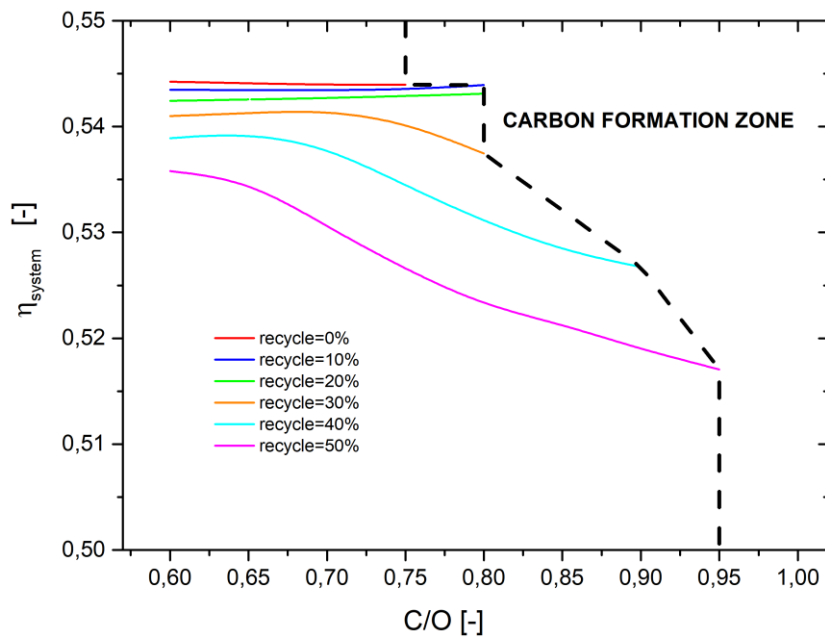
Figure 4.2 Effect of recycling and C/O on the efficiency of the SOFC-APU system

Efficiency and power of the single solid-oxide fuel cell

Figure 4.3 shows the effect of recycling at different C/O ratio for the efficiency of the SOFC. As the rate of recycling increases, the efficiency of the solid oxide fuel cell exhibits a remarkable reduction, which can be explained as a combination of two effects: at fixed C/O ratio, the molar flow rate at the inlet of the cell increases with the recycle ratio, while, as represented in figure 4.4, the electric power produced by the cell drops since the syngas produced by the reformer and flowing inside the fuel channel of the SOFC contains a lower concentration of hydrogen. The efficiency of the cell progressively decreases along the C/O coordinate: the increase of the electric power produced by the SOFC is lower than the increase in the heating value provided by the outlet stream of the reformer, which is

characterized by less oxygenated species, especially methane. Although recycling presents a detrimental impact on the efficiency of the cell and the system, it shows a beneficial effect since it allows the system to perform in wider carbon-free zones, thus in safer conditions in terms of coke formation.
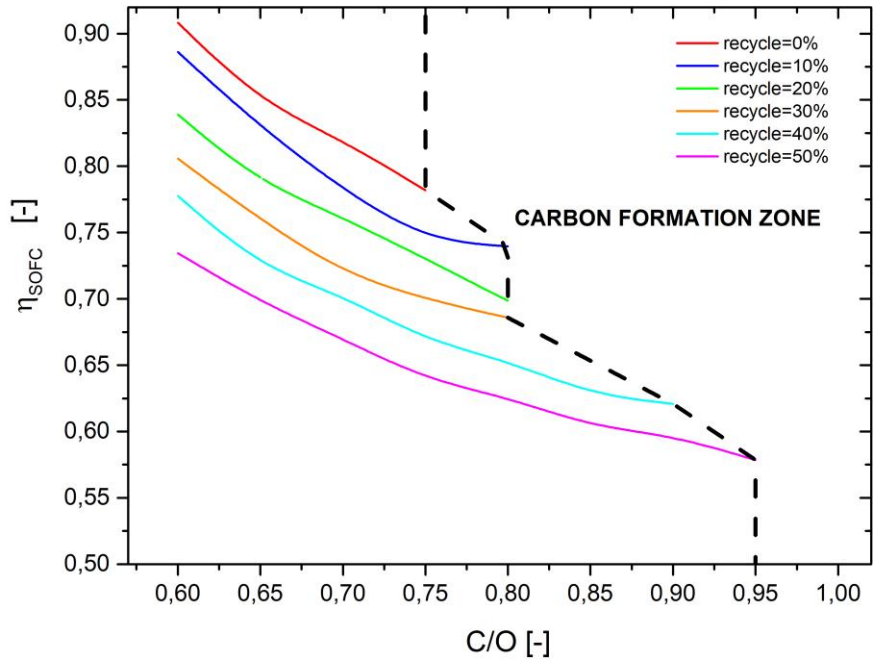
Figure 4.3 Effect of recycling and C/O on the efficiency of the single solid-oxide fuel cell
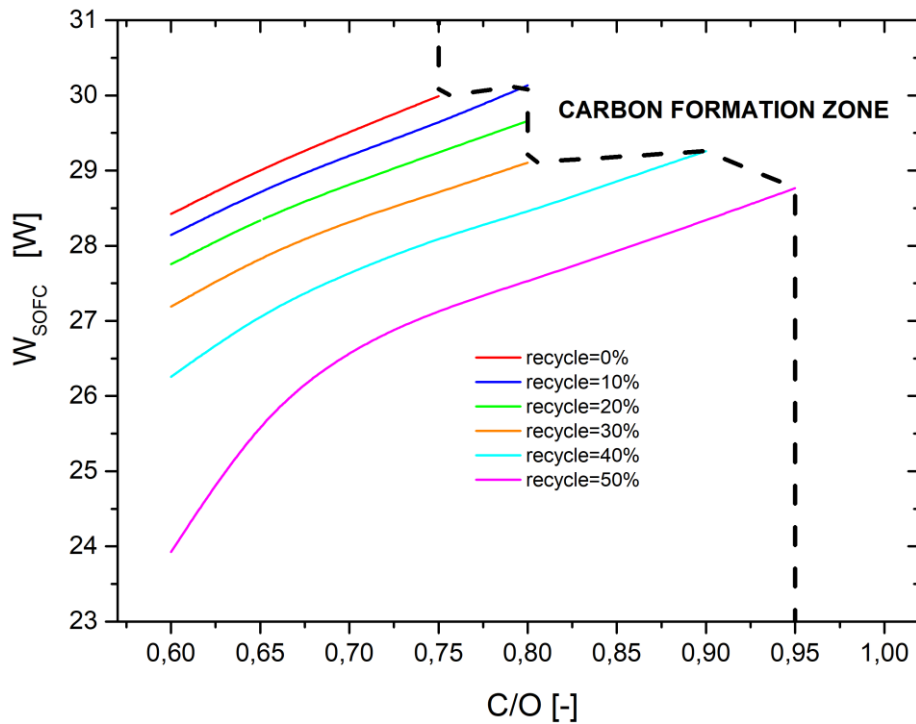
Figure 4.4 Effect of recycling and C/O on the power of the single solid-oxide fuel cell

Outlet temperature of the reformer

By examining the effect of the reformer feeding conditions, at fixed C/O ratio, recycling part of the hot flue gases of the SOFC leads to an increase in the inlet molar flow and temperature of the reformer (figure 4.5), increasing the extent of the endothermic reactions therefore reducing the adiabatic equilibrium temperature of the reformer (figure 4.6). This has a beneficial effect in terms of controlling the sintering process which is favoured at high temperatures [38]. At higher recycling rates, the heat capacity of the system increases as a result of the higher flow rates, thus the curve is characterized by a lower slope leading to a lower decrease of the temperature with the C/O ratio. Accordingly, with this trend, as the carbon formation zone is approached (C/O>0.8), the opposite effect is shown, where recycling is increasing the outlet temperature of the reformer.
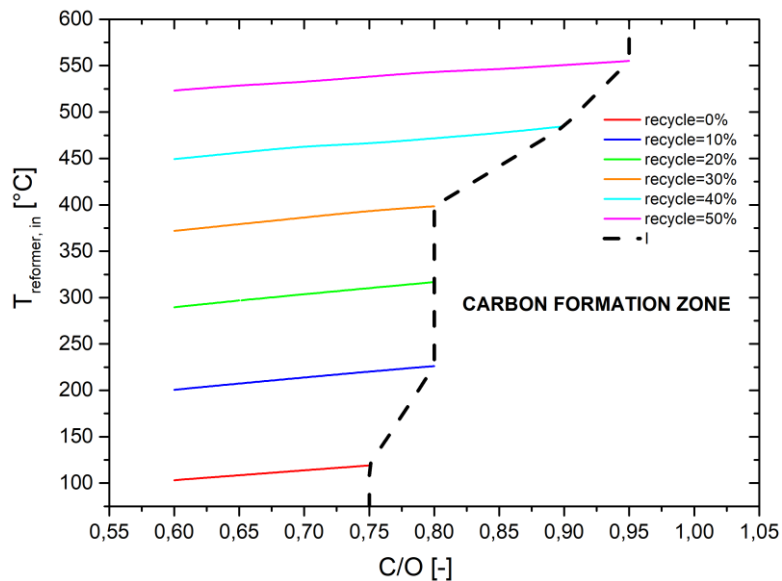
Figure 4.5 Effect of recycling and C/O on the inlet temperature of the reformer
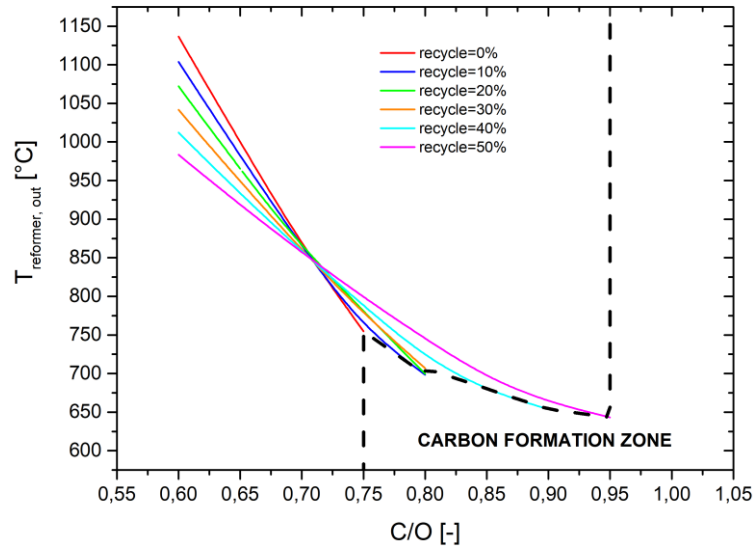
Figure 4.6 Effect of recycling and C/O on the outlet temperature of the reformer

4.3.2 Current density effect

A sensitivity analysis performed by changing the current density and fixing the C/O=0.7, Uf=0.7, $T_{SOFC,out}$=850°C , showed that there are no significant effects on the parameters of the model. The only exception is represented by the power produced by a single cell, whose trend is represented in figure 4.7. As the current density increases, the cell produces more power. As the rate of recycle increases, the power produced decreases as explained before: in case of 50% recycling the curve stops at i_{cell}=0.4 A/cm^2 since after this value the anode limiting current density is exceeded, leading to a null cell potential and power [56].
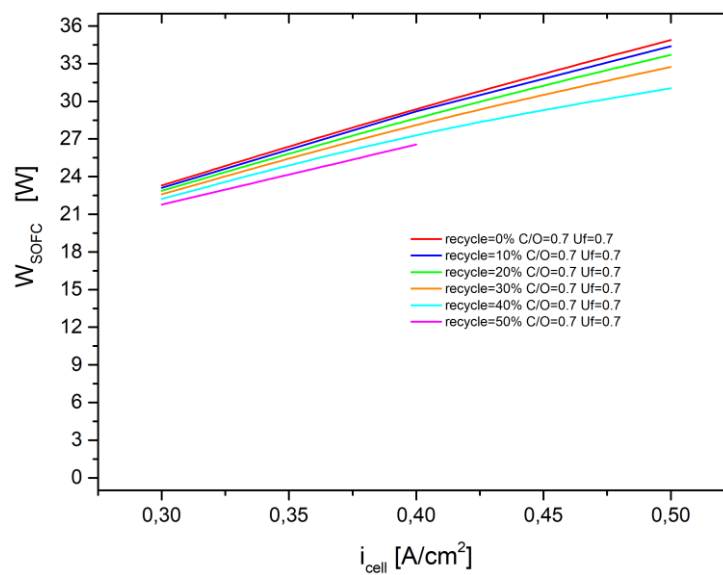
Figure 4.7 Effect of the current density of the cell on the power of the single SOFC

4.3.3 Fuel utilization effect

The fuel utilization (Uf) effect was evaluated with C/O=0.7, i_{cell}=0.4 A/cm^2, $T_{SOFC,out}$=850°C and results are plotted in figure 4.8. Increasing Uf improves the efficiency of the cell, although the power output decreases. It may be considered controversial to have low power output and high electrical efficiency at the same time: this is due to the fact that less mass flow rate going inside the cell is needed for higher fuel utilization ratios. Hence, it is seen that increasing this ratio improves the cell thermodynamically, and this is perfectly in line with the results found in literature [52].
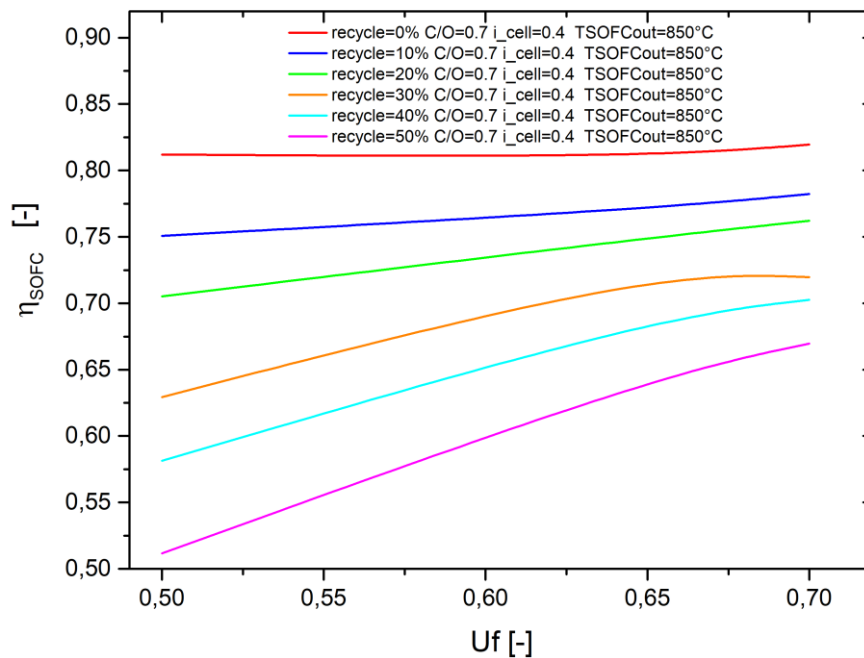
Figure 4.8 Effect Uf on the efficiency of the single solid-oxide fuel cell

Conclusions

In this thesis work, the Catalytic Partial Oxidation (CPO) of ethanol on Rh/α-Al$_2$O$_3$ catalyst has been studied in a lab-scale adiabatic reactor, to verify the potentials and critical issues of this process for the small-scale production of H$_2$. This study addresses the analysis of the effect of CO$_2$ dilution in CPO of ethanol-water mixture in terms of the catalyst stability and performance.

Following the same procedure performed to evaluate the effect of the operating conditions of the CPO of different liquid fuels [44], the effect of the CO$_2$ recycling is studied using a higher C/O ratio (0.7) with respect to the C/O ratio (0.65) adopted in a previous thesis work and reducing the dilution ratio R from 0.5 to 0.25. CO$_2$ is added by replacing part of the diluting N$_2$ so to keep a constant dilution (H$_2$O+ CO$_2$+ N$_2$) R=0.25. Consecutive temperature and concentration tests were performed with the same feeding conditions, alternated with characterization methane temperature tests performed to monitor the extent of deactivation phenomena. Replacing part of the diluting nitrogen with CO$_2$ shifted the adiabatic equilibrium temperature to a lower value moving the whole profile to lower temperatures. The concentration profiles show a lower selectivity towards hydrogen production, whereas, on the other hand, higher concentration of CH$_4$ in the oxy-reforming zone is observed, which may be related to the different temperature in this area. The addition of CO$_2$ may favour the reverse water gas shift reaction or the ethanol dry reforming reaction at the entrance of the reactor, leading to the observed consumption of CO$_2$ and the increased production of CO and H$_2$O

Post mortem TPO tests performed on this monolith catalyst showed that a limited but significant coke deposition occurred, with more severity with respect to the carbon deposit of the NE5 catalyst (tested with water-cofeed only in previous work).

The effect of the FHS configuration was tested on a new catalyst (OTT2). The experiments were performed with CH$_4$ with a molar fraction y$_{CH4}$ equals 27.8% and a C/O=0.9. The temperature profile exhibits a higher hot spot (960°C) than the BHS configuration. Noteworthy, there was a reduced selectivity towards hydrogen and carbon monoxide.

A further investigation was conducted where the catalyst was cut along its central axis and it was found that the length of the internal coated area is different from the external one. This was probably related to an uneven distribution of the coating inside the channels suggesting the need to modify the coating technique in order to solve this problem.

The results from the SOFC-APU analysis showed that, although flue gas recycling penalizes the performances of the system, it has a beneficial effect since it allows the system to work at higher C/O ratios without entering in the carbon formation zone, hence safer conditions are expected with the increase of recycling. The power of the SOFC also increases along with recycling, thus leading to more compact stack with a lower number of cells to achieve the target Pel,net. However a more detailed analysis should be performed on the selected size, as well as an introduction of neglected losses in the system, which could properly described the performace of each component via an exergy analysis.

The experimental results of this study can be used in a future work to provide validation to a reactor model of ethanol CPO extending the existing model for methane, propane, and iso-octane CPO. the presence of such models help in optimizing the reactor design and selecting the proper working condition to take further steps towards commercialization of the process.

Moreover, further investigation of flue gas recycling will be needed with different CO_2 concentrations to provide a better understanding of this process. Regarding suppression of the coke deposition, using different catalyst supports such as $MgAl_2O_4$ as substitute for the acidic α-Al_2O_3 support may enhance the catalyst stability as it will lower the tendency of carbon formation.

List of Figures

List of Tables

Bibliography

[1] M. Plazas-González, C. A. Guerrero-Fajardo, and J. R. Sodré, "Modelling and simulation of hydrotreating of palm oil components to obtain green diesel," *J. Clean. Prod.*, vol. 184, pp. 301–308, 2018, doi: 10.1016/j.jclepro.2018.02.275.

[2] L. D. Schmidt, E. J. Klein, C. A. Leclerc, J. J. Krummenacher, and K. N. West, "Syngas in millisecond reactors: Higher alkanes and fast lightoff," *Chem. Eng. Sci.*, vol. 58, no. 3–6, pp. 1037–1041, 2003, doi: 10.1016/S0009-2509(02)00645-0.

[3] J. D. Holladay, J. Hu, D. L. King, and Y. Wang, "An overview of hydrogen production technologies," *Catal. Today*, vol. 139, no. 4, pp. 244–260, 2009, doi: 10.1016/j.cattod.2008.08.039.

[4] J. Sehested, "Four challenges for nickel steam-reforming catalysts," *Catal. Today*, vol. 111, no. 1–2, pp. 103–110, Jan. 2006, doi: 10.1016/j.cattod.2005.10.002.

[5] A. P. E. York, T. Xiao, and M. L. H. Green, "Brief overview of the partial oxidation of methane to synthesis gas," *Top. Catal.*, vol. 22, no. 3–4, pp. 345–358, 2003, doi: 10.1023/A:1023552709642.

[6] H. Liander, "The utilisation of natural gases for the ammonia process," *Trans. Faraday Soc.*, vol. 25, p. 462, 1929, doi: 10.1039/tf9292500462.

[7] P.Franchetti and C.Padovani, "Incomplete oxidation of methane with oxygen and air," *Chim.Ind.Appl*, vol. 15, 1933.

[8] M.Pettre C. Eichner and M.Perrin, "The catalytic oxidation of methane with oxygen and air," *Trans. Faraday Soc.*, vol. 42, p. 335b, 1946.

[9] G.Racz G.Szekely K. Huszar, "Investigation of the partial catalytic oxidation of methane," *Acta Chim. Accad. Sci. Hungaricae*, vol. 70, pp. 287–299, 1971.

[10] D. A. Hickman, E. A. Haupfear, and L. D. Schmidt, "Synthesis gas formation by direct oxidation of methane over Rh monoliths," *Catal. Letters*, vol. 17, no. 3–4, pp. 223–237, 1993, doi: 10.1007/BF00766145.

[11] D. HICKMAN, "Synthesis gas formation by direct oxidation of methane over Pt

monoliths*1," *J. Catal.*, vol. 138, no. 1, pp. 267–282, Nov. 1992, doi: 10.1016/0021-9517(92)90022-A.

[12] S. S. Bharadwaj and L. D. Schmidt, "Catalytic partial oxidation of natural gas to syngas," *Fuel Process. Technol.*, vol. 42, no. 2–3, pp. 109–127, 1995, doi: 10.1016/0378-3820(94)00098-E.

[13] A. M. Efstathiou, A. Kladi, V. A. Tsipouriari, and X. E. Verykios, "Reforming of methane with carbon dioxide to synthesis gas over supported rhodium catalysts: II. A steady-state tracing analysis: Mechanistic aspects of the carbon and oxygen reaction pathways to form CO," *J. Catal.*, vol. 158, no. 1, pp. 64–75, 1996, doi: 10.1006/jcat.1996.0006.

[14] A. B. Mhadeshwar and D. G. Vlachos, "Hierarchical, multiscale surface reaction mechanism development: CO and H2 oxidation, water-gas shift, and preferential oxidation of CO on Rh," *J. Catal.*, vol. 234, no. 1, pp. 48–63, 2005, doi: 10.1016/j.jcat.2005.05.016.

[15] M. Bizzi, G. Saracco, R. Schwiedernoch, and O. Deutschmann, "Modeling the partial oxidation of methane in a fixed bed with detailed chemistry," *AIChE J.*, vol. 50, no. 6, pp. 1289–1299, 2004, doi: 10.1002/aic.10118.

[16] A. Donazzi, A. Beretta, G. Groppi, and P. Forzatti, "Catalytic partial oxidation of methane over a 4% Rh/α-Al2O3 catalyst Part II: Role of CO2 reforming," *J. Catal.*, vol. 255, no. 2, pp. 259–268, 2008, doi: 10.1016/j.jcat.2008.02.010.

[17] R. P. O'Connor, E. J. Klein, and L. D. Schmidt, "High yields of synthesis gas by millisecond partial oxidation of higher hydrocarbons," *Catal. Letters*, vol. 70, no. 3–4, pp. 99–107, 2000, doi: 10.1023/A:1018825015184.

[18] G. J. Panuccio, K. A. Williams, and L. D. Schmidt, "Contributions of heterogeneous and homogeneous chemistry in the catalytic partial oxidation of octane isomers and mixtures on rhodium coated foams," *Chem. Eng. Sci.*, vol. 61, no. 13, pp. 4207–4219, 2006, doi: 10.1016/j.ces.2006.02.010.

[19] G. J. Panuccio and L. D. Schmidt, "Species and temperature profiles in a differential sphere bed reactor for the catalytic partial oxidation of n-octane," *Appl. Catal. A*

Gen., vol. 332, no. 2, pp. 171–182, 2007, doi: 10.1016/j.apcata.2007.06.035.

[20] M. Hartmann, L. Maier, H. D. Minh, and O. Deutschmann, "Catalytic partial oxidation of iso-octane over rhodium catalysts: An experimental, modeling, and simulation study," *Combust. Flame*, vol. 157, no. 9, pp. 1771–1782, 2010, doi: 10.1016/j.combustflame.2010.03.005.

[21] M. G. Zabetakis, "Flammability characteristics," *Flammabl. Charact. Combust. gases Vap.*, pp. 20–27, 1965.

[22] L. V. Mattos and F. B. Noronha, "Hydrogen production for fuel cell applications by ethanol partial oxidation on Pt/CeO2 catalysts: The effect of the reaction conditions and reaction mechanism," *J. Catal.*, vol. 233, no. 2, pp. 453–463, 2005, doi: 10.1016/j.jcat.2005.04.022.

[23] N. M. Marinov, "Kinetic Model for High Temperature Ethanol Oxidation," *Int. J. Chem. Kinet.*, vol. 31, no. 3, pp. 183–220, 1999.

[24] M. Koehle and A. Mhadeshwar, "Microkinetic modeling and analysis of ethanol partial oxidation and reforming reaction pathways on platinum at short contact times," *Chem. Eng. Sci.*, vol. 78, pp. 209–225, 2012, doi: 10.1016/j.ces.2012.05.017.

[25] A. N. Fatsikostas and X. E. Verykios, "Reaction network of steam reforming of ethanol over Ni-based catalysts," *J. Catal.*, vol. 225, no. 2, pp. 439–452, 2004, doi: 10.1016/j.jcat.2004.04.034.

[26] S. Cavallaro, V. Chiodo, A. Vita, and S. Freni, "Hydrogen production by auto-thermal reforming of ethanol on Rh/Al2O3 catalyst," *J. Power Sources*, vol. 123, no. 1, pp. 10–16, 2003, doi: 10.1016/S0378-7753(03)00437-3.

[27] H. Chen *et al.*, "Hydrogen production via autothermal reforming of ethanol over noble metal catalysts supported on oxides," *J. Nat. Gas Chem.*, vol. 18, no. 2, pp. 191–198, 2009, doi: 10.1016/S1003-9953(08)60106-1.

[28] M. Tóth, E. Varga, A. Oszkó, K. Baán, J. Kiss, and A. Erdohelyi, "Partial oxidation of ethanol on supported Rh catalysts: Effect of the oxide support," *J. Mol. Catal. A Chem.*, vol. 411, pp. 377–387, 2016, doi: 10.1016/j.molcata.2015.11.010.

[29] J. R. Salge, G. A. Deluga, and L. D. Schmidt, "Catalytic partial oxidation of ethanol over noble metal catalysts," *J. Catal.*, vol. 235, no. 1, pp. 69–78, 2005, doi: 10.1016/j.jcat.2005.07.021.

[30] A. Carrera, A. Beretta, and G. Groppi, "Catalytic Partial Oxidation of Iso-octane over Rh/α-Al2O3 in an Adiabatic Reactor: An Experimental and Modeling Study," *Ind. Eng. Chem. Res.*, vol. 56, no. 17, pp. 4911–4919, 2017, doi: 10.1021/acs.iecr.7b00255.

[31] A. Donazzi *et al.*, "Synergy of homogeneous and heterogeneous chemistry probed by in situ spatially resolved measurements of temperature and composition," *Angew. Chemie - Int. Ed.*, vol. 50, no. 17, pp. 3943–3946, 2011, doi: 10.1002/anie.201007346.

[32] D. Livio, C. Diehm, A. Donazzi, A. Beretta, and O. Deutschmann, "Catalytic partial oxidation of ethanol over Rh/Al2O3: Spatially resolved temperature and concentration profiles," *Appl. Catal. A Gen.*, vol. 467, pp. 530–541, 2013, doi: 10.1016/j.apcata.2013.07.054.

[33] A. Mostafa, Y. Uysal, R. B. S. Junior, A. Beretta, and G. Groppi, "Catalytic Partial Oxidation of ethanol over Rh-coated monoliths investigated by the axially resolved sampling technique: Effect of H2O co-feed," *Catal. Today*, no. April, 2020, doi: 10.1016/j.cattod.2020.09.030.

[34] K. L. Hohn and L. D. Schmidt, "Partial oxidation of methane to syngas at high space velocities over Rh-coated spheres," *Appl. Catal. A Gen.*, vol. 211, no. 1, pp. 53–68, 2001, doi: 10.1016/S0926-860X(00)00835-8.

[35] K. Heitnes Hofstad, J. H. B. J. Hoebink, A. Holmen, and G. B. Marin, "Partial oxidation of methane to synthesis gas over rhodium catalysts," *Catal. Today*, vol. 40, no. 2–3, pp. 157–170, 1998, doi: 10.1016/S0920-5861(98)00004-2.

[36] S. Galluzzi and D. Ballabio, "Ossidazione parziale catalitica di i-C8H18 e n-C8H18 su catalizzatori Rh/α-Al2O3, Msc Thesis," 2016.

[37] J. G. Li, T. Ikegami, J. H. Lee, T. Mori, and Y. Yajima, "A wet-chemical process yielding reactive magnesium aluminate spinel (MgAl2O4) powder," *Ceram. Int.*,

vol. 27, no. 4, pp. 481–489, 2001, doi: 10.1016/S0272-8842(00)00107-3.

[38]   M. Argyle and C. Bartholomew, "Heterogeneous Catalyst Deactivation and Regeneration: A Review," *Catalysts*, vol. 5, no. 1, pp. 145–269, Feb. 2015, doi: 10.3390/catal5010145.

[39]   A. Lindermeir, S. Kah, S. Kavurucu, and M. Mühlner, "On-board diesel fuel processing for an SOFC-APU-Technical challenges for catalysis and reactor design," *Appl. Catal. B Environ.*, vol. 70, no. 1–4, pp. 488–497, 2007, doi: 10.1016/j.apcatb.2006.02.025.

[40]   J. Rechberger, A. Kaupert, J. Hagerskans, and L. Blum, "Demonstration of the First European SOFC APU on a Heavy Duty Truck," *Transp. Res. Procedia*, vol. 14, no. x, pp. 3676–3685, 2016, doi: 10.1016/j.trpro.2016.05.442.

[41]   D. Livio, A. Donazzi, A. Beretta, G. Groppi, and P. Forzatti, "Optimal design of a CPO-reformer of light hydrocarbons with honeycomb catalyst: Effect of frontal heat dispersions on the temperature profiles," *Top. Catal.*, vol. 54, no. 13–15, pp. 866–872, 2011, doi: 10.1007/s11244-011-9710-1.

[42]   R. Horn, N. J. Degenstein, K. A. Williams, and L. D. Schmidt, "Spatial and temporal profiles in millisecond partial oxidation processes," *Catal. Letters*, vol. 110, no. 3–4, pp. 169–178, 2006, doi: 10.1007/s10562-006-0117-8.

[43]   D. Livio, "Ossidazione parziale catalitica di propano," 2012.

[44]   A. Donazzi, D. Livio, A. Beretta, G. Groppi, and P. Forzatti, "Surface temperature profiles in CH4 CPO over honeycomb supported Rh catalyst probed with in situ optical pyrometer," *Appl. Catal. A Gen.*, vol. 402, no. 1–2, pp. 41–49, 2011, doi: 10.1016/j.apcata.2011.05.022.

[45]   C. Cristiani *et al.*, "Activation of metallic open-cell foams via washcoat deposition of Ni/MgAl 2O 4 catalysts for steam reforming reaction," *Catal. Today*, vol. 197, no. 1, pp. 256–264, 2012, doi: 10.1016/j.cattod.2012.09.003.

[46]   R. Batista, A. Carrera, A. Beretta, and G. Groppi, "Thermal deactivation of Rh/α-Al2O3 in the catalytic partial oxidation of iso-octane: Effect of flow rate," *Catalysts*, vol. 9, no. 6, 2019, doi: 10.3390/catal9060532.

[47] B. Mcbride, S. Gordon, and M. Reno, "Coefficients for Calculating Thermodynamic and Transport Properties of Individual Species," *Nasa Tech. Memo.*, vol. 4513, no. NASA-TM-4513, p. 98, 1993, [Online]. Available: http://ntrs.nasa.gov/archive/nasa/casi.ntrs.nasa.gov/19940013151_1994013151.pdf.

[48] A. Rimoldi and M. Stigliani, "Catalytic Partial Oxidation of methane, iso-octane and ethanol on Rh coated monoliths: in situ measurements of temperature and concentration profiles," 2018.

[49] A. SIMPSON and A. LUTZ, "Exergy analysis of hydrogen production via steam methane reforming," *Int. J. Hydrogen Energy*, vol. 32, no. 18, pp. 4811–4820, Dec. 2007, doi: 10.1016/j.ijhydene.2007.08.025.

[50] S. Perry, R. H. Perry, D. W. Green, and J. O. Maloney, *Perry's chemical engineers' handbook*, vol. 38, no. 02. 2000.

[51] D. C. Larson, C. B. Weinberger, A. Lawley, D. H. Thomas, and T. W. Moore, *Fundamentals Of Engineering Energy*, vol. 83, no. 4. 1994.

[52] C. O. Colpan, I. Dincer, and F. Hamdullahpur, "Thermodynamic modeling of direct internal reforming solid oxide fuel cells operating with syngas," *Int. J. Hydrogen Energy*, 2007, doi: 10.1016/j.ijhydene.2006.10.059.

[53] P. Jienkulsawad, D. Saebea, Y. Patcharavorachot, and A. Arpornwichanop, "Design of the integrated solid oxide fuel cell and molten carbonate fuel cell system to reduce carbon dioxide emissions," *Chem. Eng. Trans.*, vol. 43, pp. 2191–2196, 2015, doi: 10.3303/CET1543366.

[54] U. G. Bossel, "Final report on SOFC Data, Facts & Figures," no. April, p. 70, 1992.

[55] F. Barbir, "Fuel Cell Electrochemistry," in *PEM Fuel Cells*, Elsevier, 2005, pp. 33–72.

[56] J. Hanna, W. Y. Lee, Y. Shi, and A. F. Ghoniem, "Fundamentals of electro- and thermochemistry in the anode of solid-oxide fuel cells with hydrocarbon and syngas fuels," *Prog. Energy Combust. Sci.*, vol. 40, no. 1, pp. 74–111, 2014, doi: 10.1016/j.pecs.2013.10.001.